

TIME-RESOLVED INFRARED SPECTROSCOPY AT THE NSLS U12IR
BEAMLINE

BY

JOSEPH DONALD LAVEIGNE

A DISSERTATION PRESENTED TO THE GRADUATE SCHOOL
OF THE UNIVERSITY OF FLORIDA IN PARTIAL FULFILLMENT
OF THE REQUIREMENTS FOR THE DEGREE OF
DOCTOR OF PHILOSOPHY

UNIVERSITY OF FLORIDA

1999

ACKNOWLEDGMENTS

I would like to offer sincere thanks my adviser, Professor David B. Tanner, for his encouragement and advice during my graduate career. His support and guidance have been invaluable to me and I will continue to look to him as an example of an ideal mentor and colleague.

I would also like to thank Professor David Reitze, a member of my committee, for his advice and assistance with the time-resolved project. I also thank Professors S. Hershfield, J. Graybeal and R. Singh for serving on my committee and reading this dissertation.

I would like to thank my collaborators at Brookhaven National Lab, L. Carr and R. Lobo, for their assistance and conversations. I would like to thank all my past and present colleagues in Tanner's group and those who worked in his lab for their conversations, friendship and cooperation: H.L. Liu, A. Zibold, A. Ugawa, L. Gasparov, C. Porter, D. John, N.L. Tache, V. Boychev, S. Hong, J. Hwang, S. Moore, and R. Kumar.

I would like to express my gratitude for technical support to the members of the machine shop, electronics shop and cryogenics team of the University of Florida physics department, as well as the members of the experimental shop at the NSLS. I would also like to acknowledge the invaluable assistance of the physics department staff, especially C. Bright, in handling the bureaucratic details at UF while I was in Brookhaven.

I would like to thank my parents, Don and Midge LaVeigne, for their support, both emotional and financial during my entire educational career. Finally, I give

special thanks to my wife, Yao-yi Tseng. For her constant love, support and patience, I am very grateful.

TABLE OF CONTENTS

ACKNOWLEDGMENTS	ii
ABSTRACT	vii
CHAPTERS	
1 INTRODUCTION	1
1.1 History	1
1.2 Motivation	1
1.3 Organization	2
2 EXPERIMENTAL METHODS	5
2.1 Introduction	5
2.2 Spectroscopy	5
2.2.1 Monochromators	6
2.2.2 Interferometers	8
2.3 Theory of FTS	9
2.3.1 Disadvantages of Film Beam Splitters	15
2.3.2 Wavefront Separation	17
2.3.3 Aliasing	18
2.3.4 Phase Correction and Apodization	20
2.3.5 Fast Scan Interferometry	22
2.3.6 Time-Resolved Measurements Using Interferometers	23
2.4 Synchrotron Radiation	25
2.4.1 Introduction	25
2.4.2 Synchrotron Radiation Theory	25
2.4.3 Infrared Synchrotron Radiation	30
2.4.4 Comparison of Synchrotron and Thermal Sources	32
2.4.5 Pulsed Nature of the Source	37
2.4.6 Coherent Emission	38
2.5 Optical Properties of Materials	39
2.5.1 Dielectric Response Function $\epsilon(\omega)$	39
2.5.2 Determination of Film Thickness From Interference Fringes	42
2.5.3 Modeling Absorption	43
2.5.4 Sum Rule	44

3	EXPERIMENT	45
3.1	Introduction	45
3.2	NSLS VUV Ring	46
3.3	General Beamline Description	49
3.4	Pump Laser System	52
3.4.1	Mode-locked Ti:sapphire Laser	57
3.4.2	Photoinduced Measurements	60
3.5	Lamellar Grating Interferometer	62
3.5.1	Description	62
3.5.2	Laser Insertion	67
3.5.3	Measurement Methods	68
3.5.4	Source Comparison	70
3.6	Bruker 113V Fast Scan Interferometer	72
3.6.1	Description	72
3.6.2	Laser Insertion	74
3.6.3	Measurement Methods	75
3.6.4	Source Comparison	78
4	TIME-RESOLVED IR STUDIES OF $\text{Hg}_x\text{Cd}_{1-x}\text{Te}$	81
4.1	Introduction	81
4.2	Optical Properties of MCT	82
4.2.1	Transmission	82
4.2.2	Time-resolved Measurements	83
4.2.3	Estimated Carrier Density	85
4.2.4	Time-resolved Spectroscopy	89
4.2.5	Sum Rule	95
4.3	Summary	97
5	TIME-RESOLVED IR STUDIES OF Pb FILMS	98
5.1	Introduction	98
5.2	Superconductivity	99
5.2.1	FIR Transmission of Thin Superconducting Films	100
5.2.2	Non-equilibrium Superconductors	100
5.3	Experiment	104
5.3.1	Film Growth and Characterization	104
5.3.2	ZPD Decay	106
5.3.3	Temperature Dependence of the Quasiparticle Lifetime	112
5.3.4	Time-resolved Spectroscopy	119
5.3.5	$\text{Pb}_{0.75}\text{Bi}_{0.25}$	122
5.4	Summary	124

6	CONCLUSION	126
APPENDICES		
A	COHERENT EMISSION	130
A.1	Introduction	130
A.2	Observations	131
A.3	Summary	135
B	USING A BOLOMETER AS A MID IR DETECTOR	137
B.1	Introduction	137
B.2	Experiment	138
B.3	Summary	144
C	LASER OPERATION	146
C.1	Description	146
C.2	Manual	148
C.3	Optimization of the Downstream Optics	150
	REFERENCES	152
	BIOGRAPHICAL SKETCH	157

Abstract of Dissertation Presented to the Graduate School
of the University of Florida in Partial Fulfillment of the
Requirements for the Degree of Doctor of Philosophy

TIME-RESOLVED INFRARED SPECTROSCOPY AT THE NSLS U12IR
BEAMLINE

By

Joseph Donald LaVeigne

August 1999

Chairman: David B. Tanner
Major Department: Physics

Synchrotron radiation has been used as a light source for many decades. First used as a source for ultraviolet and x-rays, in the 1970s and 1980s pioneering work was done in the use of synchrotron radiation as an infrared source. A synchrotron source has several advantages over a thermal source. Although it has lower total power than a thermal source over most of the IR spectrum, the synchrotron has higher brightness. At very low frequencies, the synchrotron produces more power than a standard black body source. The least used advantage of synchrotron radiation is the pulsed nature of the source. The electrons in the ring are contained in bunches causing the synchrotron radiation to be emitted in pulses which have a high repetition rate. This advantage is put to use to perform time-resolved or pump-probe infrared spectroscopy.

The U12IR beamline of the National Synchrotron Light Source (NSLS) at Brookhaven National Lab (BNL) is a newly constructed beamline dedicated to time-resolved and far infrared spectroscopy. It is operated by a collaboration between the NSLS, the physics department of BNL and the Department of Physics at the University of Florida.

This dissertation presents a detailed description of the beamline including two endstations (spectrometers) and the pump laser system. The synchrotron pulses have a duration of 0.3–1.5 ns (FWHM), with a maximum time between pulses of ~ 180 ns, allowing phenomena with time scales from hundreds of ps to hundreds of ns to be investigated. Data from two series experiments are presented, including a study of electron-hole pair relaxation in $\text{Hg}_x\text{Cd}_{1-x}\text{Te}$ films and pair recombination in superconducting lead and lead bismuth films.

The MCT films show a high relaxation rate, consistent with a large number of defects at the surface of the film. Far infrared studies show free carrier absorption at low frequencies. Mid IR studies show a decrease in absorption near the absorption edge of the band gap, consistent with states being removed by the promotion of carriers from the valence band to the conduction band. A deviation from the sum rule for oscillator strengths is found and explained by insufficient data in the mid IR region.

The superconducting Pb and PbBi films show an increase in absorption in their FIR spectra due to pair breaking by the incident pump pulse. The recombination time of the quasiparticles is resolved at the lowest temperatures. The temperature dependence of the lifetime is inferred from signal changes with the pump and probe pulses coincident.

The dissertation concludes with a summary of the performance of the beamline and a discussion of some proposed enhancements to the current experiment.

CHAPTER 1 INTRODUCTION

1.1 History

The equations describing synchrotron radiation were first published in 1949 by Schwinger [1]. Since that time, synchrotrons have been used as sources for a number of optical experiments. The first applications made use of the x-ray or ultraviolet (UV) portions of the spectrum for which other sources were not available. In the 1970s and early 1980s, pioneering work was done in the use of synchrotron radiation as a source of infrared (IR) light [2]. Since that time, several beamlines dedicated to IR radiation have been constructed at sites around the world [3, 4, 5, 6]. Although throughout most of the IR spectrum the power emitted by most rings is less than a typical glowbar source, it's high brightness makes it very useful for surface science and microscopy [7, 8].

1.2 Motivation

The high brightness of a synchrotron source is not its only benefit. They can produce more power than a typical thermal source at very long wavelengths. Synchrotrons also produce light in a series of pulses at a high repetition rate. It is the pulsed nature of synchrotron radiation that will be put to use in the work of this dissertation to perform time-resolved spectroscopy. Synchrotron sources

have been used to perform time-resolved experiments in the past [9, 10]. The U12IR beamline at the National Synchrotron Light Source (NSLS) is a facility currently undergoing commissioning and is dedicated to far infrared and time-resolved infrared spectroscopy. The beamline provides a unique opportunity for measuring transient phenomena on time scales in the 100s of ps to 100s of ns range over a broad region of the electromagnetic spectrum. The broadband nature of the source allows the use of well developed interferometry techniques and is the major advantage of using synchrotrons over terahertz spectroscopy [11].

The facility provides a tool for studying many non-equilibrium systems in solid state physics. Systems studied in this dissertation include electron-hole plasma relaxation in semiconductors and quasiparticle recombination in normal superconductors. Many other systems are also of interest such as photogenerated carriers in conducting polymers as well as quasiparticle recombination and photoinduced doping in high- T_c superconductors.

1.3 Organization

This dissertation describes experiments using two end stations on the U12IR beamline of the NSLS Vacuum Ultraviolet (VUV) ring. These experiments involve time-resolved spectroscopy and cover the frequency range of 2-10,000 cm^{-1} . Much of the work centered around the construction of various devices for coupling the synchrotron radiation into the sample, or bringing the laser pump pulses to the sample with adequate power and at the correct time relative to the synchrotron probe pulses.

First, a theoretical discussion of various types of spectrometers is presented. The advantages and disadvantages of Fourier transform interferometric spectrometers and monochromators are discussed. Two types of interferometers are described, those using a semitransparent beam splitter for amplitude separation and those using a lamellar grating for wavefront separation. A general discussion of synchrotron radiation follows with a focus on IR. Calculations of the brightness advantage of SR over thermal sources and of the power advantage at low frequencies will be discussed. The use of the pulsed source for time-resolved measurements and the implications that has on the frequency resolution of the experiment is investigated.

Following that is a description of the experimental apparatus. The specifics of the beamline including the extraction optics, and methods of bringing the IR radiation to the spectrometers will be presented. The time-resolved experiments use a pump-probe technique with a mode-locked Ti:sapphire laser synchronized to the ring radio frequency (RF) as an excitation source. Details of the laser, the optics used to bring the laser pulses to the sample, and the electronics for keeping the laser pulses in phase with the probe pulses are also presented. Techniques for various time-resolved experiments are discussed including those used for both step scan and fast scan instruments.

Chapter 4 describes a study of a thin $\text{Hg}_x\text{Cd}_{1-x}\text{Te}$ film on a CdTe substrate. Time-resolved transmission measurements were made in both the far and mid IR regions. The FIR data show carriers are generated and follow their decay back to a bound state. The mid IR data show bleaching near the semiconductor gap. This bleaching is attributed to a reduction in the density of available electronic states

in the valence band as some electrons are promoted to the conduction band by the pump pulse. The data are consistent with a single carrier being responsible for the observed changes and based on the predicted mobility, the carriers are taken to electrons. The measured lifetime is much shorter than that observed in clean $\text{Hg}_x\text{Cd}_{1-x}\text{Te}$. The differences are attributed to increased scattering from surface defects. The results are discussed with a focus on the sum rule for oscillator strengths. The increased absorption in the FIR region is compensated by a decrease in the mid infrared. Some deviation from the sum rule is observed and attributed to a lack of precision in the mid IR measurements.

Chapter 5 presents time-resolved studies of superconducting Pb and $\text{Pb}_{0.75}\text{Bi}_{0.25}$ films. Time-resolved transmission measurements in the FIR region follow the recombination of quasiparticles generated from Cooper pairs broken by the pump pulse. Frequency averaged transmission measurements allow the direct measurement of the quasiparticle lifetime and its temperature dependence. The measured lifetime and temperature dependence are found to be in agreement with previously published observations and theory. Time-resolved spectra showing the excitation and relaxation of the system are presented and used to estimate the number of excess quasiparticles generated.

Overall, this dissertation describes the U12IR beamline and presents results from the first time-resolved experiments conducted thereon. It shows the range of capabilities of this new facility in both frequency coverage and time resolution. The synchrotron source is shown to be useful in characterizing device structures and in studying fundamental phenomena of solid state physics.

CHAPTER 2 EXPERIMENTAL METHODS

2.1 Introduction

In this chapter experimental methods in this research are discussed. The first part of the chapter is devoted to Fourier transform spectroscopy. The theory of Fourier transform spectroscopy will be developed. Using the developed theory, some limitations and differences in various types of spectrometers will be discussed. In the second part, synchrotron radiation will be discussed. The equations defining synchrotron radiation will be developed. Some approximations valid for the infrared spectrum will be presented and discussed. A comparison between synchrotron and standard thermal sources will be made, including power, brightness and time structure differences. The third part contains a review of the optical properties of materials, including a discussion on the dielectric response function, various models of that response function and a discussion on the sum rule for oscillator strengths.

2.2 Spectroscopy

A spectrometer is a device used to determine the intensity of some source of light as a function of frequency $I(\omega)$. For consistency, in this writing, frequency is defined as $\omega = 2\pi c/\lambda$, where c is the speed of light and λ is the wavelength of the

light. Generally there are 2 types of spectrometers in common use, monochromators and interferometers. Monochromators use a grating, prism or other device to separate spatially the light from the source into its component frequencies. Then, the particular frequency range of interest is selected by a slit or other aperture. The light from this aperture is then passed to the sample and into a detector where the intensity is measured. Interferometers use either a partially reflecting, partially transmitting beam splitter or a wavefront divider to separate the light from the source into two parts. The path difference between the two beams is varied and then the light is recombined. The recombined beams interfere with each other depending on the difference in length between the two paths, leading to a measured intensity that varies with the path difference. The measured intensity as a function of path difference is called the interferogram. This interferogram is then Fourier transformed yielding a power spectrum (see Section 2.3.) See Figure 2.1 for diagram of a typical spectroscopic experiment.

2.2.1 Monochromators

One of the most common instruments for visible and near infrared (NIR) spectroscopy is a monochromator. This type of instrument makes use of a prism or grating to separate spatially the light from the source into its component frequencies. The light is passed through a slit, which selects a particular narrow range of frequencies. The light then passes through the optics of the experiment and is brought to the detector. The grating or prism is stepped so that another frequency is selected by the slit and the power spectrum is directly measured at the detector. Grating monochromator instruments use diffraction to separate the light. For

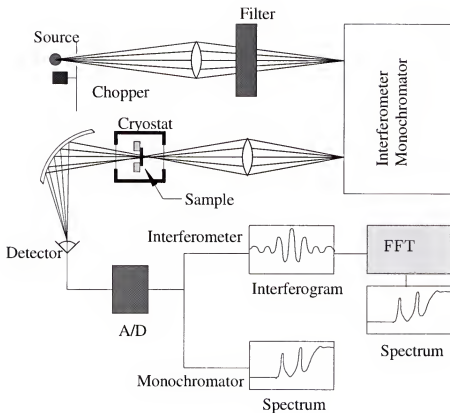


Figure 2.1: A diagram of a typical experimental setup.

wavelength λ [12],

$$\lambda = \frac{d}{m (\sin \theta_m - \sin \theta_i)} \quad (2.1)$$

where m is the order of the diffraction, d is the grating spacing, θ_m is the angle between the grating face and θ_i is the angle of the incident light on the grating. In order to prevent components of other frequencies due to higher order diffraction ($m = 2, 3, \dots$) a filter is used to select only the frequency range of interest.

The maximum attainable resolution is determined by the size of the grating (number of lines) and the focal optics. The instrumental resolution of the experi-

ment is determined by the width of the entrance and exit slits. The advantages of a monochromator are in its simplicity. The power spectrum is directly measured at the detector. There is no need for further manipulation of the data as with FT spectroscopy. The largest disadvantage of a monochromator is the monochromatic sampling. Depending on the signal to noise of the experiment, because a monochromator only measures one frequency at a time, the time it takes to generate a spectrum can be quite long.

2.2.2 Interferometers

The other common type of spectrometer is the interferometer. Interferometers separate the source beam into two parts, the two beams traverse different paths and are then recombined where they interfere. The difference in path length between the two beams is varied and the resulting signal, called an interferogram, is measured. The interferogram is then Fourier transformed to yield the power spectrum (see Section 2.3.) Interferometers have a multiplex advantage over monochromators, called the Fellgett advantage [13]. The fact that all frequencies impinge on the detector at all times allows for higher signal to noise and thus quicker sampling when compared to monochromator instruments. The advantage is only true for detector noise limited systems, making it very useful for far and mid infrared spectroscopy. For higher frequencies, increasing photon “shot” noise reduces the Fellgett advantage. The other “disadvantage” of interferometers is the necessity of the Fourier transform itself which may introduce errors into the spectrum if proper care is not taken.

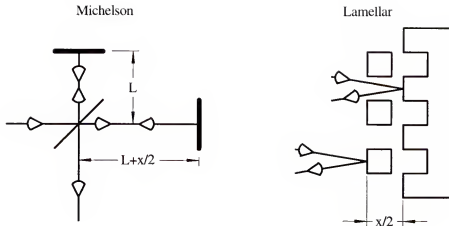


Figure 2.2: Simplified representations of the two common types of interferometers. The Michelson uses a partially transmitting, partially reflecting beam splitter for amplitude separation, the lamellar uses a grating for wavefront separation.

Generally, there are 2 types of interferometers differentiated by how they separate the source light. One type of instrument uses a partially reflecting, partially transmitting beam splitter to amplitude separate the source. The most common interferometer using amplitude separation is the Michelson interferometer. The second type of interferometer uses separate reflecting surfaces to wavefront separate the light. Two mirrors, or more often a lamellar grating can be used for this purpose.

2.3 Theory of FTS

Consider the basic experiment shown in Figure 2.3¹. For this discussion we will use a simplified Michelson interferometer, but the theory is general and will hold

¹This derivation is based on a series of lectures given by D.B Tanner in 1994. For other derivations consult the literature [14, 15, 16, 17, 18].

for any type. The source emits an electric field spectrum $S_0(\omega)$:

$$S_0(\omega) = E_0(\omega)e^{i(\vec{k} \cdot \vec{r} - \omega t)}. \quad (2.2)$$

The light traverses a distance S to the beam splitter with a reflectivity r_b and a transmissivity t_b . The reflected beam goes a distance L to a fixed mirror with reflectivity² r_y and phase ϕ_y , and the transmitted beam goes a variable distance $L + x/2$ to a moving mirror with reflectivity r_x and phase ϕ_x . The two beams return to the beam splitter and are again transmitted or reflected with efficiency t_b and r_b and portions of the beams then travel a distance D to the detector. At the detector the electric field is a superposition of the fields of the two beams (taken at time $t = 0$):

$$E_D = E_0 e^{ikS} \left(r_b e^{ikL} r_y e^{i\phi_y} e^{ikL} t_b + t_b e^{ik(L+x/2)} r_x e^{i\phi_x} e^{i(kL+x/2)} r_b \right) e^{ikD} \quad (2.3)$$

In some cases, the one of the mirrors may be replaced with a sample, in which case both magnitude and phase information about the reflected beam can be obtained. For our discussion, we will assume the end mirrors are near perfect reflectors such that $r_x \simeq r_y \simeq -1$. We define the frequency ω by the relation $k = \frac{2\pi\nu}{c} = \frac{2\pi}{\lambda} \equiv \omega$ (i.e., $c = 1$). Measure x in cm and ν in cm^{-1} , $\omega = 2\pi\nu$. Let $\phi(\omega) = \phi_x - \phi_y$ and $\Phi = k(S + D + L) + \phi_y$. Making those substitutions, E_D becomes:

$$E_D = E_0 r_b t_b e^{i\Phi} \left[1 + e^{i(\omega x + \phi(\omega))} \right]. \quad (2.4)$$

²All quantities refer to amplitudes.

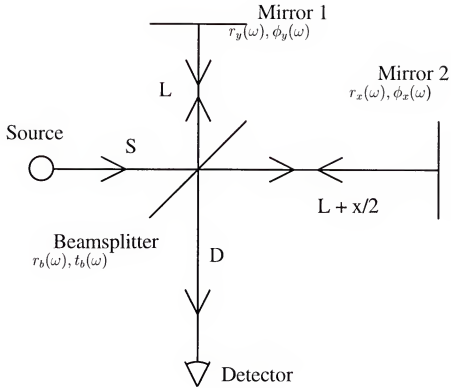


Figure 2.3: A schematic diagram of the Michelson interferometer used for our development of the theory of FTS.

Thus the spectrum at the detector is:

$$\begin{aligned}
 S_D = E_D E_D^* &= S_0(\omega) \mathcal{F}_b \mathcal{R}_b \left[1 + e^{i(\omega x + \phi(\omega))} \right] \left[1 + e^{-i(\omega x + \phi(\omega))} \right] \\
 &= S_0(\omega) \mathcal{F}_b \mathcal{R}_b \left[1 + \cos(\omega x + \phi(x)) \right].
 \end{aligned}
 \tag{2.5}$$

Now, define a beam splitter efficiency ϵ_b . For an ideal beam splitter there is no absorption, thus, $\mathcal{A}_b = 0$ and $\mathcal{T}_b = 1 - \mathcal{R}_b$. In that case

$$\mathcal{T}_b \mathcal{R}_b = \mathcal{R}_b(1 - \mathcal{R}_b) = \begin{cases} 0 & \text{if } \mathcal{R}_b = 0 \\ 0 & \text{if } \mathcal{R}_b = 1 \\ \frac{1}{4} & \text{if } \mathcal{R}_b = \frac{1}{2} \text{ (max).} \end{cases} \quad (2.6)$$

So, we define ϵ_b as

$$\epsilon_b = 4 \mathcal{T}_b \mathcal{R}_b = 4 \mathcal{R}_b(1 - \mathcal{R}_b). \quad (2.7)$$

Equation 2.5 gives the intensity of frequency ω at the detector. However, the measured quantity is the overall intensity at the detector I_D as a function of the path difference x , so now write:

$$I_D(x) = \frac{1}{2} \int_0^\infty S(\omega) \epsilon_b(\omega) [1 + \cos(\omega x + \phi(\omega))] d\omega. \quad (2.8)$$

For the special cases of $x \rightarrow \infty$ and $x = 0$ we have the following: For the case $x \rightarrow \infty$ the cosine averages to zero so we have:

$$I_D(\infty) \equiv I_\infty = \frac{1}{2} \int_0^\infty S(\omega) \epsilon_b(\omega) d\omega. \quad (2.9)$$

For the case $x = 0$ and $\phi = 0$ (zero path difference or ZPD):

$$I_D(0) \equiv I_0 = \int_0^\infty S(\omega) \epsilon_b(\omega) d\omega. \quad (2.10)$$

Now, define S_D to be the spectrum arriving at the detector so $S_D(\omega) = S_0(\omega)\epsilon_b(\omega)$. At the detector, the measured quantity is the difference between the intensity at each point and the average value we have the measured interferogram $\gamma = I_D(x) - I_\infty$, or

$$\gamma = \frac{1}{2} \int_0^\infty S_D(\omega) \cos(\omega x + \phi(\omega)) d\omega \quad (2.11)$$

So, γ is the cosine Fourier transform of S_D . Now write $\cos(\omega x + \phi)$ as $\frac{1}{2}e^{i\omega x}e^{i\phi} + \frac{1}{2}e^{-i\omega x}e^{-i\phi}$. Assuming S_D is hermitian as it should be for a real response, γ can be written as:

$$\gamma(x) = \frac{1}{4} \int_{-\infty}^\infty S_D(\omega) e^{i\phi(\omega)} e^{i\omega x} d\omega \quad (2.12)$$

Taking the inverse Fourier transform of this yields:

$$S_D(\omega) e^{i\phi(\omega)} = \frac{2}{\pi} \int_{-\infty}^\infty \gamma(x) e^{-i\omega x} dx. \quad (2.13)$$

The desired result is to get the spectrum at the detector S_D . The additional phase term may cause significant errors and must be handled carefully.

In the case of experimental FTS, all of the interferograms are taken at equally spaced discrete points. In the ideal case, one of those points would fall on at ZPD, however, in a real experiment, there is always an error ξ between the measured point and ZPD. The discrete nature of the real experiment can be handled mathematically by multiplying the continuous interferogram by a infinite sum of Dirac δ functions:

$$\gamma_S = \gamma(x) \sum_{j=-\infty}^{\infty} \delta(x - j\delta - \xi) \quad (2.14)$$

where δ is the spacing between the points. This makes the inverse Fourier transform into

$$S_D(\omega)e^{i\phi(\omega)} = \frac{2}{\pi} \sum_{j=-\infty}^{\infty} \gamma(j\delta + \xi)e^{-i\omega j\delta} e^{-i\omega\xi}. \quad (2.15)$$

This discretizing of the interferogram causes two effects of note. First, it introduces an additional term $e^{-i\omega j\delta}$ into the spectrum. This term can be viewed as another kind of phase error, to be handled in part of the phase correction. The second effect is to make the spectrum periodic. This effect leads to the possibility of aliasing or “folding” and will be discussed in more depth later.

For real experiments there is also a limit on the size of the interferogram. Points are taken within some finite distance on either side of ZPD. We write this as $-L_1 \leq x \leq L_2$ and for convenience we take $L_2 \geq L_1$. This truncation can be described mathematically by a function $A(x)$, called the apodization. For the case described above, also known as the “boxcar”, $A(x)$ is:

$$A(x) = \begin{cases} 0 & \text{for } x < -L_1 \\ 1 & \text{for } -L_1 \leq x \leq L_2 \\ 0 & \text{for } x > L_2 \end{cases} \quad (2.16)$$

Thus, the function which is transformed is not the complete interferogram, but instead the product of the interferogram and the apodization. The result of this is that the spectrum is the convolution of the “real” spectrum with the apodization. In the case of the boxcar apodization, the Fourier transform of $A(x)$ is a $\text{sinc}(x)$ function [$\text{sinc}(x) = \sin(x)/x$]. The characteristic width of the function is $1/L_2$. If a single sine wave of frequency ν_1 were convolved with a boxcar apodization with

maximum length L_2 , the resultant spectrum would be a $\text{sinc}(x)$ function centered at ν_1 with width $1/L_2$. Thus, the resolution is limited to $\Delta\nu \approx 1/L_2$. The convolution also introduces side lobes near sharp features in the spectrum. These side lobes may be reduced by multiplying the interferogram by using a different apodization function but this will come at the cost of a further reduction in resolution. Further details on the effects of various apodizations can be found in the literature.

2.3.1 Disadvantages of Film Beam Splitters

Although we started with a Michelson interferometer in the example, up until now, all the equations derived have been generally true for all interferometers. Now, we consider the effect of using a film beam splitter. The reflectivity of a plane wave of frequency ω incident at angle φ on a film of thickness d with index of refraction n is described by the following equation [12]:

$$R = \frac{E_r}{E_0} = e^{i\omega t} \left[\frac{r(1 - e^{-i\delta})}{1 - r^2 e^{-i\delta}} \right] \quad (2.17)$$

Where $\delta = 2knd \cos \varphi$ and r is the single bounce reflectivity. Note that if δ is an even multiple of π the reflectivity and hence the reflectance \mathcal{R}_b would be zero. This has a profound effect on the efficiency, ϵ_b , causing it to oscillate between zero and some maximum, but always starting at zero for zero frequency [*i.e.*, $\epsilon_b(\omega \rightarrow 0) \rightarrow 0$]. All film beam splitters produce this interference pattern due to multiple internal reflections in the film. This structure causes limitations in the resolution and frequency range attainable using that beam splitter. For mylar films, a common type of film used in the FIR region, the thickness of the beam

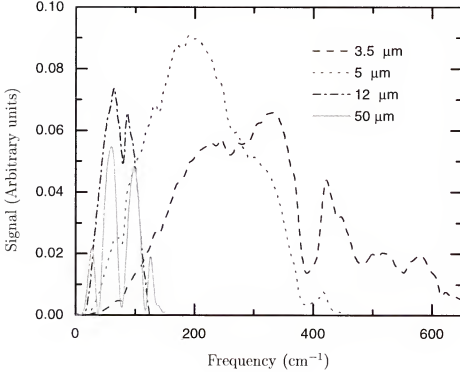


Figure 2.4: Plot of single beam spectra taken with a series of mylar beam splitters. For all but the $50\text{ }\mu\text{m}$ films, the spectra are electronically filtered above the first minimum due to the beam splitter.

splitter produces an interference fringe with a spacing on the order of the frequency range of interest, generally a few 10's to a few 100's of wavenumbers, dependent on the film thickness. Thus, in order to measure a full frequency range one must use a set of beam splitters with varying thickness. See Figure 2.4 for an example of a set of spectra taken with a “normal” set of mylar beam splitters. As the desired frequency range gets lower, the beam splitters get progressively thicker and have a more and more narrow usable region, that still goes to zero at zero frequency. Another option is to use a thicker film or wafer as the beam splitter. An undoped

Si wafer is a common choice for this type of beam splitter. Although very appealing because of the large range of frequencies covered, the wafer thickness introduces a fringe with spacing on the order of a few wavenumbers, limiting the maximum resolution attainable.

2.3.2 Wavefront Separation

The other type of interferometer uses wavefront separation. This type of interferometer uses a grating or other multi-planed surface to spatially separate the incoming beam [19, 15]. One section of the grating is recessed compared to the other introducing the necessary path difference. The wavefront separation class has the advantage of a constant efficiency at low frequencies. Grating or other wavefront separation instruments do not suffer the loss of efficiency at low frequencies due to multiple reflections inherent in film beam splitters. The “beam splitter” efficiency of a grating or other wavefront instrument is governed by the material properties (reflectivity). At low frequencies the grating acts as a waveguide causing the light polarized parallel to the grating facets to have a different phase velocity than that of light polarized perpendicular to the facets [14]. For unpolarized light, this causes the the two possible polarizations to interfere destructively leading to a loss of modulation and thus limiting the lowest frequencies available. The response of the grating is good until the wavelength is comparable to the grating spacing. At the upper frequencies, the efficiency is limited by the diffraction of the grating. For the modes higher than the zeroth order, the light is modulated but is out of phase by π with that of the zeroth order. For high frequencies, these orders enter the exit aperture and interfere destructively with the zeroth order, leading to loss

of signal. The frequency where the loss begins is given by [19]:

$$\nu_s = \frac{f}{sd} \text{ cm}^{-1}, \quad (2.18)$$

where f is the focal length of the focusing mirror, d is the grating constant and s is the dimension of the limiting aperture, all measured in cm. For example, the grating used in the experiments described in this dissertation had a 1 cm spacing and provided usable modulation of frequencies from $\sim 1 \text{ cm}^{-1}$ up to 100 cm^{-1} .

2.3.3 Aliasing

We now return to the subject of aliasing or “folding”. Aliasing is caused by discretizing the interferogram. The interference causes an ambiguity in the frequencies measured. For this discussion we will refer to Equation 2.15, and make the further simplifying assumption of zero phase error. Thus, to start we have,

$$S_D(\omega) = \frac{2\delta}{\pi} \sum_{-\infty}^{\infty} \gamma(k\delta) e^{-i\omega k\delta}. \quad (2.19)$$

Note that if we replace ω with $\omega + \frac{2\pi}{\delta}$ we have

$$S_D\left(\omega + \frac{2\pi}{\delta}\right) = S_D(\omega),$$

or the spectrum is now periodic with period $\frac{2\pi}{\delta}$. Now recall that in Section 2.3, we assumed the spectrum at the detector was hermitian. Thus, $S_D(\omega) = S_D(-\omega)$.

This combined with the periodicity shown above implies

$$S_D(\omega + \frac{(2n+1)\pi}{\delta}) = S_D(-\omega).$$

in other words the spectrum is mirrored about the frequencies $\frac{(2n+1)\pi}{\delta}$. The frequency $\frac{\pi}{\delta}$ is known as a “folding frequency” and is also known as the Nyquist frequency. This folding and periodicity allow aliasing of higher frequency components into the lower frequency part of the spectrum. Another way to see this is to consider the following example. Suppose there is a interferometer measuring with a step of 0.01 cm corresponding to a maximum measured frequency $\nu_{max} = 2\pi/0.01 \text{ cm} = 628 \text{ cm}^{-1}$. Now suppose that the source for that interferometer is monochromatic with a variable frequency. First we illuminate it with light of frequency $0.5\nu_{max} = 314 \text{ cm}^{-1}$. Next, let us illuminate with light of frequency $1.5\nu_{max} = 942 \text{ cm}^{-1}$. Figure 2.5 shows these two frequencies and their corresponding samples. Note that even though the frequencies are different, the sampled points are the same because the sampling is not fine enough to measure the higher frequency. This is aliasing, the spectral components of higher frequencies gets folded back onto the calculated spectrum. This folding back of the spectral content of higher frequencies can cause the resultant spectrum to contain errors. In order to avoid aliasing, the spectral content of the higher frequencies must be removed before the interferogram is Fourier transformed. This can be accomplished by optical filtering, or in the case of fast scan interferometers, electrical filtering.

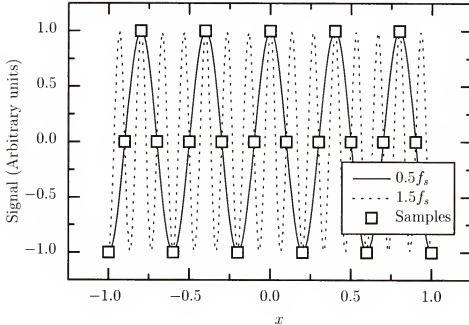


Figure 2.5: Graphic depiction of aliasing.

2.3.4 Phase Correction and Apodization

The next two subjects we will cover in the discussion of FTS are phase correction and apodization. There is a fair amount of literature available on these subject [20, 17, 18, 14, 15] and a thorough treatment is beyond the scope of this discussion. Therefore, only a general description will be given here and it is left to the reader to use the references if a further investigation is desired.

We begin with apodization. As mentioned in Section 2.3, the effects of truncating the interferogram are to limit the frequency resolution and introduce side lobes near sharp features. So far, the case we have described has the interferogram being truncated immediately at $-L_1$ and L_2 . This can be described as the

apodized interferogram

$$\gamma_A(x) = A(x)\gamma(x)$$

where

$$A(x) = \begin{cases} 0 & \text{for } x < -L_1 \\ A(x) & \text{for } -L_1 \leq x \leq L_2 \\ 0 & \text{for } x > L_2 \end{cases} \quad (2.20)$$

The function $A(x)$ is known as the apodization function. For the case studied so far we have used $A(x) = 1$ also known as the boxcar apodization. This apodization yields the maximum resolution, however it also produces the worst side lobes. The side lobes can be reduced by choosing an apodization that goes to zero less abruptly. As mentioned before, the reduction of the side lobes is accompanied by a reduction in resolution. Some other apodizations often used are the triangular, trapezoidal, Happ-Genzel and Blackman-Harris. These produce varying degrees of side lobe reduction. For a further discussion of apodization see the literature on the subject [20, 21, 14, 17].

Now we move on to the subject of phase correction. As shown previously in Equation 2.13, the result of the Fourier transformed interferogram contains a term $e^{i\phi(\omega)}$. This term is a result of various properties of the experiment that lead to phase error, such as differences in the mirrors, phase changes introduced by the sample, electronic filtering and sampling error. Since the desired result is the spectrum $S_D(\omega)$, something must be done to remove the phase term and this process is known as phase correction. The most direct method was introduced by Mertz. This method is as follows. Suppose we start with our previous example of a interferogram sampled from $-L_1$ to L_2 and $L_1 \leq L_2$. Then, for the Mertz method,

we take a small portion of this interferogram on equal sides of ZPD, $-L_1 \leq x \leq L_1$ and perform a Fourier transform. We use this transform to calculate the phase. Since we used a smaller maximum path difference, the result is a low resolution phase term. We assume the phase is slowly varying and interpolate the phase for the points of the full interferogram. We then take the full interferogram, perform a Fourier transform and multiply the result $e^{-i\phi_i(\omega)}$, where $\phi_i(\omega)$ is the interpolated phase.

A second method is to always take interferograms with equal distances on either side of ZPD. Then one can calculate the power spectrum from the real and imaginary parts of the transform. Another method involves the convolution of the interferogram with the Fourier transform of $e^{i\phi(\omega)}$. This will produce a symmetric interferogram. A cosine Fourier transform of this symmetrized interferogram will then yield the power spectrum. These methods are well defined in the literature and the reader is encouraged to visit the references cited for further details [20, 21, 14].

2.3.5 Fast Scan Interferometry

Interferometers may take data in one of two ways. They may either step along with a constant step length, stopping at each step to take a data point. Or they may use a moving mirror and some means of triggering sampling as the mirror passes each interval of δx . The moving mirror has the effect of mixing an optical frequency f_o down to a lower (audio) frequency f_a . Consider a monochromatic source of frequency f_o . This has a wavelength $\lambda = \frac{c}{f_o}$, where c is the speed of light. For an interferometer with a mirror traveling at velocity v , the time it takes to pass through one cycle of the interference pattern is $\frac{\lambda}{v}$. Thus the resulting audio

frequency is:

$$f_a = \frac{v}{\lambda} = \nu_o v \text{ Hz.}$$

With the optical frequency, ν_o in cm^{-1} , the velocity in cm/s and the audio frequency, f_a in Hz . Having a continuous signal at audio frequencies allows the use of conventional electronic filters to reduce noise and prevent aliasing.

2.3.6 Time-Resolved Measurements Using Interferometers

In the previous sections of this chapter we have discussed using interferometers for optical measurements. Until now, our discussion has always assumed the source to be in a steady state. However, if time resolved measurements are called for, a time-varying source must be used. Dependent on the relationship between the desired optical resolution and time resolution, a time dependent source may have significant effects on the relationships we have derived previously.

There are 2 general cases to be considered:

$$\begin{aligned} \Delta x &\ll c\Delta t \\ \Delta x &\geq c\Delta t \end{aligned} \tag{2.21}$$

where Δx is the maximum path difference between the two arms of the interferometer, Δt is the duration of the source pulse and c is the speed of light.

In the first case, the pulse intensity is approximately constant over the length of the displacements and can thus be treated like the steady state case. The second case is more complicated. As the pulse duration becomes smaller than the maximum path difference, the limiting resolution of the spectrometer appears to

be dominated by the width of the optical pulse, not the path difference. However, this is not the case. Consider the uncertainty principle which states that energy and time are conjugate variables, or:

$$\Delta E \Delta t \geq \hbar$$

If we write ΔE as $2\pi\hbar c\Delta\nu$ and Δt as $\Delta x/c$, then the relation becomes $2\pi\Delta\nu\Delta x \geq 1$, and in the case of equivalence, we have just recovered the Nyquist Theorem. Now consider a spectrum with a feature at frequency ν_0 of width $\Delta\nu$. If this sample is irradiated with a pulse of light, the frequencies near ν_0 must be dispersed such that those frequencies of the pulse are broadened to $1/\Delta\nu$ in order to satisfy the uncertainty principle. Thus, regardless of the sharpness of a feature or shortness of the source pulses, there is no limit to the frequency resolution. However, the uncertainty principle also implies that any sharp feature will not have a time constant shorter than $1/\Delta\nu$. Therefore, the experiment is limited by the time constant of the feature. In other words, in the case of a feature more narrow than the probing pulse, the experimental time resolution near the feature will be limited at the response time of the feature.

A few final notes on this subject. None of the experiments described in this dissertation have sufficiently narrow features to be affected by this limitation. The current operational parameters have the NSLS VUV ring producing minimum pulse widths of ~ 300 ps or ~ 9 cm, corresponding to a frequency resolution of ~ 0.1 cm^{-1} . The Bruker 113V has a maximum resolution of 0.03 cm^{-1} , and is therefore capable of measuring the effect. However, although there are certainly

systems with excitations more narrow than this, so far, none have been measured at this beamline. The people in the RF group continue to work on methods of further shortening the pulses and it is believed that pulses down to 100 ps may be eventually achieved. This would correspond to a resolution of $\sim .3 \text{ cm}^{-1}$ and increase the probability of having a sample-limited time resolution.

2.4 Synchrotron Radiation

2.4.1 Introduction

Electron storage rings have been in widespread use as light sources for some time now³. Initially used as visible, UV and x-ray sources, since 1987 a number of beamlines dedicated to infrared spectroscopy have been constructed. Infrared synchrotron radiation (IRSR) sources differ from thermal sources in several respects. The synchrotron produces a train of IR pulses with a higher brightness but lower overall power than thermal sources over most of the infrared spectrum. Like a thermal source, the synchrotron produces a continuous spectrum over the entire IR region. It is a stable source that is suitable for standard FTIR techniques.

2.4.2 Synchrotron Radiation Theory

Initially seen as a nuisance for accelerators, synchrotron radiation has since become vital source for research. The equations describing synchrotron radiation were first published by Schwinger in 1949 [1]. Schwinger's derivation begins with a classical nonrelativistic formula and is generalized to the relativistic case by a

³For a general discussion of synchrotron radiation and its applications see reference [22].

series of transformations. The derivation is a bit tedious, so instead we will base our development on a section of Jackson's *Classical Electrodynamics* [23]. From Jackson we have the power radiated per unit solid angle of a particle undergoing acceleration as:

$$\frac{dP(t)}{d\Omega} = |\mathbf{A}(t)|^2$$

Where $\mathbf{A}(t) = \left(\frac{c}{4\pi}\right)^{1/2} [R\mathbf{E}]_{ret}$, the *ret* subscript denotes the quantity should be evaluated at the retarded time, $t' = t - R/c$ and R is the distance from the observer to the particle at the retarded time (the time the particle emitted the radiation.) The total energy radiated per unit solid angle is:

$$\frac{dW}{d\Omega} = \int_{-\infty}^{\infty} |\mathbf{A}(t)|^2 dt$$

A Fourier transform leads to:

$$\frac{dW}{d\Omega} = \int_{-\infty}^{\infty} |\mathbf{A}(\omega)|^2 d\omega$$

The intensity I is defined:

$$\frac{dW}{d\Omega} = \int_0^{\infty} \frac{d^2 I(\omega, \mathbf{n})}{d\omega d\Omega} d\omega.$$

For real $\mathbf{A}(t)$:

$$\frac{d^2 I}{d\omega d\Omega} = 2 |\mathbf{A}(\omega)|^2$$

and

$$\mathbf{A}(\omega) = \left(\frac{e^2}{8\pi^2 c}\right)^{1/2} \int_{-\infty}^{\infty} e^{i\omega t} \left[\frac{\mathbf{n} \times \{(\mathbf{n} - \beta) \times \dot{\beta}\}}{(1 - \beta \cdot \mathbf{n})^3} \right]_{ret} dt,$$

where \mathbf{n} is the unit vector pointing from the particle at the retarded time to the observer and β is defined as $\beta = v/c$ with v the speed of the particle and c the speed of light. Switching to the retarded time yields:

$$\frac{d^2 I}{d\omega d\Omega} = \frac{e^2}{4\pi^2 c} \left| \int_{-\infty}^{\infty} \frac{\mathbf{n} \times \{(\mathbf{n} - \beta) \times \dot{\beta}\}}{(1 - \beta \cdot \mathbf{n})^2} e^{i\omega(t - \mathbf{n} \cdot \mathbf{r}(t)/c)} dt \right|^2.$$

The vector portion of the integrand is a perfect derivative,

$$\frac{\mathbf{n} \times \{(\mathbf{n} - \beta) \times \dot{\beta}\}}{(1 - \beta \cdot \mathbf{n})^2} = \frac{d}{dt} \left[\frac{\mathbf{n} \times (\mathbf{n} \times \beta)}{1 - \beta \cdot \mathbf{n}} \right].$$

Integration by parts leads to the following equation for the intensity:

$$\frac{d^2 I}{d\omega d\Omega} = \frac{e^2}{4\pi^2 c} \left| \int_{-\infty}^{\infty} \frac{\mathbf{n} \times (\mathbf{n} \times \beta)}{1 - \beta \cdot \mathbf{n}} e^{i\omega(t - \mathbf{n} \cdot \mathbf{r}(t)/c)} dt \right|^2. \quad (2.22)$$

Now, assume circular motion of radius ρ and consider the observer at a small vertical angle ψ from a tangent of the path (see Figure 2.4.2) and the time scale of interest is near $t = 0$. Then the vector part of the integrand in Equation 2.22 can be written as:

$$\mathbf{n} \times (\mathbf{n} \times \beta) = \beta \left[-\epsilon_{\parallel} \sin\left(\frac{vt}{\rho}\right) + \epsilon_{\perp} \sin\left(\frac{vt}{\rho}\right) \sin\psi \right],$$

where ϵ_{\parallel} is the unit vector pointing from the position of the particle to the center of the radius of curvature and $\epsilon_{\perp} = \mathbf{n} \times \epsilon_{\parallel}$ is the unit vector pointing in the direction perpendicular to the plane of the orbit. The argument of the exponential can be

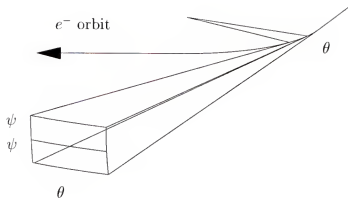


Figure 2.6: A diagram of the emitted radiation from a particle in a circular section of an orbit. The light emitted is in a narrow cone tangent to the orbit. ψ is the angle out of the plane, θ is the amount of the arc visible to the observer.

written as:

$$\omega \left(t - \frac{\mathbf{n} \cdot \mathbf{r}(t)}{c} \right) = \omega \left[t - \frac{\rho}{c} \sin \left(\frac{vt}{\rho} \right) \cos \psi \right].$$

Application of expansions valid for small arguments of t and ψ leads to the radiated energy becoming:

$$\frac{d^2 I}{d\omega d\Omega} = \left| -\epsilon_{\parallel} A_{\parallel}(\omega) + \epsilon_{\perp} A_{\perp}(\omega) \right|^2.$$

Where ϵ_{\parallel} and ϵ_{\perp} are unit vectors parallel and perpendicular to the orbital plane and the amplitudes are:

$$A_{\parallel}(\omega) \simeq \frac{c}{\rho} \int_{-\infty}^{\infty} t e^{\left\{ i \frac{\omega}{2} \left[\left(\frac{1}{\gamma^2} + \psi^2 \right) t + \frac{c^2 t^3}{3\rho^2} \right] \right\}} dt \quad (2.23)$$

$$A_{\perp}(\omega) \simeq \psi \int_{-\infty}^{\infty} e^{\left\{ i \frac{\omega}{2} \left[\left(\frac{1}{\gamma^2} + \psi^2 \right) t + \frac{c^2 t^3}{3\rho^2} \right] \right\}} dt. \quad (2.24)$$

Introduce the parameter ξ :

$$\xi = \frac{\omega\rho}{3c} \left(\frac{1}{\gamma^2} + \psi^2 \right)^{3/2}$$

and integrate to get:

$$\frac{d^2 I}{d\omega d\Omega} = \frac{e^2}{3\pi^2 c} \left(\frac{\omega\rho}{c} \right)^2 \left(\frac{1}{\gamma^2} + \psi^2 \right)^2 \left[K_{2/3}^2(\xi) + \frac{\psi^2}{(1/\gamma^2) + \psi^2} K_{1/3}^2(\xi) \right].$$

The K 's are modified Bessel functions, the first term is for light polarized in the orbital plane, the second is light polarized perpendicular to that plane. The light emitted is somewhat polarized in the plane of the synchrotron ring, with about 75% of the light emitted polarized parallel to the path of the charged particles and 25% polarized perpendicular to the path, see Figure 2.7. To put the equations in terms of emitted power instead of intensity from a single particle, replace one factor of the the charge e by the current i . The sum of the two polarizations can then be integrated over the orbital path to give an equation for the emitted power in terms of frequency and angular distribution:

$$\frac{d^2 P}{d\psi d\omega} = \frac{ei\theta}{3\pi^2 c} \left(\frac{\omega\rho}{c} \right)^2 \left(\frac{1}{\gamma^2} + \psi^2 \right)^2 \left[K_{2/3}^2(\xi) + \frac{\psi^2}{(1/\gamma^2) + \psi^2} K_{1/3}^2(\xi) \right] \quad (2.25)$$

Figure 2.4.2 shows the angular distribution of the emitted SR for several frequencies, using the parameters of the NSLS in normal operations. It shows that most of the light is emitted near the plane of the ring. As the frequency decreases, there is an increase in the distribution out of the plane.

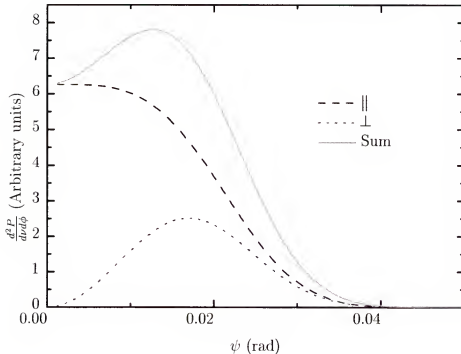


Figure 2.7: Plot of the emitted power distribution as a function of ψ for the \parallel and \perp polarizations and their sum. The plot is for a frequency of 1000 cm^{-1} and uses the parameters of the NSLS VUV ring and the extraction optics for the U12IR beamline.

2.4.3 Infrared Synchrotron Radiation

Duncan and Williams made further approximations to these equations that help clarify the properties and advantages of using IRSR as a light source [2]. For the rest of this section, we now switch to measuring frequencies in wavenumbers. Using expansions valid for small arguments of the Bessel functions they showed that

$$\frac{dP(\nu)}{d\nu} = 8.6416 \times 10^{-10} i \theta \rho^{1/3} \nu^{1/3} G \left(\frac{\text{W cm}}{\text{A}} \right), \quad (2.26)$$

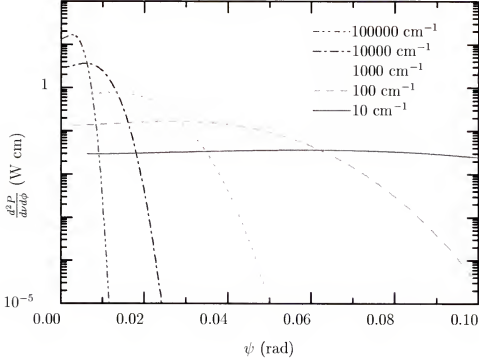


Figure 2.8: Plot of the emitted power distribution as a function of ψ for several frequencies. Note that the natural opening angle increases at lower frequencies. The plots are of the sum of both polarizations.

and

$$\left. \frac{d^2 P(\nu)}{d\nu d\psi} \right|_{\psi=0} = 5.2 \times 10^{-10} i \theta \rho^{2/3} \nu^{2/3} H \left(\frac{\text{W cm}}{\text{\AA rad}} \right). \quad (2.27)$$

The functions G and H are defined as:

$$G = \left[1 - 2.193 \left(\frac{1}{\gamma^2} \right) (\rho\nu)^{2/3} \right], \quad (2.28)$$

$$H = \left[1 - 6.312 \left(\frac{1}{\gamma^4} \right) (\rho\nu)^{4/3} \right], \quad (2.29)$$

Note that for the vertical angle distribution the approximation is only valid for $\psi = 0$. However, they give an equation for a vertical angle function $\Psi(\nu)$ such that

Parameter	Value
Temperature	2000 K
Size	0.4 cm ²
Solid Angle	0.02 sr (f/3.5)

Table 2.1: Parameters of the glowbar used as a blackbody source in the comparison of blackbody to synchrotron radiation.

it describes the angle necessary to collect the FWHM of the power distribution at that frequency.

$$\Psi(\nu) = 1.66188 \left(\frac{1}{\rho\nu} \right)^{1/3} G \text{ rad} \quad (2.30)$$

Equation 2.30 is valid for frequencies much less than the critical frequency of the ring ($\nu \ll \nu_c$), where ν_c is defined as [2]:

$$\nu_c = \frac{3\gamma^3}{4\pi\rho} \text{cm}^{-1}, \quad (2.31)$$

with ρ measured in cm. For the NSLS VUV ring, $\nu_c = 6,500,000 \text{ cm}^{-1}$, thus the approximation is good for the IR frequencies used at U12IR. A plot of Ψ using the parameters of the NSLS VUV ring is shown in Figure 2.9.

2.4.4 Comparison of Synchrotron and Thermal Sources

Let us now make a comparison between synchrotron and conventional thermal sources. For the blackbody source in this comparison we will use a glowbar with properties give in Table 2.1. First let us consider the absolute power. Figure 2.4.4 is a plot the power radiated as a function of frequency for a conventional thermal source and a synchrotron source, using the NSLS VUV parameters. Note that in the very far IR ($\omega \leq 50 \text{ cm}^{-1}$) the synchrotron has a higher output power than a

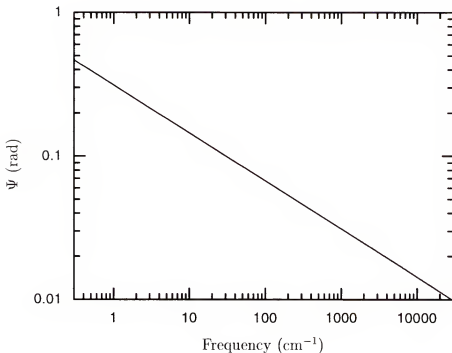


Figure 2.9: Plot of the natural opening angle Ψ as a function of frequency, using NSLS VUV parameters. The U12IR beamline has a maximum vertical opening of 90 mrad.

thermal source. For the rest of the middle and near infrared, the thermal source wins.

However, measurement times are governed by signal to noise, not absolute power. Because of the small source size, the intrinsic brightness of the synchrotron is much larger than that of a thermal source. This higher brightness is one of the great advantages of synchrotron radiation. For systems with small etendue, the high brightness can have a marked effect. It allows the study of smaller samples and surface science without requiring long sampling times. The ability to focus the light into a small spot has other advantages. For detectors whose noise limit or responsivity is governed by background radiation (such as bolometers and pho-

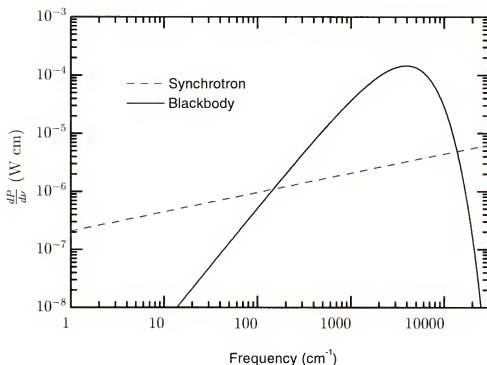


Figure 2.10: Plot of the emitted power distribution as a function frequency for a synchrotron source and a 2000 K blackbody source. The blackbody source has a significantly higher power output over most of the IR range. The synchrotron has a higher power only at the lowest frequencies.

to detectors) one can take advantage of the small spot size to make a spatial filter. An example of this can be found in Appendix B, where a test using a spatial filter for a bolometer was performed, allowing the detector, which usually has an upper limit of $700\text{--}800\text{ cm}^{-1}$, to function up to $6,000\text{ cm}^{-1}$. See the above mentioned section for more details.

For a discussion of the brightness of synchrotron there are two cases to consider. The first is the intrinsic brightness. This is the brightness calculated considering only the geometric parameters of the source. Thus it accounts for the beam size and the extended nature of the source, but does not consider diffraction effects.

For the intrinsic brightness we have,

$$B = \frac{P(\nu)}{A(\theta)}, \quad (2.32)$$

where $A(\theta)$ is the area of the source considering both the projection of the beam arc in the plane of the ring as well as the effect of not having the entire section of the arc in focus. For the actual brightness, the denominator has an additional term to account for diffraction. Thus the actual brightness becomes:

$$B_A = \frac{P(\nu)}{A(\theta) + \frac{\Omega}{\nu^2}} \quad (2.33)$$

As a comparison, for a blackbody source, the energy density is given by [24]:

$$u(\nu, T) = 16\pi^2 \hbar \frac{\nu^3}{e^{(2\pi\hbar\nu/k_B T)} - 1}. \quad (2.34)$$

The emitted power per frequency $d\nu$ is:

$$\frac{dP}{d\nu}_{BB}(\nu, T) = 16A\pi^2 \hbar c^2 \frac{\nu^4}{e^{(2\pi\hbar\nu/k_B T)} - 1}. \quad (2.35)$$

For a typical blackbody source the source area is quite large ($\sim 0.25 \text{ cm}^2$). Because of this, over most of the infrared range diffraction effects are relatively small and can be ignored. Thus, the brightness is described by the following equation:

$$B_{BB}(\nu) = \frac{16\pi^2 \hbar}{c} \frac{\nu^4}{e^{(2\pi\hbar\nu/k_B T)} - 1}. \quad (2.36)$$

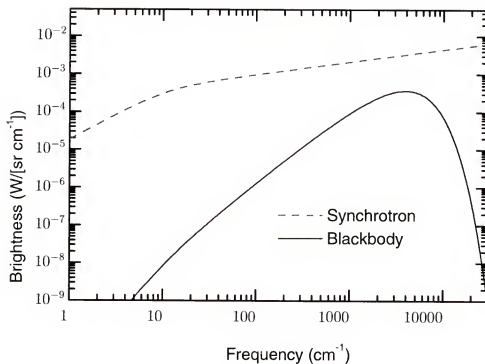


Figure 2.11: Comparison of the brightness of a synchrotron source to a blackbody source. Even though the blackbody emits more power as seen in Figure 2.4.4, the small emittance angle of the synchrotron leads to a significantly higher brightness. This can be very useful for samples with a small etendue, such as small single crystals or surface science experiments. Diffraction effects have been considered for both sources in this plot.

The assumption of limited diffraction effects leads to the use of the real area for the brightness calculation, thus the blackbody brightness is not dependent on the area of the source, just the temperature. Figure 2.11 shows a comparison between the theoretical brightness of a 2000 K blackbody and the NSLS. A more detailed comparison for specific sources and instruments can be found in Chapter 3 including measured differences in brightness.

2.4.5 Pulsed Nature of the Source

The second advantage of synchrotron sources and the one taken advantage of in this work is the pulsed nature of the source. The pulsed nature of the source allows time-resolved measurements. The fact that the source is pulsed allows fast measurements even though a slow detector is being used. For example, a common detector for the far IR is a Bolometer. A bolometer is a thermal detector that typically has a time constant on the order of msec. With a conventional steady state thermal source, that would limit the time resolution to the order of msec. With a synchrotron source, the synchrotron light is essentially taking a picture of the sample with a time scale on the order of the pulse duration (electron bunch length). Using some other source capable of short pulses to generate photoexcitations at high repetition rates and using the synchrotron as a probe source it is possible to perform pump-probe spectroscopy. For example, the experiments described in this dissertation use a mode-locked Ti:sapphire laser that is synchronized to the ring RF in this manner. Even though the bolometer is much slower, the synchrotron pulse acts like an optical gate, limiting the time seen by the sample. Thus we are able to make fast measurements even though we have much slower detector. The laser and synchrotron pulses are separated for by some delay that is held constant while a spectrum is taken. Then the delay is changed and another spectrum measured. In this way, the time-dependent response of the sample can be measured. The temporal limits of the experiment are determined by the parameters of the ring and the pump pulse. For the case a pump that is much faster than the probe pulse, the limits are determined solely by the ring.

The electrons in the ring are contained in bunches or RF "buckets". The maximum number of buckets is determined by the orbital period of the ring and the radio frequency of the amplifier driving the ring, usually called RF. The maximum number is :

$$N_{max} = \frac{D}{cT_{rf}},$$

where c is the speed of light, D the orbital path length and T_{rf} is the RF period. Not all the bunches need be filled at once. For time resolved measurements, the most interesting fills have equal spacing between the bunches. For the NSLS VUV ring, $N_{max} = 9$. Thus, the available fills for time resolved measurements are 9 bunch, 3 bunch symmetric and 1 bunch. The maximum time resolution is determined by the bunch length. The maximum decay time is determined by the time between probe pulses. For one bunch mode, this corresponds to ~ 180 ns. For more specific details on fill patterns and their effect on measurements, see Section 3.2.

2.4.6 Coherent Emission

The final point of discussion on the topic of synchrotron radiation is coherent emission. Coherent emission is expected to occur when the wavelength of the emitted light approaches the size of the electron bunches. From Williams *et al.* [25], the form of the function which determines coherence is just the Fourier transform of the single particle distribution function, $n_e(z)$. Thus for a bunch with a Gaussian distribution of particles, the enhancement due to coherent emission is of the form:

$$\frac{P_{coh}}{P_{inc}} \propto e^{2\pi^2 \tau_{BL}^2 \nu^2}, \quad (2.37)$$

where P_{coh} is the power due to coherent emission, P_{inc} is the power due to incoherent emission and τ_{BL} is the bunch length (Gaussian half-width) measured in cm. For the NSLS VUV ring operating in single bunch mode, coherent emission should only be evident at frequencies on the order of 0.01 cm^{-1} or below. These frequencies are well below those attainable with the lamellar grating spectrometer and based on this, coherent emission was not expected to be observable on the U12IR beamline. However, coherent emission is observed at the NSLS. It is very apparent in single-bunch mode with currents over 100 mA. Coherent emission is also seen in 3-bunch mode at currents over 300 mA. It is believed that the emission is caused by periodic modulation of the electron bunch, $n_e(z)$. Appendix A contains a description of the coherent emission observed at the NSLS and some possible explanations.

2.5 Optical Properties of Materials

2.5.1 Dielectric Response Function $\epsilon(\omega)$

The dielectric function $\epsilon(\mathbf{q}, \omega)$ describes the response of a material to incident radiation of frequency ω and momentum \mathbf{q} . The dielectric response is affected by various material properties including electronic band structure, crystal structure and lattice dynamics. For the IR and visible regions, the momentum of the incident photon is small compared to that of other excitations and its magnitude can be taken to be zero. For homogeneous, linear, isotropic materials the dielectric function does not depend on the polarization of the incident light and so it can be written as a frequency dependent scalar $\epsilon(\omega)$. In general, the dielectric response is

complex and can be written as [26]

$$\epsilon(\omega) = \epsilon_1(\omega) + i\epsilon_2(\omega) = \epsilon_1(\omega) + \frac{4\pi i\sigma_1(\omega)}{\omega}, \quad (2.38)$$

where ϵ_1 is called the real part of the dielectric function and σ_1 is the real part of the complex conductivity. For zero frequency ($\omega = 0$), these two quantities become the static dielectric constant ϵ and the DC conductivity σ_{de} respectively.

Optical experiments do not measure $\epsilon(\omega)$ directly, but instead measure the the reflectance or transmittance of a given material. The dielectric response is then calculated from these results. The reflectance and transmittance are most easily described in terms of the complex index of refraction $N(\omega)$, which may be written in terms of its real and imaginary parts, the refractive index $n(\omega)$ and the extinction coefficient $\kappa(\omega)$. These functions are in turn related to the dielectric response function by [26]

$$N(\omega) = n(\omega) + i\kappa(\omega) = \sqrt{\epsilon(\omega)}. \quad (2.39)$$

For an electromagnetic wave in medium a at normal incidence on a material b , the reflectivity and transmissivity are defined as follows [27]:

$$r(\omega) \equiv \frac{E_r}{E_i} = \frac{N_a(\omega) - N_b(\omega)}{N_a(\omega) + N_b(\omega)} \quad (2.40)$$

$$t(\omega) \equiv \frac{E_t}{E_i} = 1 - r = \frac{2N_a(\omega)}{N_a(\omega) + N_b(\omega)}, \quad (2.41)$$

where E_i is the incident electromagnetic field at the interface and E_r and E_t are the reflected and transmitted fields respectively. For experimental measurements, we are usually concerned with the transmission and reflection of a incident wave through a sample of thickness d . The measured quantities are the reflectance \mathcal{R} and transmittance \mathcal{T} which, at normal incidence, are [27]:

$$\mathcal{T} = \frac{[(1 - R_s)^2 + 4R_s \sin^2 \theta] e^{-\alpha d}}{[1 - R_s e^{-\alpha d}]^2 + 4R_s e^{-\alpha d} \sin^2(\theta + \beta)} \quad (2.42)$$

$$\mathcal{R} = \frac{(1 - e^{-\alpha d})^2 + 4R_s e^{-\alpha d} \sin^2 \beta}{[1 - R_s e^{-\alpha d}]^2 + 4R_s e^{-\alpha d} \sin^2(\theta + \beta)} \quad (2.43)$$

where $\beta = n\omega/cd$, θ is the phase shift of the incident wave on reflectance at the internal surface, R_s is the single bounce reflectance, defined as:

$$R_s = rr^* = \frac{(1 - n^2)^2 + \kappa^2}{(1 + n^2)^2 + \kappa^2}, \quad (2.44)$$

and α is the absorption coefficient,

$$\alpha = \frac{2\omega\kappa}{c}. \quad (2.45)$$

For thick samples, variations in thickness lead to a loss of phase coherence, thus it is sufficient to add intensities, leading to:

$$\mathcal{T} = \frac{(1 - R_s)^2 e^{-\alpha d}}{1 - R_s^2 e^{-2\alpha d}}. \quad (2.46)$$

In the case of photoinduced transmission measurements, the quantity measured is the change in transmission $\Delta\mathcal{T}$. If this is normalized by the unexcited

transmission \mathcal{T} , it can be written:

$$\frac{\Delta \mathcal{T}}{\mathcal{T}} = \frac{\frac{(1-R_s)^2 e^{-(\alpha+\Delta\alpha)d}}{1-R_s^2 e^{-2(\alpha+\Delta\alpha)d}} - \frac{(1-R_s)^2 e^{-\alpha d}}{1-R_s^2 e^{-2\alpha d}}}{\frac{(1-R_s)^2 e^{-\alpha d}}{1-R_s^2 e^{-2\alpha d}}} \quad (2.47)$$

If the arguments in the above equation are expanded in terms of αd and assuming the change in absorption is small ($\Delta(\alpha d) \ll 1$), the above equation can be reduced to:

$$\frac{\Delta \mathcal{T}}{\mathcal{T}} \approx -\Delta(\alpha d) \quad (2.48)$$

2.5.2 Determination of Film Thickness From Interference Fringes

This fringe can be used to determine the fringe thickness. For a plane wave incident on a thin film, part of the light transmitted through the front surface is reflected off the back surface of the film. The same occurs at the front surface to the wave reflected off the back surface. For wavelengths of light comparable to the film thickness, these multiply reflected amplitudes will add coherently. The phase difference between two successive internal reflections of a wave is [12]:

$$\Delta\theta = \frac{4\pi n d}{\lambda_0} \cos(\phi), \quad (2.49)$$

where ϕ is the angle between the internally reflected wave and the surface normal, n is the index of refraction of the film and λ_0 is the wavelength of the incident wave in free space. Using Equation 2.49, we set the phase difference to 2π , assume normal incidence, so $\phi = 0$, replace $1/\lambda_0$ with the difference in wavenumber between two

successive peaks in transmittance, $\Delta\omega$ and solve for d , leading to:

$$d = \frac{1}{2n\Delta\omega}. \quad (2.50)$$

2.5.3 Modeling Absorption

Absorption occurs in a material when the incident light is converted into another form of energy. There are many avenues of absorption: free (conduction) electrons absorb near their plasma frequency; lattice vibrations provide another method; photons of energies higher than the band gap of a semiconductor can cause interband transitions between the valence and conduction bands.

The Drude model is used to describe free carrier effects. For the Drude model, the carriers are assumed to be independent of interactions with the ions and other carriers, except during collisions. Collisions are assumed to be instantaneous. They occur with probability $1/\tau$ and are the only method for the carriers to reach thermal equilibrium [28, 29]. The Drude model describes the dielectric function as [28, 26]:

$$\epsilon(\omega) = 1 - \frac{\omega_p^2}{\omega^2 + i\omega\tau}, \quad (2.51)$$

where ω_p is the plasma frequency defined by the following equation:

$$\omega_p^2 = \frac{4\pi ne^2}{m^*}. \quad (2.52)$$

where n is the number density of the free carriers and m^* is their effective mass.

For bound carriers, the Lorentz model is used [26]. The Lorentz model assumes the electrons to be bound to the ion cores by a harmonic potential. It is also valid

for modeling lattice vibrations (phonons). The Lorentz model is a sum of responses for each of the bound charges or lattice vibrations (called oscillators). The Lorentz model is written as [26]:

$$\epsilon(\omega) = 1 + \sum_j \frac{\omega_{pj}^2}{\omega_j^2 - \omega^2 - i\omega\gamma_j} \quad (2.53)$$

where ω_{pj}^2 , ω_j and γ_j are the oscillator strength, resonant frequency and damping coefficient of the j^{th} oscillator. The oscillator strength, ω_{pj}^2 is defined in the same way as in Equation 2.52, with the effective mass m_j^* and number density n_j of the j^{th} oscillator replacing those of the free carriers. Note that if the resonant frequency is zero, the Drude model is recovered with the damping coefficient $\gamma_{Drude} = 1/\tau$.

2.5.4 Sum Rule

Equation 2.52 can be solved for n_j to yield the number density of carriers as a function of oscillator strength,

$$n_j = \frac{m_j^* \omega_{pj}^2}{4\pi e^2}$$

This formula leads to the sum rule, which states that the total number of carriers in a system must be conserved, therefore, oscillator strength removed from one frequency must be added somewhere else to maintain a constant total carrier density. Formally written the sum rule for oscillator strength is [26]

$$N_{tot} = \frac{2m^* V_{cell}}{\pi e^2} \int_0^\infty \sigma_1(\omega') d\omega' = \text{constant}, \quad (2.54)$$

where N_{tot} is the total number of carriers per unit cell of volume V_{cell} .

CHAPTER 3 EXPERIMENT

3.1 Introduction

The experiments described in this dissertation were conducted on the U12IR beamline of the National Synchrotron Light Source (NSLS) VUV ring at Brookhaven National Laboratory. The U12IR beamline has two end stations which can be used for infrared (IR) spectroscopy [30]. One is a Bruker IFS 113V spectrometer which can cover a frequency range of 20 cm^{-1} to $10,000\text{ cm}^{-1}$. The other is a lamellar grating interferometer which is geared for the $2\text{-}100\text{ cm}^{-1}$ range [31]. The experiments involve using a laser synchronized with the IR pulses from the synchrotron to perform pump-probe spectroscopy (see Figure 3.1). Pump-probe spectroscopy uses an energy source (the pump pulse) to excite a material. An arbitrary, but selectable time later, the probe pulse comes and samples the material state. To generate a full decay measurement, spectra over a range of decay times are taken. This method is limited in time resolution by the cross-correlation of the pump and probe pulses. In the case of these experiments, the laser (pump) pulse is a few ps and the synchrotron pulse length is $0.3\text{ - }1.5\text{ ns}$ and is thus the limiting time scale. This chapter will describe the details of the experimental apparatus. It will include details on the synchrotron, beamline and pump laser. It will also provide a description of the two spectrometer end stations, including comparisons of sources. Methods of bringing the laser pump beam to the samples will also be discussed.

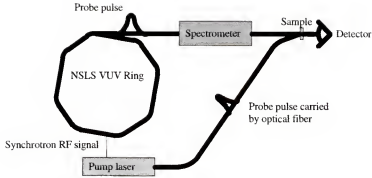


Figure 3.1: Diagram of the pump-probe measurement system.

3.2 NSLS VUV Ring

The VUV ring normally operates at an energy of 800 MeV with an RF frequency of 52.9 MHz. The ring circumference is 50 m leading to 9 RF "buckets" that may be injected with electrons. In normal operations the average current is close to 500 mA and the average beam size is $550 \times 185 \mu\text{m}$ [32]. The 9 buckets can be arbitrarily filled leading to a number of possible ring conditions. However, for timing purposes, only the symmetric fills are useful. When running in 9 bunch mode, every bucket is filled and the PRF of the synchrotron is the same as the RF cavity frequency of 52.9 MHz. Another useful mode is the so called 7 bunch mode. In this mode 7 of the 9 buckets are filled. Due to instabilities in the electron orbit caused by having all 9 buckets filled, the 7 bunch mode is the most commonly used in the day to day operations of the ring. It provides a stable, reliable template with the maximum current available. The two other interesting modes are single bunch and 3 bunch symmetric. In single bunch mode, only one bucket is filled, leading to a PRF of 5.9 MHz. In 3 bunch symmetric mode every 3rd bunch is filled yielding a PRF of 17.6 MHz. Because of the limitations of some materials in the

ring, the 3 bunch and single bunch modes must be run with lower current. Many of the other experiments on the VUV ring depend strongly on the output power of the beam and may suffer from low signal to noise when the ring is run with lower currents. For this reason, these modes are not used during normal operations and are only used by request during after midnight shifts, weekends and special timing periods.

For 7-bunch operations, several special configurations have been developed by the RF group to assist in timing measurements. During normal operations, a RF cavity with resonant frequency 4 times that of the ring RF (called the 4th harmonic cavity) is powered. This cavity helps stretch the electron bunches which in turn increases the beam lifetime. The longer lifetime allows higher average current and fewer fills, leading to less thermal cycling for parts exposed to the beam and to a lower radiation dose. (Stray radiation comes primarily during injections.) However, broader pulses implies lower time resolution. For timing experiments with resolution better than 1 ns, other modes must be used. For intermediate time resolution, a so-called 7-bunch detuned mode is used. In this mode, the 4th harmonic cavity is powered down leaving the bunches unstretched. This provides bunch lengths of 500–700 ps, depending on the ring current. The 7-bunch detuned mode is capable of running at a full current, but has approximately half of the lifetime of that achieved in normal operations (7-bunch stretched). For better time resolution, a third configuration has been developed, called 7-bunch compressed. In this mode, the RF/2 cavity (also used to stretch the bunches) is run 180 degrees out of phase and thus compresses the bunches. This mode shows an onset of coherent emission at low currents and is thus limited to currents below

Parameter	Value
Circumference	51.0 m
Peak Current	1.0 A
Average Current	518 mA
Energy	808 MeV
Orbital Period	170.2 nsec
RF Frequency	52.886 MHz
Horizontal Size	536 - 568 μm
Vertical Size	170 - 200 μm

Table 3.1: Operating parameters of the NSLS VUV ring. For adjustable parameters, the values used for normal operations are shown here.

Parameter	Value
Bending Radius	191 cm
Horizontal Opening Angle	90 mrad
Vertical Opening Angle	90 mrad
Frequency Range	1 - 10,000 cm^{-1}

Table 3.2: Parameters of the U12IR beamline. The frequency range given is that available with the current spectrometers, the beamline could be used to up to ultraviolet frequencies with a spectrometer with corresponding limits.

~ 120 mA. Using 7- bunch compressed, synchrotron pulses on the order of 300 ps have been achieved. Table 3.2 shows some the possible operating parameters of the NSLS VUV ring for timing measurements. For many timing measurements, 7 bunch stretched or 7 bunch detuned operations are used. One may be led to believe that the 2 empty bunches may cause some problems for the measurements. However, this is not the case. For all the timing measurements the laser pump is used and arrives at some time Δt before the probe pulse. The 2 empty bunches do not excite the detector and thus have no effect on the spectrum.

Param. (unit)	$7b_{stretched}$	$7b_{det}$	$7b_{comp.}$	3b	1b
Fill pattern (-)	0011111111	0011111111	0011111111	001001001	100000000
I_{max} (mA)	1000	1000	120	600	400
l_{bunch} (cm)	36	15	9	20	30
τ_{eff} (min)	300	200	300	150	100
τ_{pulse} (ns)	18.9	18.9	18.9	56.7	170.2

Table 3.3: Operating parameters of the NSLS VUV ring for various modes used for timing experiments. For the fill pattern, a ‘1’ indicates a filled bucket, a ‘0’ indicates an empty one. I_{max} is the maximum allowed current for that mode, l_{bunch} is the electron bunch length, τ_{eff} is the nominal lifetime of the ring current and τ_{pulse} is the time between pulses.

3.3 General Beamline Description

The U12IR beamline is a dedicated IR beamline with a large extraction angle port (90 mrad x 90 mrad) located near the end of the sixth dipole magnet [30]. The large angle allows the efficient extraction of light down to the 10s of cm^{-1} range. The light is collected by a water-cooled gold coated mirror and reflected up out of the plane of the ring. There are then 2 steering mirrors that direct and refocus the beam through a 0.5 inch (1.27 cm) diameter CVD diamond window used to separate the ring side UHV ($\sim 10^{-9}$ torr) from the rough vacuum (20 mtorr base) of the collimating optics and spectrometers. The diamond window has a 0.5° wedge to prevent “fringes” in the spectra due to multiple internal reflections in the window. On the ring side of the diamond window there is a large cone used to help collect the longest wavelengths and guide them through the diamond window. See Figures 3.3 and 3.2.

Once through the window, the beam enters the collimating box where there are two possible configurations leading to two spectrometers. One configuration has a short piece of light pipe or a cone leading into light pipe immediately after the

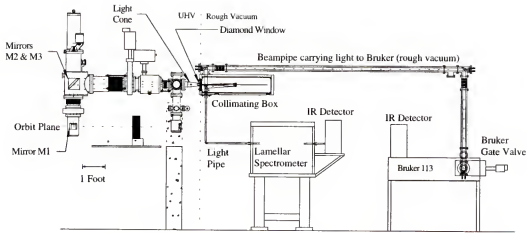


Figure 3.2: Elevation view of the U12IR beamline.

diamond window. In this configuration the cone before the diamond window collects and guides the long wavelength light into the light pipe. Initial experiments were conducted with the light being coupled into 0.5 inch diameter light pipe immediately after the diamond window. The light pipe then makes a turn down and out of the box and then brings the light into a lamellar grating spectrometer. This spectrometer is used in the very far IR region of $2\text{--}100\text{ cm}^{-1}$. The light pipe optics are non-focusing so the brightness advantage of the synchrotron is lost, however, the pulsed nature of the source makes it still useful for time resolved measurements and below 20 cm^{-1} the low frequency power advantage of the synchrotron gives it more power than the thermal source used in this spectrometer.

The other configuration has the light pipe removed with the beam collimated by a paraboloid mirror located approximately 50 cm from the diamond window. It is then reflected by a series of mirrors through an evacuated pipe and brought into a Bruker IFS 113v spectrometer. The Bruker can measure spectra from $20\text{--}10,000$

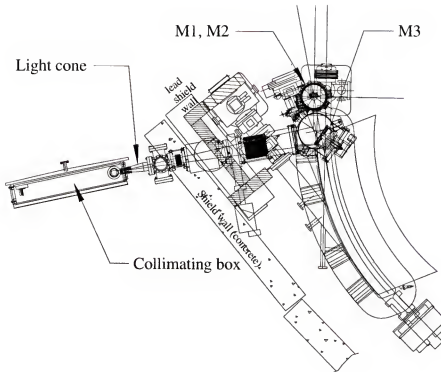


Figure 3.3: Plan view of the U12IR beamline up to the collimating box.

cm-1 using various beam splitters and detectors. The Bruker can make use of the small source size to measure samples scales on the order of 1 mm^2 or smaller. In this configuration there is no gain from the 6 degree cone in front of the diamond window. The additional angle introduced by the cone would cause any ray that hit the cone surface to miss the collimating paraboloid. The Bruker has a gate valve with a glass window in the gate to allow visual alignment with the Bruker vented to atmosphere while keeping the collimating box and pipe and steering optics under vacuum. Once a reasonable alignment has been achieved, the Bruker can be pumped, the gate valve opened and fine alignment can be started, followed by measuring spectra.

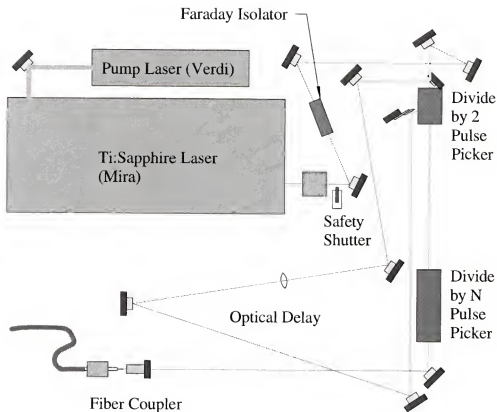


Figure 3.4: Diagram of the optical layout of the laser system.

3.4 Pump Laser System

For the time resolved measurements, the pump pulse is provided by a Mira mode- locked Ti:sapphire laser that may be synchronized with the synchrotron pulse. The laser was custom built by the Coherent Inc. Laser Group. In order to maintain stable operation, the laser was required to operate with a PRF of 105.8 MHz, twice that of the VUV ring, instead of the ring's 52.9 MHz PRF. See Figure 3.4 for a diagram of the laser and pulse picker arrangement. At the output of the Mira there is a shutter. This shutter is interlocked with the door of the laser

hutch for safety purposes, such that if an unauthorized person enters the hutch without triggering the interlock bypass, the shutter will close and thus reduce the possibility of injury to that person by a stray beam. Following the shutter is a Faraday isolator. This is an electro-optic device used to prevent back-reflections of downstream optics from reentering the laser cavity and causing instabilities. After the Faraday isolator, the beam passes through a pair of cylindrical lenses used to correct a slight eccentricity in the beam cross-section.

In order to reduce the PRF of the laser to match that of the synchrotron, an electro-optical “pulse picker” made by Conoptics Inc. is used. The device is a Pockels cell which rotates the polarization of every other pulse by 90 degrees. The beam then passes through a polarizing beam splitter with the result that every other pulse is rejected. In order to recover some of the power lost by having to divide the PRF, the rejected pulses are recycled. After exiting the pulse picker, the rejected pulse is optically delayed and its polarization is rotated back to its original state by a half-wave plate. Coincidence between the recycled and following pulse was achieved by adjusting the length of the optical delay until the pulses were indistinguishable using a fast photodiode (~ 50 ps rise time, see Figure 3.5). The delayed pulse is then re-injected next to the following pulse as it enters the pulse picker. Both pulses are passed with an increase in power of approximately 80% over the single pulse. As mentioned in Section 3.2 the NSLS VUV ring can be run with multiple PRFs. For 7 or 9 bunch operations, the single pulse picker is adequate to bring the laser into coincidence with the ring. However, for 3-bunch symmetric and single-bunch mode (17.6 and 5.9 MHz PRF respectively), another pulse picker is required. The second pulse picker uses the same concept as the first,

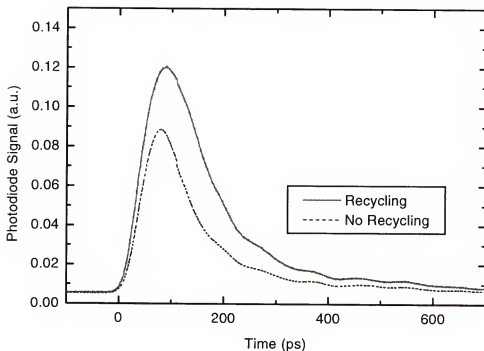


Figure 3.5: This figure shows the effects of the pulse recycler for the “divide by 2” pulse picker. The rise time for the photodiode is ~ 50 ps. The rise times of the two curves are similar and the pulse widths (FWHM) differ by ~ 30 ps, thus the two pulses are well stacked compared to the synchrotron pulse with minimum pulse width of 300 ps. The 80% difference in pulse energy after recycling is given by the difference in integrated area under the curves.

the main difference being that it has a selectable rate, so that every n th pulse may be passed, where n is some integer. Figure 3.6 shows the result of the various pulse pickers on the laser pulse train. Currently, the rejected pulses from the second pulse picker are not recycled.

After the laser is passed through the pulse pickers it enters a fiber coupler where it is focused into a fiber optic cable for transport to the beamline. The fiber allows the laser and beamline to be separated making it possible to house the laser in a secure room and freeing up valuable space in the beamline area. The fiber also

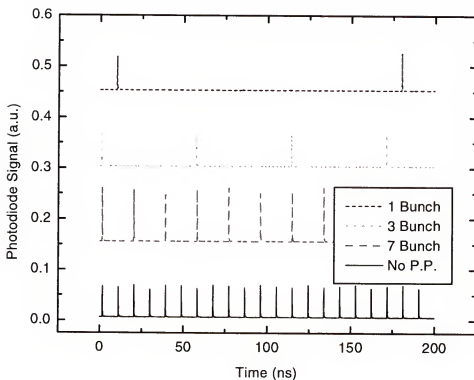


Figure 3.6: Effects of the pulse pickers on the laser pulse train. From bottom to top, the curves show the laser pulses with no pulse pickers, just the “divide by 2”, and also after the “divide by N” pulse picker set for 3 bunch symmetric and single bunch modes. Variations in peak height are due to undersampling by the digital oscilloscope and do not reflect power fluctuations in the laser.

makes it possible to conveniently transport the laser pulses to other beamlines for time-resolved experiments there.

The laser is maintained at a selectable relative to the synchrotron pulse through the use of a program provided by Coherent called Synchro-lock. Figure 3.7 shows a diagram of the current system. The program allows the user to lock the laser to the synchrotron and also allows phase modulation between the two making derivative measurements possible. The laser software was designed to operate only at the ring PRF of 52.9 MHz. For other PRFs, there is no convenient method

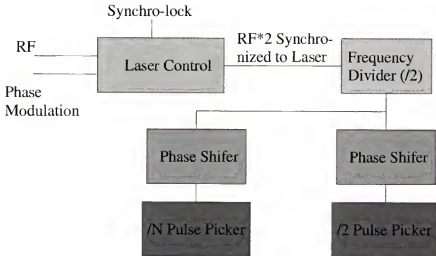


Figure 3.7: Diagram of the timing signals used at present for the synchronization and pulse picking electronics. With this configuration, using the frequency divided 106 MHz output of the laser, instabilities in the electronics can lead to the pulse pickers moving to an incorrect phase. Figure 3.8 contains a diagram of a proposed unit using a frequency multiplied RF/9 signal which overcomes these and other problems.

for locking and maintaining the lock between the laser and the synchrotron. This causes some trouble for all the measurement methods. The first problem lies with the fact that the laser actually operates at 105.8 MHz, while the synchronization program is running at 52.9 MHz. The first pulse picker operates on a divided signal output from the laser, so it will be in phase with the laser no matter the laser time delay. However, if the laser loses mode lock, when it regains lock, the divided frequency may be out of phase by 180° , shifting the delay between the pump and probe pulses by ~ 9 ns. The laser occasionally loses lock due to instabilities and each time this happens, the correct phase must be confirmed. A second similar problem arises when running at PRFs lower than 52.9 MHz. The basic problem lies with the fact that the laser is synchronized to the 52.9 MHz RF signal, and

part is similar to one described above. To lock and operate it at a lower frequency, requires some division of the RF signal to bring it down to the RF/9 or RF/3 frequencies. This causes two problems with controlling the laser. First, the laser control can only shift the phase up to 9 ns, a small fraction of the necessary phase delay required for 3 bunch or 1 bunch operations. The second problem is there is more than one possible phase for the laser to synchronize to using the divided RF signal. For 3 bunch operations, there are 6 phases to which the laser can possibly be synchronized (105.8 MHz/17.6 MHz). Similarly, for 1 bunch there are 18 possible phases. To correct this, a custom phase shifting unit has been designed by the staff at UF and the NSLS. This unit will make use of a signal synchronized to a particular bucket in the ring called RF/9. The RF/9 signal of the synchrotron operates at a frequency of 6 MHz. The new phase shifter makes use of the RF/9 signal to generate functions used to drive the laser and the pulse pickers. It will allow a full 170 ns time delay making a complete measurement convenient in single bunch mode. All other PRFs for the pulse pickers are derived from the RF/9 signal. This prevents hopping from one phase to another in the event the laser loses lock or some electronic instability occurs. See Figure 3.8 for a diagram of the proposed system. At the time of this writing construction of this multiple phase shifter had not been completed.

3.4.1 Mode-locked Ti:sapphire Laser

The Mira is a mode-locked ultrafast laser that uses Ti:sapphire as the gain medium and is tunable from 700 to 1000 nm. It has two power configurations, depending on the pump source. The unit described in this dissertation uses

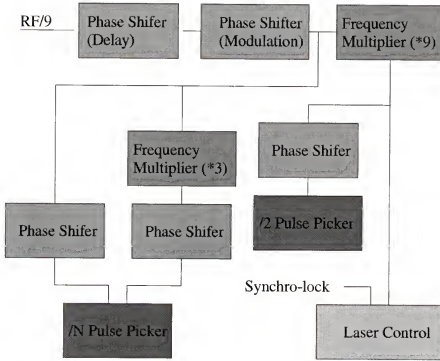


Figure 3.8: Diagram of the proposed unit for generating timing signals for the synchronization and pulse picking electronics. With this configuration, using a frequency multiplied RF/9 signal, possible phase hopping is avoided.

a Coherent Verdi pump laser. The Verdi is a diode-pumped frequency-doubled Nd:Vanadate laser. It produces a single frequency 532 nm (green) output beam with power levels up to 5.5 W. The Verdi uses power tracking software to insure stable operation. Using the Verdi pump, the Mira is capable of a maximum output of 1 W with an average output of 800 mW. The Mira mode-locking technique is called Kerr lens mode-locking [33, 34]. The Mira laser cavity takes advantage of the Kerr effect in the Ti:sapphire crystal which self focuses the beam. This self focusing leads to higher gain in mode-locked operation than in CW mode. To further discriminate against CW operation, a slit is placed in a location where

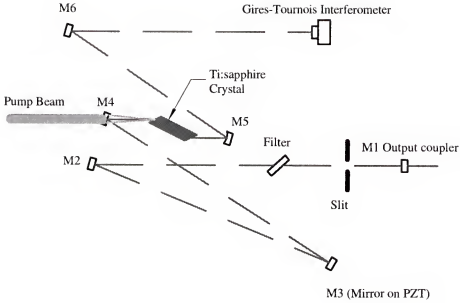


Figure 3.9: Optical diagram of the Mira Ti:sapphire laser cavity.

the mode-locked beam's cross-section is smaller than that of the CW beam. See Figure 3.9 for an optical schematic of the Mira.

The Mira laser has three modes of operation. It can operate in continuous wave (CW), mode-locked (ML) or beta-locked (β L) modes. The CW mode is used during alignment when the laser is first started during the day. It is also used for steady-state photoinduced measurements. The Mira is put in ML mode for time resolved measurements. In this mode, the laser mode locked and can be synchronized to the ring RF. For mode-locked operation, the cavity length must be an integer number of the laser wavelength. This can be achieved by either tuning the frequency of the laser until the frequency matches the resonant frequency of the cavity, or the cavity length can be adjusted until it's resonance is tuned to the laser frequency. The laser is tuned by micrometer adjustment of a birefringent

filter. The cavity length can be varied by applying a constant voltage to the PZT mirror (M3). Either one of the methods is effective in adjusting the laser until mode-locked operations are possible. Beta lock is an automated form of mode-locking. In the beta lock mode, the Gires-Tournois interferometer (GTI) mirror is dithered until the laser achieves mode-locked operation. Once mode-locked, the dithering is stopped and the GTI is kept at a constant voltage. If a loss of lock is detected, the GTI will once again be dithered until mode-locked operation is regained.

3.4.2 Photoinduced Measurements

There are several methods for using the laser in photoinduced measurements. As mentioned above, the laser can be placed in CW mode for steady-state photoinduced measurements. The laser can also be placed in ML or β L modes and operated unsynchronized to the ring. For the plain photoinduced measurements there are two methods of collecting spectra. First, the laser can be chopped and a difference signal (laser on - laser off) detected by a lock-in amplifier. The second method is to take spectra in the normal fashion for the particular spectrometer with the laser on and laser off and then take the difference of these two spectra. In the case of a fast scan bench, this is the only option available.

For time resolved measurements there are also several options. One is to simply synchronize the laser with the ring and then take a series of photoinduced spectra as described above. Each spectrum would be taken with a different delay between the laser and synchrotron pulses and in this way, the time evolution of the photoinduced spectrum can be measured. Another way, less sensitive to heating effects

and more sensitive to small signals it to dither the laser delay and use lock-in techniques to measure the derivative signal. The laser delay can be adjusted by the actuation of a mirror located on a piezoelectric transducer (PZT). The PZT moves the mirror slightly, making changes in the cavity length and thus changing the delay time between pump and probe pulses. Because the laser is irradiating the sample at all times, the sample does not undergo the relatively larger swings in temperature possible if the laser is chopped. Thus the dithered method provides the least sensitivity to sample heating. A series of differential spectra are taken and after a full set, they can be integrated to give the time dependence of the photoinduced response.

In the ideal experiment, the laser dithering is the method with the greatest sensitivity and least trouble from heating. However, in a real experiment it does have some drawbacks. First, the PZT has a bandwidth on the order of a kHz. For derivative measurements the ideal dither signal is a square wave. From the standpoint of intrinsic noise, a high frequency dither would be the most desirable. However, because of the limited bandwidth of the PZT, high frequency dithers are not possible. As the frequency increases, the higher harmonics introduced by the square wave eventually drive the PZT to exceed its maximum safe current. This occurs because PZT cannot keep up with the higher harmonics of the square wave. When used with bolometric detectors (the detector used in all the dithered experiments described in this dissertation) the loss is not so significant because the detector response is limited to a few kHz, but in all cases the PZT is what limits the maximum usable frequency. One possible solution is to use a sine dither. This allows the frequency to be increased by a factor of 2-4 over the square wave.

However, the sine dither requires a deconvolution to acquire the real derivative signal. The second problem of the dithered measurement also stems from the PZT. In this case, it is caused by the motion of the PZT during dithering. Because the PZT mirror, M3, is not an end mirror of the cavity, as it moves back and forth the beam walks slightly. During dithering, if the beam is not well centered on the output slits, the beam can move across the slit causing power fluctuations. These fluctuations, which are in phase with the dithered signal, can be misinterpreted as false signals if the sample shows a large steady state photoinduced response, relative to the time-dependent response. They should be easy to remove because the spurious signal generated by these fluctuations should be constant with laser delay. They may also be eliminated using a reference photodiode before the sample and dividing the measured signal by the reference signal, however, this method has not been implemented. In the case of a large error, the spurious signal can mask the determination of coincidence by keeping the signal sign the same for all delays. This effect can be minimized by directing the output of a photodiode to a lock-in amplifier in the laser hutch. The slit width and position are then adjusted to minimize the power fluctuations caused by the dithering.

3.5 Lamellar Grating Interferometer

3.5.1 Description

The lamellar grating interferometer covers a frequency range of $2\text{--}100\text{ cm}^{-1}$ [31]. Infrared light from the synchrotron is brought into the spectrometer by a 0.5 inch diameter brass light pipe (see Section 3.3.) A small break in the pipe allows a

- 1) Entrance Lightpipe
- 2) Internal Source Lightpipe
- 3) Internal Source (Hg Arc)
- 4) Chopper Assembly
- 5) Stepper Motor
- 6) Micrometer
- 7) Lamellar Grating
- 8) Exit Lightpipe
- 9) Collimating Mirror
- 10) Focusing Mirror

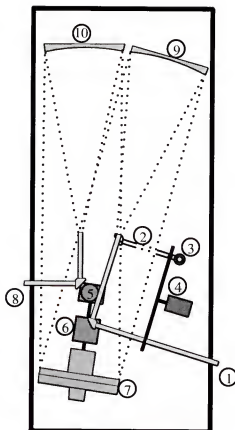


Figure 3.10: Diagram of the lamellar grating spectrometer.

chopper blade to pass for use with a lock-in amplifier to measure absolute spectra. The light pipe makes a 90 degree turn and ends at the focus of the spherical mirror used to collimate the light onto the grating. The collimated light is reflected off the grating to a matched spherical mirror that focuses the light into the entrance of the exit light pipe. The light pipe then carries the light out of the spectrometer where it can be passed through a sample and into a detector (see Figure 3.10). Refer to Section 2.2.2 for a discussion of how the lamellar grating works and a theoretical comparison between it and other spectrometers.

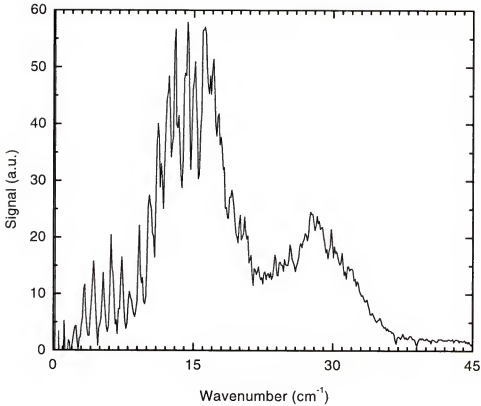


Figure 3.11: This plot shows the comb structure due to a reduced number of modes in the light pipe at low frequencies and selective coupling into those modes by the straight 6 deg cone just before the diamond window in the collimating box.

The spectra from the first experiments showed a comb structure at the lowest frequencies ($< 20 \text{ cm}^{-1}$, see Figure 3.11). The features were not evident in spectra taken with the Bruker, and it was determined that this structure was caused by the cone immediately before the diamond window. The straight 6 degree cross section of the cone caused the incident light to be reflected through the window and into the light pipe at only a few selected angles. As the wavelength of the light approaches the size of the light pipe, the number of modes available for transporting the light is decreased. This reduced number of modes selectively couple to only certain

narrow ranges of input angles of the incident light. Therefore, only frequencies whose modes were compatible with the few incident angles were efficiently coupled into the light pipe. The comb function was sharp enough that it made taking accurate data at resolutions higher than 4 cm^{-1} impractical. In an effort to help reduce the comb function, the short section of light pipe just after the diamond window was replaced with a Winston cone [35, 36]. A non-imaging optic, the Winston cone takes all the light that enters the entrance aperture within a certain entrance angle and focuses it through the exit aperture. For our purposes, the important thing is that the cone has a curved cross section, giving the light a continuous range on entrance angles into the light pipe. The Winston cone had some effect on the comb function, however this was at the cost of a large reduction in signal at the lowest frequencies. Figure 3.12 shows a comparison of spectra taken with and without the cone in place. The reduction in signal is due to the extra angle introduced by the Winston cone. The longest wavelengths once guided into the light pipe by the Winston cone have such a sharp exit angle from the light pipe that they miss the collimating mirror in the lamellar. A possible future upgrade would replace the upstream straight cone with a Winston cone, or replace the light pipe with a larger diameter waveguide. The larger diameter light pipe would have more modes available at the lower frequencies and thus not present as large a problem. Another possible solution would be to replace the light pipe with fast imaging optics and avoid the mode problems altogether.

For experiments performed between 3.5 K and 300 K, an APD Helitran flow cryostat was used. For lower temperatures or cases where sample heating by the laser could have strong or adverse effects, an Oxford Optistat bath immersion

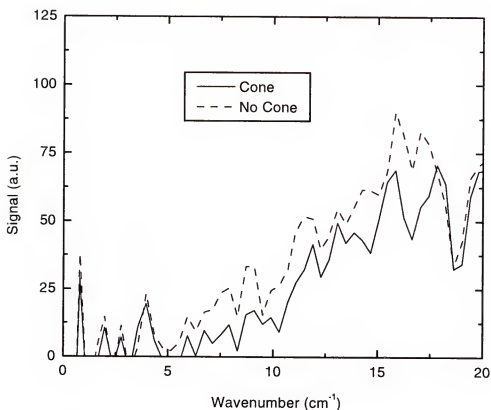


Figure 3.12: Effects of the addition of a Winston cone just behind the diamond window. The purpose of the Winston cone was to reduce the comb structure seen in Figure 3.11 by improving the coupling into the low frequency modes. The cone failed to significantly improve the comb structure and caused a large reduction in the low frequency signal.

cryostat was used. See Section 3.5.2 for more details on laser injection with the lamellar grating spectrometer.

For computer control of the lamellar, custom code with a WindowsTM interface was written by Dr. R.P.S.M. Lobo. The code allows for easy acquisition of data with the ability to choose resolution, apodization, averaging time and a host of other features. Custom code for measuring signal decays as a function of time was also written by Dr. Lobo.

3.5.2 Laser Insertion

For transmission measurements with the lamellar grating, an apparatus was designed and constructed to allow the laser pump pulse to be injected parallel with the probe pulse carried by the light pipe. This approach consists of two attachments to a standard APD Helitran shroud. The attachments take the place of the windows that would normally be used to seal the cryostat sample space. One attachment allows the insertion of an optical fiber carrying the NIR pump pulse into the light pipe. The fiber ends approximately 1.5 inches from the sample and has a 0.5 inch range of motion along the axis of the light pipe. With the optional addition of a gradient index lens, this allows the spot size of the excitation pulse at the sample to be adjustable from 3/16 to 1/2 inch diameter. On the exit side, there is another attachment to the Helitran. This one has a window near the Helitran to keep the Helitran volume separate from the exit light pipe section. It also has a fitting to allow the exit light pipe section to be evacuated, removing absorptions due to air (primarily from H_2O and CO_2). The attachment ends in an adapter designed to fit a bolometer detector with a flange for use with a Nicolet spectrometer. Figure 3.13 is a diagram of the attachments designed for the Helitran.

To attain lower temperatures and in situations where sample heating by the laser could be a problem, a Oxford Instruments Optistat Bath immersion cryostat may be used. The Optistat bath circulates temperature stabilized helium gas or liquid through the sample chamber. For samples with low thermal conductivity the circulating gas or liquid can remove heat due to the laser excitation faster than the Helitran. Pumping on the exhaust allows sample temperatures as low as 1.5 K to be reached. For the immersion cryostat, adaptors were designed and

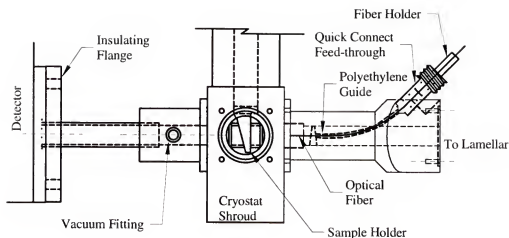


Figure 3.13: Drawing of the attachments to the Helitran cryostat shroud allowing laser insertion. For the lamellar, with this method the laser radiation is parallel to the synchrotron pulses.

constructed that allow the use of the existing hardware of the for laser injection and carrying the probe light to the sample and the detector in use for the Helitran. See Figure 3.14.

3.5.3 Measurement Methods

For measuring absolute transmittance, the source is chopped and the detector signal is fed to a lock-in amplifier. Depending on the signal-to-noise ratio, the signal is averaged from 100 msec to up to 10 or more seconds. Once the point is taken, the grating is stepped and the after a short wait to allow mechanical vibrations due to the step to dissipate, averaging for the next point is begun. The procedure is repeated until an entire interferogram is sampled. Then, with a choice of apodizations, the interferogram is Fourier transformed and the power spectrum recovered.

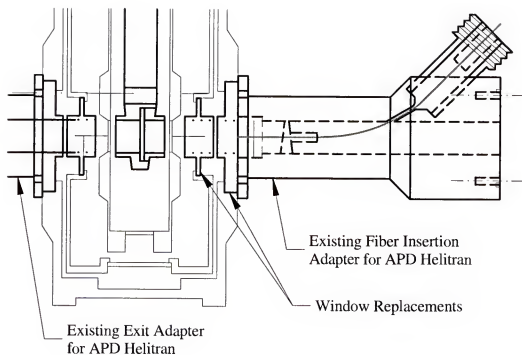


Figure 3.14: Drawing of the adapters to the Oxford immersion cryostat allowing laser insertion through the use of pieces designed for the Helitran.

For steady state photoinduced measurements there are several different methods that may be used to collect spectra. One way is to simply take absolute spectra with the excitation on and off and then take the difference. This method, while simple, produces poor results if the photoinduced effects are relatively small. For steady state photoinduced measurements, a second method can be used. In this method, the laser is put in CW mode and the beam is passed through a chopper. A synchronous reference signal from the chopper is fed into a lock-in amplifier. The lock-in amplifier rejects signals which are not in phase with the reference signal from the chopper, acting as a narrow band pass filter and allowing more accurate measurements. The output signal from the lock-in is the difference between the

signal with the laser excitation on and off, so that a difference spectrum is directly generated. This method allows the study of weaker signals, however it has the drawback of being susceptible to false signals caused by sample heating. If the sample has any temperature dependence in its transmittance, even a small amount of heating can cause spurious results.

For time resolved measurements, there are two possible measurement methods. The first method is to directly measure the photoinduced signal at different delay times using the a chopped laser as described above. In order to generate time resolved spectra, the laser is mode locked and synchronized to the ring RF frequency. Then a series of spectra at variable delays is taken to generate the time-resolved spectra. This method is still susceptible to false signals due to sample heating. To minimize the heating effects, differential spectra are taken between two time delays. Instead of chopping the laser, the delay is modulated by a low frequency(10s - 100s of Hz) sine or square signal. The lock-in uses the modulation signal as a reference and rejects “static” signals. In most cases heating occurs on the ms to us time scale and appears static to the lock- in and is rejected.

After a full range of delays is measured, the differential spectra are integrated to generate the time resolved change in transmission.

3.5.4 Source Comparison

Figure 3.15 is a plot of the intensity vs frequency as measured by the lamellar for the synchrotron and thermal sources. Note that the synchrotron spectrum crosses that of the Hg arc lamp just below 20 cm^{-1} . This crossover occurs at a somewhat lower frequency than predicted by the calculations in Chapter 2. The

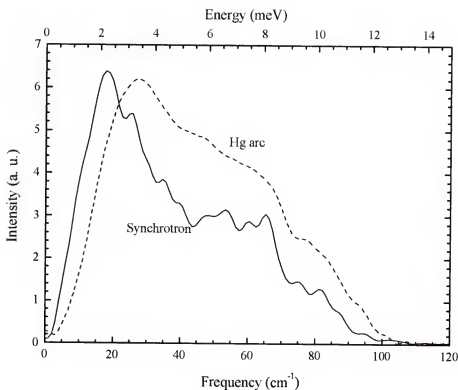


Figure 3.15: Comparison of signal strength using synchrotron and thermal sources.

explanation is the dependence of the black-body radiation on source temperature and collected angle. The source used in the lamellar is a high pressure Hg arc lamp operating at 250–300 W. Also, the lamp is housed in a cylindrical sleeve that helps collect more light and couple it into the light pipe. The result is the thermal source being competitive to lower frequencies. However, it still drops off at the longest wavelengths, and at 5 cm^{-1} the synchrotron intensity is 5–6 times greater than that of the arc lamp.

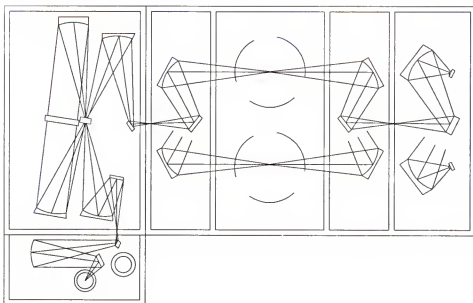


Figure 3.16: Diagram of the Bruker 113V with internal sources in place.

3.6 Bruker 113V Fast Scan Interferometer

3.6.1 Description

For all but the longest wavelengths, the instrument used on this beamline is the Bruker 113v. It is a fast scan FTIR bench with a spectral range of 20–10,000 cm^{-1} . Generally the Bruker has a set of lamps in a source box for use as light sources in the various frequencies. For the U12IR beamline, the sources and source base plate have been removed and replaced with focusing and steering optics for the synchrotron light. In place of the sources there is a flat gold mirror that steers the beam onto a spherical mirror used to focus the light through an aperture and into the interferometer chamber. See Figure 3.16 and 3.17 for diagrams of the Bruker before the source box changes and changes to the source box. Making

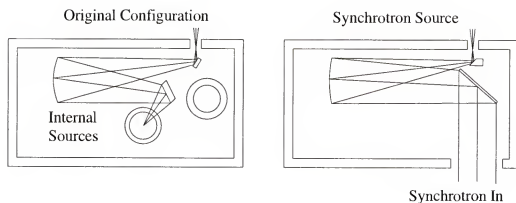


Figure 3.17: Diagram showing the changes in the Bruker source box for use with the synchrotron source. A hole was cut in the side to allow the synchrotron light to be brought into the source box. The original plate with sources and focusing mirror was removed and replaced with optics for directing and focusing the collimated synchrotron light.

use of the synchrotron as an external source for the Bruker posed some problems not evident when using the internal thermal sources. First of all, the synchrotron has some beam motion caused by noise in the RF cavity, mechanical vibrations of the magnets, etc. This is all translated into noise in the signal measured at the detector. Another problem arises due to the use of the external source when evacuating or venting the spectrometer. The assembly holding the mirrors and tube that bring the light into the Bruker are attached directly to the side of the source box. When evacuated, the atmospheric pressure outside the spectrometer causes the source box wall to bend slightly, which changes the alignment of the light coming into the spectrometer. A temporary solution has been to make alignment changes after pumping or venting. However, this practice tends to lead to long term drift of the external alignment and should be corrected at some time by reinforcing the walls of the source box.

3.6.2 Laser Insertion

For time-resolved experiments using the Bruker 113v, two methods of bringing the laser light to the sample have been developed. The first simply uses an optical fiber that has been fed into the cryostat. The fiber is brought near the sample through a small stainless steel tube which is bent to point the beam exiting the fiber onto the sample, see Figure 3.18. No effort is made to focus the light so the spot size of the excitation pulse is determined by the exit angle of the fiber and the distance from the fiber tip to the sample. This method is simple but very effective. However, it does have some drawbacks. As mentioned, there is no way to focus the light, so there is a limited range of available spot sizes. Also, constraints on the minimum bending radius and space available in the cryostat limit the angle of incidence that can be attained. Finally, with no external control, there is no way to make changes to the alignment during an experiment. If something should get bumped or otherwise changed inside the cryostat during an experiment, the only available course of action is to vent the cryostat, correct the laser alignment and then start over.

The second method for laser injection uses a fiber brought into the Bruker sample chamber. Inside the chamber are focusing and steering optics used to reflect the beam through the cryostat windows and onto the sample, see Figure 3.19. This arrangement allows a broad range of spot sizes as well as external changes that can be made while the sample stays under vacuum. The drawbacks are that the optical setup is more complicated, and there is some loss of power through the spectrometer windows. The angle of incidence for this method is limited by the requirement for the reflecting optics to not shadow the incident IR beam. But,

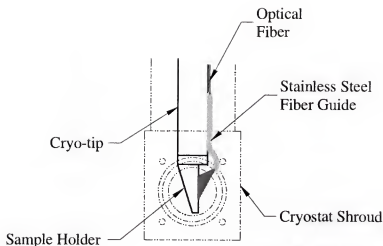


Figure 3.18: Sketch showing placement of fiber guide for photoinduced measurements. This method brings the fiber down the cryostat and uses a metal tube to aim the fiber at the sample.

the angle is much closer to normal incidence than the angle available using the previous method.

3.6.3 Measurement Methods

For the lamellar grating, the laser can be dithered at each point so that a differential measurement can be taken directly. For a fast scan bench like the 113V, this is not possible because of the scanning mirror. As the mirror scans, points are taken on the kHz scale with scan repetition rates on the order of seconds. Because of this, it is impossible to make direct differential measurements as with the lamellar. In order to generate differential spectra, a series of scans at each of two laser delays must be taken and then the spectra subtracted. This makes getting the spectra somewhat more difficult. First, there is no way to take a quick measurement to confirm that everything is working. Several scans at several delays

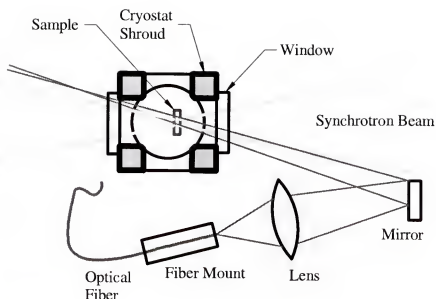


Figure 3.19: Schematic of second method of fiber insertion for the Bruker. In this case, the fiber is outside the cryostat and can be focused and aimed onto the sample. Some losses occur from the window and other optics. With this method, smaller spot sizes can be achieved. Also, the angle of incidence is closer to normal than that by the in-cryostat method.

must be taken and subtracted before it is known if a good signal is achievable. Due to the problems in measuring the differential signal with the Bruker, a different method is used to determine coincidence of the laser and synchrotron pulses. For the Bruker, the synchrotron pulses have enough power to be detected by a fast photodiode. Thus, coincidence can be measured directly. Both the laser and synchrotron pulses are focused onto the photodiode element and the output is viewed with a fast oscilloscope. The laser delay is then adjusted until the pulses are coincident.

For measuring the differential spectra, there are a few other points that make measurements with the Bruker more complicated. The Bruker macro programming

language does not allow for manipulating the interferogram before it is Fourier transformed. Also, there is no convenient way to measure an outside value such as the ring current for use in normalizing the spectra while it is being acquired. Therefore, in the case of taking differential spectra, some precautions must be taken to minimize the effect of the lack of direct beam current normalization on the data. To do this, a series of interleaved sets of scans are taken with the laser at two different delays. If each run has N sets of M scans, then the measurement routine would be as follows:

M/2 Scans at delay 0 (1)

M scans at delay 1 (1)

M scans at delay 0 (2)

.

.

.

M Scans at delay 1 (N)

M/2 Scans at delay 0 (N+1)

The M*N spectra at each delay are then averaged and the difference taken to calculate the differential spectra. The end result is that the same number of scans are taken at each delay and the difference due to ring current decay or long term drifts in the detector should be minimized by the interleaving of the scans at the two delays. The photoinduced change in absorption is calculated as:

$$\Delta(\alpha d) = \frac{\Delta \mathcal{I}}{\mathcal{I}} = \frac{\sum \mathcal{I}_1 - \sum \mathcal{I}_0}{\sum \mathcal{I}_0} \quad (3.1)$$

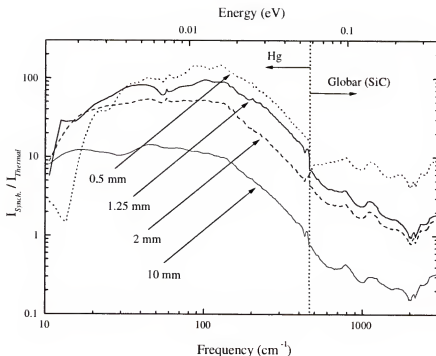


Figure 3.20: Ratio of synchrotron intensity to thermal source intensity for various aperture sizes.

3.6.4 Source Comparison

In Chapter 2 of this dissertation a series of calculations describing brightness and power advantages of the synchrotron over thermal sources were performed. These advantages dealt with ideal conditions. In this section, the actual measured differences between the sources will be discussed. In the case of the Bruker 113v, there are 2 internal sources that may be used. For the far IR, an Hg arc lamp is used, up to a frequency of 450 cm⁻¹. Above that, a SiC glowbar is used as the source.

Figure 3.20 shows a plot of the ratio of intensity for the 2 sources as measured through apertures of different sizes. The 10 mm diameter aperture essentially

passes all the light from both sources, making it a good comparison of the output power of the two sources. The synchrotron becomes comparable to the thermal sources near a 400 cm^{-1} . This is somewhat higher than expected from the calculations of Chapter 2, but can be explained by differences in source size, collection angle and source temperature. As the apertures become smaller, the synchrotron advantage becomes more evident, and for apertures near 1 mm in diameter, the synchrotron intensity may exceed that of the thermal source by two orders of magnitude for some frequencies. All intensity ratios follow a $\omega^{(-5/3)}$ power law for the range of a few thousand wavenumbers, as suggested by Equation 2.26. Above that range, the ω^4 extrapolation of the thermal source is not valid. Below a few hundred wavenumbers the synchrotron intensity decreases. This can in large part be explained by diffraction effects. Figure 3.21 is a plot of integrated intensity of the FIR region for the two sources as a function of aperture. Note that the synchrotron intensity is fairly constant down to a diameter of 2 mm.

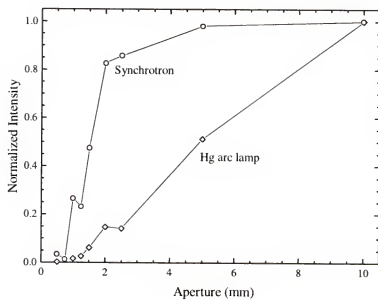


Figure 3.21: Comparison of integrated synchrotron intensity to thermal source intensity as a function of aperture size.

CHAPTER 4

TIME-RESOLVED IR STUDIES OF $\text{Hg}_x\text{Cd}_{1-x}\text{Te}$

4.1 Introduction

In this chapter we describe time-resolved response of $\text{Hg}_x\text{Cd}_{1-x}\text{Te}$ (mercury cadmium telluride or MCT) films. MCT is a well known semiconductor which is commonly used as an infrared detector. Its optical properties are well documented in the literature [37, 38]. We will then present the experimental data and discuss it in the context of these models.

The motivation for this experiment is not only for studying the physics of MCT, but also testing the experimental apparatus. Characterizing semiconductor photocarriers is related to the development of infrared detectors and thus the physics of the experiment are important. MCT provides a well studied test material with properties in the ranges attainable with the experiment as described in Chapter 3. In general, MCT has recombination rates on the order of ms for n -type and 100's of ns for p -type in the clean limit [39]. In the presence of defects, the recombination rate can be much higher. The sample used in this experiment had been left unprotected for several years. This would cause a large number of surface defects and a correspondingly high recombination rate is expected.

4.2 Optical Properties of MCT

4.2.1 Transmission

The sample measured was a $\text{Hg}_x\text{Cd}_{1-x}\text{Te}$ film on a CdTe substrate. Transmission measurements were performed using the lamellar grating spectrometer for the 10 - 60 cm^{-1} range, with a silicon boron 4 K bolometer used as the detector. The sample was mounted on a He-tran cryostat with polyethylene windows. The Bruker 113v was used for the 30–7000 cm^{-1} range. With the Bruker, a nitrogen cooled InSb detector was used. The sample was measured in the same Helitran cryostat as the FIR measurements, with KRS5 windows replacing those of polyethylene on the shroud. Figure 4.1 shows the transmittance the sample at 77 K and 300 K. At low frequencies, the spectrum is dominated by lattice vibrations in the CdTe substrate. At room temperature the band gap is near 3250 cm^{-1} , which shifts to near 3000 cm^{-1} at low temperatures. The transmittance approaches a finite value at low frequencies which is characteristic of an insulating material. At low temperatures, the thermal broadening of lattice vibrations is reduced leading to sharpening of the phonon related features. There is an oscillation in the transmittance data between 350 cm^{-1} and 700 cm^{-1} . This is an interference fringe caused by multiple reflections in the MCT film. The fringe spacing in the transmission data is 110 cm^{-1} and the refractive index for MCT is taken to be near 3.5, in reasonable agreement with the transmission data. Using Equation 2.50, this leads to a thickness of approximately 15 μm .

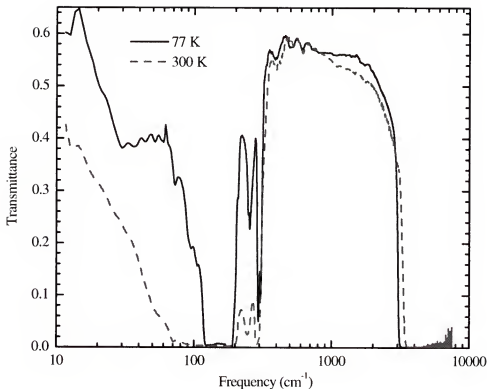


Figure 4.1: Plot of the transmittance of the MCT sample at 300 K and 77 K.

4.2.2 Time-resolved Measurements

The first time-resolved measurements were done on the lamellar with the grating fixed at zero path difference (ZPD). This gives a frequency averaged transmission through the sample, weighted by the source spectrum and instrument transmission. In these experiments, the average laser pump power was approximately 300 mW focused on the sample with a spot size of ~ 0.6 cm diameter. The ring was in 7 bunch detuned mode, leading to probe pulses on the order of 500 ps and a time between pulses of ~ 18 ns. In these measurements, the arrival time of the pump pulse is modulated and the derivative signal is measured with

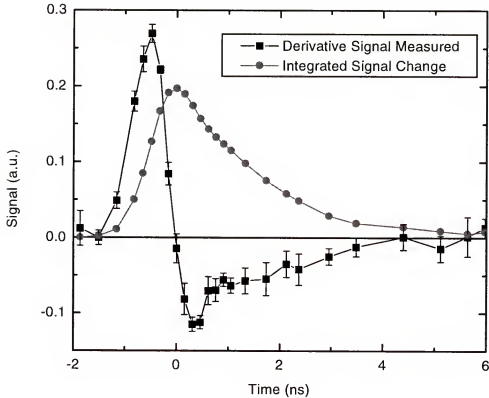


Figure 4.2: Plot of the measured derivative signal change with errors and the integrated photoinduced response for the MCT sample, measured at 100 K. The remainder of the plots of the decay at ZPD will show only the integrated response.

a lock-in amplifier (see Section 3.5.3). The signal is sampled for a time until the noise is acceptable, then the average delay is stepped to the next point and that point acquired. The derivative signal is then integrated to give the photoinduced change in transmission as a function of time. As an example of this, Figure 4.2 shows a plot of both the derivative and the integrated average photoresponse for the MCT sample at 100 K. The remaining ZPD data shown will contain only the integrated response.

4.2.3 Estimated Carrier Density

Given the laser power, spot size and repetition rate, a calculation can be made of the expected number of carriers generated by each pump pulse. The laser has a repetition rate of 53 MHz, with an output power of 300 mW at the sample when operated at 800 nm. This leads to approximately 3×10^{10} photons per laser pulse. The spot size at the sample is approximately 0.25 in. (0.64 cm) in diameter, slightly overfilling the aperture at the sample of 3/16 in. (0.48 cm) diameter. The film has an approximate thickness of 15 μm (see Section 4.2.1) and a uniform distribution of photogenerated carriers in the film is assumed. Taking reflectance losses at the surface into account, the carrier density immediately after the pulse is $\sim 3.5 \times 10^{13} \text{ cm}^{-3}$.

The synchrotron light itself can excite carriers. This would lead to a DC shift in the time dependent response of the sample as the synchrotron pulse is coincident with itself. This effect may be estimated by calculating the incident power on the sample above the bandgap of the MCT ($\sim 3000 \text{ cm}^{-1}$). For the lamellar grating instrument, the brass light pipe and thick polyethylene windows sharply reduce the intensity of the light above a few hundred wavenumbers, effectively eliminating the problem. For the mid IR measurements, the power below the cutoff of the KRS5 window ($18,000 \text{ cm}^{-1}$) and above the MCT gap is about 50 mW at an average beam current of 600 mA. This level is further reduced by the 70% transmission of the KRS5 window and nearly 50% transmission of the Ge:KBr beam splitter, leading to an estimate of 18 mW for synchrotron power available for carrier generation. This is slightly more than 5% of the laser power and is therefore almost negligible

in this experiment. Also note that all experiments involve derivative measurements and should not be sensitive to DC shifts of this nature.

Modeling the ZPD signal decay

The photoinduced signal is generated by a laser pulse with width of a few ps. The synchrotron pulse can vary in width from 300 ps to 1.5 ns, depending on the storage ring operational parameters. The nominal value in these experiments was 500 ps. The measured signal is the convolution of the exponential decay of the photocarriers and the relatively broad synchrotron pulse used to sample the transmission. For this analysis, the laser pulse is assumed to be a delta function. If the assumption is made that a single carrier is responsible for the photoinduced change in transmission, then the instantaneous change in transmission can be modeled as a single exponential decay or:

$$\Delta\mathcal{T}_{inst}(t) = \begin{cases} 0 & t < t_0 \\ Ae^{-\frac{t-t_0}{\tau_{lt}}} & t \geq t_0 \end{cases} \quad (4.1)$$

where A is a constant measuring the magnitude of the change, t_0 is the arrival time of the pump pulse, and τ_{lt} is the lifetime of the photogenerated carriers. The synchrotron pulse may be modeled as a gaussian pulse with width w . The measured response at the detector is a convolution of the probe pulse with the instantaneous photoresponse, written as:

$$\Delta\mathcal{T}(t) = \frac{1}{w\sqrt{\pi}} \int_{-\infty}^{\infty} \Delta\mathcal{T}_{inst}(t') e^{-\left(\frac{t-t'}{w}\right)^2} dt' \quad (4.2)$$

Without loss of generality the laser pulse may be taken to arrive at time $t' = 0$. The measured photoresponse may then be written as:

$$\Delta\mathcal{R}(t) = \frac{A}{w\sqrt{\pi}} \int_0^\infty e^{-\frac{t'}{\tau_{it}}} e^{-\left(\frac{t-t'}{w}\right)^2} dt'. \quad (4.3)$$

This has an analytical solution [40]:

$$\Delta\mathcal{R}(t) = \frac{Aa\sqrt{\pi}}{2} e^{-\frac{t}{\tau_{it}} + \frac{w^2}{4\tau^2}} \left[1 + \operatorname{erf} \left(\frac{t}{w} - \frac{w}{2\tau} \right) \right], \quad (4.4)$$

where $\operatorname{erf}()$ is the standard error function.

Figure 4.3 shows the integrated response for the ZPD decay measured at 100 K along with a fit based on Equation 4.4. The figure also contains a plot of the exponential decay of the photoresponse without the probe pulse convolution for comparison. Note that the maximum of the convolved photoresponse is approximately 65% of the maximum without convolution. This decrease is due to the lifetime of the carriers being similar to that of the probe pulse width. For carriers with lifetimes much larger than the pulse width, the two maxima would be nearly equal. For carriers with lifetimes shorter than the pulse width, the maximum measured change would be further reduced, and would scale proportionally to the lifetime. The response shape would approach that of the probe pulse.

The decay of the photoinduced signal at ZPD was measured at temperatures from 5 K to 150 K. The integrated responses and fits are shown in Figure 4.4. The fits are of the same form as Equation 4.4 and the fit parameters are given in Table 4.1. Fit magnitudes and lifetimes with error estimates are also plotted in Figure 4.5. The magnitude shows a decrease with increasing temperature. The

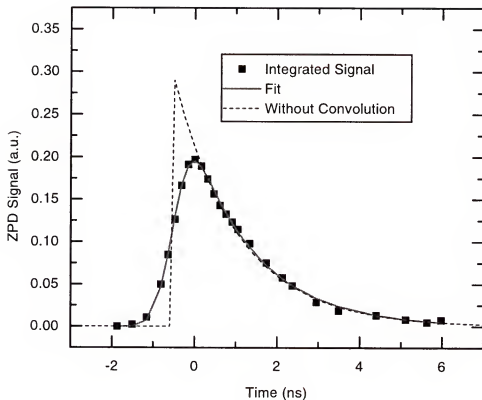


Figure 4.3: Plot of the integrated photoinduced response for the MCT sample, measured at 100 K with a fit based on Equation 4.4. Also plotted is the calculated instantaneous response, based on the fit parameters, without convolution of the pump pulse.

lifetime is fairly constant between 5 K and 100 K, but approximately doubles between 100 K and 150 K. The data is well described by a single exponential. This result is consistent with a single carrier type dominating the response with the other type being too slow to be measured. The data are assigned to the response of photogenerated electrons. The holes in MCT have a much higher mass and lower mobility [37] leading to a lower response and longer lifetimes.

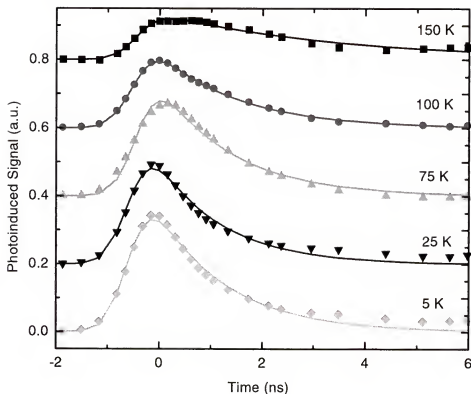


Figure 4.4: Plot of the the photoinduced signal at ZPD as a function of temperature for the MCT sample.

4.2.4 Time-resolved Spectroscopy

Far IR

Time resolved spectroscopy measurements were conducted on the sample using the lamellar grating and Bruker 113v spectrometers. A more thorough description of the experiment can be found in Section 3 of this dissertation. For the measurements using the lamellar grating, differential spectra taken by modulating the arrival time of the pump pulse were collected and then integrated. The

T (K)	A (a.u.)	τ_{lt} (ns)	w (ns)
5	0.52	1.38	0.48
25	0.45	1.28	0.48
75	0.43	1.43	0.48
100	0.29	1.58	0.48
150	0.15	3.58	0.48

Table 4.1: Fit parameters for the FIR ZPD signal decay measurements at temperature T . Fits are based on Equation 4.4. A is the magnitude, τ_{lt} is the lifetime and w is the probe pulse width.

Time (ns)	ω_p^2 (cm^{-1}) ²	γ (cm^{-1})
-0.99	50	17
-0.32	270	17
0.31	430	17
0.91	360	17
1.47	230	17
2.00	153	17
2.49	115	17
2.99	93	17

Table 4.2: Fit parameters for FIR time-resolved spectra of the MCT sample. All spectra can be fit using an oscillator with a scattering rate of 17 cm^{-1} .

integrated responses were then divided by the unexcited transmission to give the photoinduced absorption spectrum as a function of time.

Figure 4.6 shows time-resolved spectra for the FIR region of the MCT sample taken at 5 K. The data are well described with a Drude model using a single carrier, consistent with the interpretation of a single carrier being responsible for the observed change in transmission. Table 4.2 contains the fit parameters used for each of the delay times from this data. All of the data are fit to a single oscillator with a scattering rate of 17 cm^{-1} . This value is consistent with values for electrons

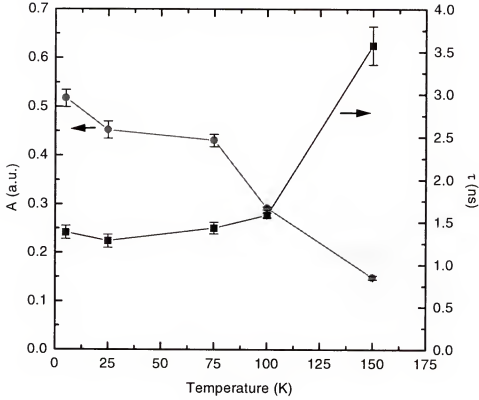


Figure 4.5: Plot of magnitude (A) and lifetime (τ) from fit parameters for ZPD decay measurements as a function of temperature. Fits use a convolution of an exponential decay and a gaussian probe pulse. All fits use the same probe pulse width of 480 ps.

in MCT and supports the interpretation of photogenerated electrons being the carriers responsible for the change in transmission. The oscillator strengths from the Drude fits are fit with a convoluted pulse with exponential decay as in the ZPD decay analysis. A plot of the oscillator strengths with the fit is shown in Figure 4.7. The magnitude of the fit represents the maximum oscillator strength and is proportional to the carrier density immediately after the pump pulse. The fit yields a maximum oscillator strength of 780 cm^{-2} . Assuming an effective mass

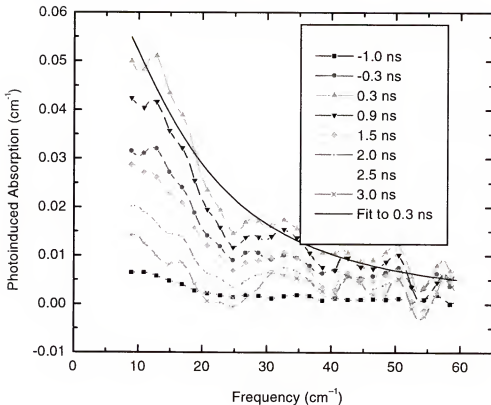


Figure 4.6: Time-resolved photoinduced spectra for the MCT sample in the FIR region.

$m^* = 0.07m_e$, the carrier density is $1.54 \times 10^{13} \text{ cm}^{-3}$, in reasonable agreement with the $3.5 \times 10^{13} \text{ cm}^{-3}$ predicted in Section 4.2.3. The lifetime from the fit is 1.37 ns, and is in excellent agreement with the ZPD decay data. The pulse width is ~ 700 ps. This value is somewhat larger than the ~ 500 ps from the ZPD decay data, but can be explained by differences in the storage ring operational parameters. The spectra were taken shortly after a fill at which time the bunch length nearer to 700 ps than the nominal 500 ps during the majority of a 7 bunch detuned fill. Thus, the spectral data are in good agreement with the ZPD decay in all cases.

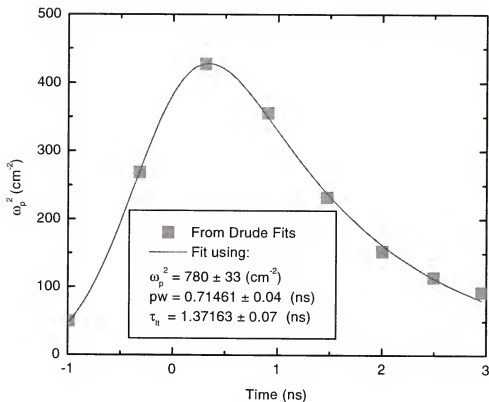


Figure 4.7: Plot of the oscillator strengths from the Drude fits to the spectral data. The line is a fit to the data of the form in Equation 4.4. Parameters from this fit are in good agreement with those from the ZPD decay measurements.

Mid IR

Mid IR time-resolved spectra were taken with the Bruker 113v (see Section 3.6.3). Laser insertion was accomplished by feeding an optical fiber through the cryostat and positioning it a few millimeters from the sample using a stainless steel guide tube (see Section 3.6.2). Laser power at the sample was similar to that in the FIR experiments. The illumination area was approximately half that in the lamellar experiments. The operational mode of the synchrotron was 7 bunch detuned, as with the experiments on the lamellar grating. With the Bruker, an interleaved se-

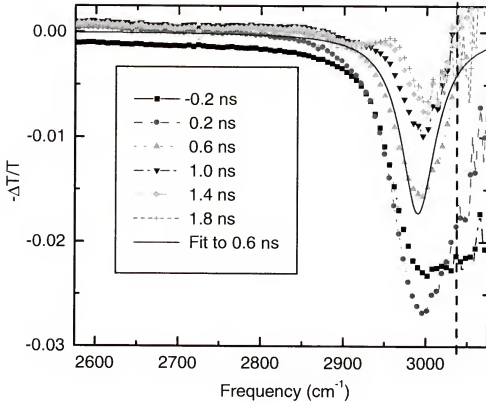


Figure 4.8: Time-resolved photoinduced spectra for the MCT sample in the mid IR region.

ries of spectra were taken with varying pump laser arrival times (see Section 3.6.3). These spectra were then separated according to their respective arrival times and the photoinduced change in transmission calculated using Equation 3.1.

The mid IR time-resolved spectra for the MCT sample are shown in Figure 4.8. These data are reasonably well described by a single oscillator whose parameters are given in Table 4.3. The maximum oscillator strength is roughly double that of the FIR experiments. The increase in oscillator strength is attributed to an increase in carrier density due to the higher laser intensity in the mid IR experiment. The

Time (ns)	ω_p^2 (cm^{-1}) ²	ω_0 (cm^{-1})	γ (cm^{-1})
-0.2	1270	3023	137
0.2	940	3002	90
0.6	340	2999	51
1.0	170	2997	44
1.8	110	2998	40
1.8	90	3001	44

Table 4.3: Fit parameters for the mid IR time-resolved spectra of the MCT sample.

data can not be fit by an exponential with similar parameters to those of the FIR spectral and ZPD measurements. This may be attributed to a lack of a sufficient number of data points near the initial rise in absorption. The oscillator width (scattering rate) begins quite high (over 100 cm^{-1}) and then decreases within a few hundred ps to a value near 40 cm^{-1} . This is interpreted as hot electron effects. The energy of the photons in the laser pump pulse is significantly greater than that of the gap ($12,500 \text{ cm}^{-1}$, compared to $3,000 \text{ cm}^{-1}$). This excess energy is converted into kinetic energy of the electrons, effectively raising their temperature. The fast electrons will occupy states higher in the conduction band than those in thermal equilibrium. The collision time of the conduction band electrons is ~ 2 ps based on the FIR data. This is consistent with a value of a few ps from other optical experiments [41]. Thus, a relaxation to thermal equilibrium within a few hundred ps is not unreasonable.

4.2.5 Sum Rule

The sum rule for oscillator strengths states that the total integral of the $-\Delta\mathcal{I}/\mathcal{I}$ curve is a constant. Figure 4.9 shows a plot of the integrated areas in the FIR

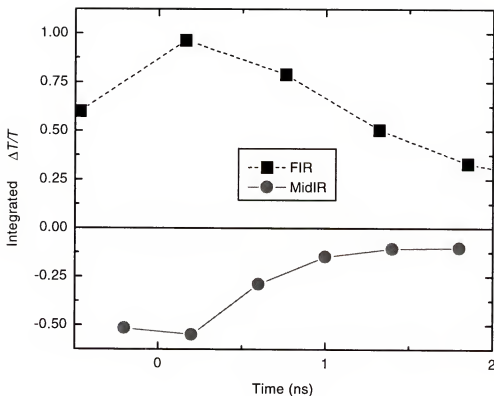


Figure 4.9: Integrated change in transmission for the FIR and mid IR regions. Oscillator strength at low frequency is taken from near the gap. The small difference in amplitude can be explained by a difference in pump intensity.

and mid IR regions as a function of delay time, corrected for the higher intensity of the mid IR experiment. It is evident that the additional spectral weight at low frequencies removed from the band gap edge. There is a discrepancy in the maximum integrated areas of the two regions. This is attributed to an imperfect measure of the intensities in each experiment. The mid IR data also shows a faster recombination than the FIR. This discrepancy and also that of the magnitude of the maximum oscillator strength may also be affected by a lack of data on the rising edge of the synchrotron pulse.

4.3 Summary

In this chapter we have described time-resolved measurements of a $\text{Hg}_x\text{Cd}_{1-x}\text{Te}$ film in the FIR and mid IR regions. Electron-hole recombination has been characterized with recombination rates on the order of 1.4 ns. The film showed photoinduced absorption in the FIR region with a Drude spectral response. Recombination lifetimes from both the spectroscopic and frequency averaged measurements were in good agreement. Furthermore, calculated electron densities from fits to the spectra are within a factor of 3 of the estimated electron density generated by each laser pulse.

Mid IR spectroscopic experiments were in qualitative agreement with those of the far infrared, showing the increased oscillator strength in the FIR region was removed from near the gap in the mid IR region. A lack of quantitative agreement was attributed to differences in experimental geometry and an insufficient number of data points for accurate integration of the response.

This experiment has demonstrated the capabilities of the U12IR beamline for use in measuring time-resolved spectra in the far and middle infrared regions. The pump-probe method was effective with both step scan and fast scan instruments, covering a range from 2 cm^{-1} to $8,000\text{ cm}^{-1}$ with a maximum time resolution of 500 ps.

CHAPTER 5 TIME-RESOLVED IR STUDIES OF Pb FILMS

5.1 Introduction

In this chapter time-resolved studies of superconducting lead and lead bismuth films are reported. The microscopic theory of superconductivity put forth by Bardeen, Cooper and Schrieffer (BCS) explains the superconducting state by means of a gap developing in the electronic band structure [42]. The gap occurs through a weak potential between the electrons mitigated by the electron phonon interaction. The superconducting state can be weakened or even destroyed by light, as first observed by Testardi [43]. Photons with energy greater than the gap can create quasiparticles at the expense of pairs, thus weakening the superconducting state. If the illumination is stopped, a non-equilibrium state exists until the quasiparticles recombine into pairs. This recombination usually involves transferring energy to the lattice through the interaction of electrons and phonons. As this is the interaction responsible for the pairing process, an understanding of the recombination is central to an understanding of superconductivity. Time-resolved spectroscopy of superconductors can be a useful tool for studying their fundamental properties.

5.2 Superconductivity

Superconductivity was first observed by Onnes in 1911 [44]¹. After its discovery, several decades passed before an explanation was developed. In 1957 Bardeen, Cooper and Schrieffer presented a very successful explanation [42]. The basic idea is that a weak attraction can bind the electrons into pairs. The attraction is caused by the interaction of electrons and lattice vibrations, or phonons. As one electron passes through the lattice, it causes a deformation, this deformation results in a slight increase in positive charge near that electron which creates a net attractive force on another electron. This causes a gap to develop in the band structure. BCS predicts at 0 K this gap is given by

$$2\Delta_0 = 3.54k_B T_c \quad (5.1)$$

where k_B is Boltzmann's constant and T_c is the superconducting transition temperature. At finite temperature near T_c the value of the gap can be approximated by

$$\frac{\Delta_g(T)}{\Delta_0} = 1.74 \left(1 - \frac{T}{T_c}\right)^{1/2} \quad T \approx T_c$$

The above formulas are valid for weak coupling between the electrons and phonons. For materials with strong coupling, T_c is reduced, and the gap is also reduced to a lesser degree. The result is that the factor in Equation 5.1 is larger than 3.54. The coupling strength also has effects on the electronic properties of superconductors [48, 49, 50, 51, 52, 53, 54]

¹For a general background on superconductivity consult references [45, 46, 47].

5.2.1 FIR Transmission of Thin Superconducting Films

Ordinary superconductors have a gap of $2\Delta_g$ in their electronic spectrum. Infrared spectroscopy was an important tool used by Glover, Tinkham and others in proving the existence of this gap [55, 56]. IR spectroscopy has also been useful in studying the gap [56, 57] and other properties of these materials [58, 59, 60, 61]. The BCS theory has proved very successful in quantitatively explaining the phenomena of superconductivity [42, 62, 48, 49]. BCS theory was first applied to the transmission of thin films by Mattis and Bardeen in 1957. Their calculations were for weakly coupled systems. Transmission measurements involving lead and other strongly coupled superconducting systems were shown to deviate from the Mattis-Bardeen predictions [59]. In 1968, Nam introduced a correction for strong coupling to the Mattis-Bardeen theory [48, 49]. This correction was shown to have good agreement with the experimental data [57]. Later, Ginsberg, Dynes and Harris published a first order correction for strong coupling that only takes the change in $\sigma_2(\omega)$ into account [63].

5.2.2 Non-equilibrium Superconductors

One of the marks of the robustness of BCS theory has been its success in predictions of non-equilibrium phenomena [64, 65, 66, 67, 68, 69, 70]. If pairs of electrons are broken, or unpaired electrons injected into a superconducting system, they appear as excited states called quasiparticles which eventually decay by phonon or some other emission and form Cooper pairs. Initial calculations of the recombination times of these quasiparticles were carried out by Schrieffer and Ginsberg and Rothworth and Cohen [66, 67]. These early results differed from

the experimentally determined lifetimes by an order of magnitude. It was shown by Rothworth and Taylor that the effective lifetime is enhanced by the emitted phonons breaking other pairs and thus generating more quasiparticles [71]. This ‘phonon trapping’ would result in a increase in the quasiparticle lifetime by about a factor of 5 for typical experimental geometries. They also predicted that in the limits of low reduced temperature (T/T_c) and a low density of excess quasiparticles compared to the density in thermal equilibrium, the temperature dependence of the lifetime goes as:

$$\tau \propto \left(\frac{1}{\Delta_g k_B T} \right)^{1/2} e^{\frac{\Delta_g}{k_B T}}, \quad (5.2)$$

where Δ_g is the single particle energy gap, T is the temperature and k_B is Boltzmann’s constant. Figure 5.1 shows a prediction for the quasiparticle lifetime as a function of temperature. It is based on calculations from [67] at 1.44 K corrected for phonon trapping and uses the temperature dependence of Equation 5.2. At 3.5 K, the estimated lifetime is ~ 100 ps. This is near the threshold of direct measurement with the 200–700 ps probe pulses available. By 2 K, the lifetime has increased to near 40 ps and should be easily resolved. However, for temperatures this low an immersion cryostat must be used. Such a system is undergoing commissioning at the time of this writing, but no experiments involving superconducting films have been conducted to date.

As first shown by Testardi [43], pairs may be broken by laser light and the change in the properties of the superconductor can not be explained simply by sample heating. In 1972, Owen and Scalapino published a theory which described a superconductor with a density of quasiparticles higher than that for thermal equilibrium [65]. Their relation for the energy gap of a nonequilibrium superconductor,

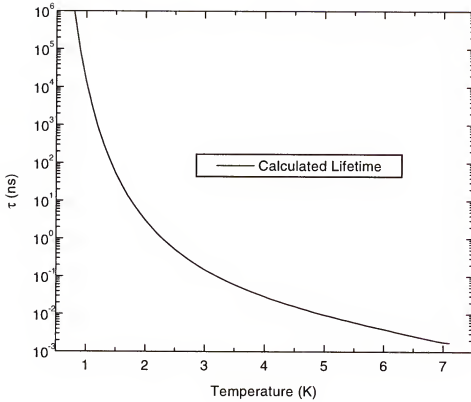


Figure 5.1: Estimated quasiparticle lifetime based on BCS [67, 71].

at low reduced temperature is:

$$\left(\frac{\Delta_g}{\Delta_0}\right)^3 = \left\{ \left[\left(\frac{\Delta_g}{\Delta_0}\right)^2 + n^2 \right]^{1/2} - n \right\}^2, \quad (5.3)$$

where n is the excess number density of quasiparticles in units of $N(0)\Delta_0$. $N(0)$ is the single spin density of states at $T = 0$. For small n Equation 5.3 may be approximated by [64]:

$$\frac{\Delta_g}{\Delta_0} \simeq 1 - 2n. \quad (5.4)$$

Calculations of the expected quasiparticle density indicate that for typical laser powers and film thicknesses used in the experiments described here, n should be near 0.01 at 4 K [72]. In order to be in the small perturbation limit, the number of excess quasiparticles n must be much less than the number of thermally available quasiparticles, n_{th} . For a temperature of 4 K, n is near $0.015n_{th}$, and thus within this limit. The number of thermally available quasiparticles decreases rapidly for lower temperatures. Thus for temperatures much lower, the small perturbation limit will no longer apply. Although not a significant concern in this thesis, exceeding the small perturbation limit will become increasingly important in future investigations at lower temperatures.

Photoinduced experiments have been conducted to study the nonequilibrium dynamics of several superconducting systems [73, 74, 64, 75]. Some direct time-resolved measurements were carried out; however, they had a time resolution of at best a few ns. The first time-resolved study with a resolution of 100 ps was performed by Johnson in a tunneling junction experiment [75]. However, this experiment was limited to temperatures near T_c . Also, the nature of the electrical response in the experiment was unclear and thus little information about the physics of the excited states could be extracted. The advent of coherent terahertz spectroscopy allowed a time resolved spectroscopy study with 1 ps time resolution [76]. This study showed the superconducting state could be destroyed in < 1 ps. However, the recombination of the quasiparticles was not investigated.

5.3 Experiment

In this experiment a synchrotron source is used perform time-resolved pump-probe spectroscopy on Pb and $\text{Pb}_{0.75}\text{Bi}_{0.25}$ thin films with resolutions of a few 100's of ps. The basic experimental apparatus is described in Chapter 3. These experiments used a lamellar grating interferometer with a He cooled bolometer as a detector. The samples were optically pumped using a mode-locked Ti:sapphire laser synchronized to the RF frequency of the ring.

5.3.1 Film Growth and Characterization

Thin films of lead and lead bismuth were grown in situ on a sapphire substrate in a He-tran cryostat used for the optical measurements. The substrate was clamped to the cold finger with indium foil gaskets to insure high thermal conductivity. The typical procedure followed was to pump the cryostat with a turbo mechanical pump for approximately one hour, until the pressure was below 1×10^{-6} torr. The substrate was then cooled to 4.7 K and a background spectrum taken. The substrate was then warmed to 100 K to boil off any nitrogen that may have condensed on the substrate. After that, the temperature was brought to 80 K and a film evaporated onto the substrate from a tungsten basket containing Pb or a $\text{Pb}_{0.75}\text{Bi}_{0.25}$ alloy. Based on previous experiments with a similar technique², typical film thicknesses were estimated to be approximately 100 angstroms for a film with a 10% transmission in the normal state³. Films were grown with trans-

²Personal communication from G.L. Carr.

³Films referred to in terms to in terms of a % transmission are always taken to mean the FIR normal state transmission at low temperature.

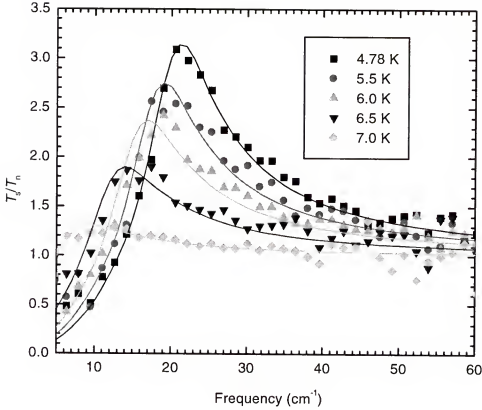


Figure 5.2: Plot of the measured $\mathcal{T}_s/\mathcal{T}_n$ as a function of temperature for a 10% transmission film. Symbols are data points, lines are fits using Mattis-Bardeen theory with a first order strong coupling correction [62, 49, 63].

mission ratios from 5% to 50% of the incident light. Film thicknesses were not measured as the films did not survive being warmed to room temperature.

Following deposition, the temperature was lowered to 20 K for a measurement in the normal state. Then the sample was cooled to approximately 4.7 K and spectrum was taken in the superconducting state. A ratio of the transmission in the superconducting state to that of the normal state was calculated. This allows a characterization of the quality of the film. Figure 5.2 shows the $\mathcal{T}_s/\mathcal{T}_n$ ratio for a 10% transmission film as a function of temperature. The lines are fits using

Mattis-Bardeen theory with a first order strong coupling correction [62, 63]. For a good film, the $\mathcal{T}_s/\mathcal{T}_n$ ratio should have a peak near 20–22 cm^{-1} and range from 2–3 at low temperature depending on film thickness. This is consistent with good film quality and BCS theory with strong coupling in the dirty limit. The fits typically yielded strong coupling factors near 0.17, somewhat lower than the value of 0.2 from the literature [63]. This may be due a difference in film quality and the use a of a finite scattering rate in our fitting method. If the film quality was good based on the $\mathcal{T}_s/\mathcal{T}_n$ ratio, time resolved measurements would begin.

5.3.2 ZPD Decay

In the initial time-resolved measurements, the lamellar grating was placed at zero path difference (ZPD) and the laser delay was dithered. Typical dither magnitudes were 200 - 600 ps. The average laser delay was then stepped through the decay of the photoinduced signal. This produces a measure of how the frequency averaged transmission changes over time (see Section 4.2.2). Figure 5.3 shows the measured differential signal as a function of laser delay for a Pb film at 3.9 K with a normal state transmission of approximately 30% and the pump pulse providing an average of 270 mW of power at the sample. The differential signal is integrated to give a frequency averaged $\Delta\mathcal{T}$ as a function of time. This is shown by the solid line in that same figure. Typically, accumulation of random errors in the derivative measurements led to the integrated signal over- or undershooting zero at the end of the 18.9 ns period between probe pulses, although, a few of the curves did return to very near zero.

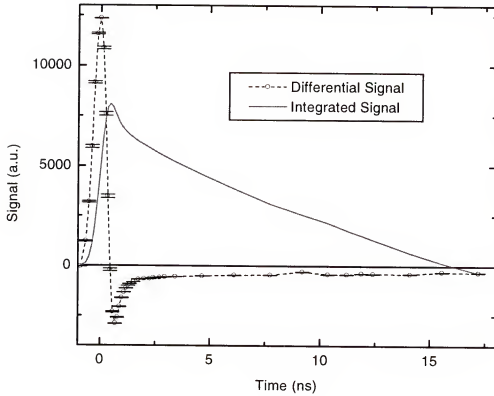


Figure 5.3: Plot of the measured differential signal and its integral for a lead film with 10% transmission in the normal state. Error bars are calculated from noise in the measurement. At delays above 16 ns, the integrated signal undershoots zero and goes negative. This is caused by accumulation of random errors in the derivative measurement.

Over 20 Pb and 3 $\text{Pb}_{0.75}\text{Bi}_{0.25}$ films were grown and characterized with varying thicknesses and film qualities. All of the films measured showed a two component decay. First there was a fast response which generally had a lifetime too short to be measured by the ~ 450 ps IR pulses available from the synchrotron. The second response was much slower and was too slow to be well characterized with the 18.9 ns between the pulses.

The data are fit based on a convolution of an exponential decay(s) and a gaussian probe pulse. See Section 4.2.3 for a more detailed discussion of the convolution. The slow response of the Pb and $\text{Pb}_{0.75}\text{Bi}_{0.25}$ films requires some additional considerations. Because the lifetime of the slow response is so long, following one pump pulse, the system does not have time to fully relax before the arrival of the next. This causes the measured changes in transmission to take place on top of an offset. To account for this, a constant is added to the magnitude of the slow portion of the decay, with the requirement that the part due to the slow portion of the decay be equal to that constant at the end of the 18.9 ns period between pulses. Thus, the fits take the form:

$$\Delta\mathcal{T}(t) = \frac{1}{w\sqrt{\pi}} \int_0^\infty \left[A_f e^{-\frac{t'}{\tau_f}} + (A_s + C) e^{-\frac{t'}{\tau_s}} \right] e^{-\left(\frac{t-t'}{w}\right)^2} dt', \quad (5.5)$$

where,

$$(A_s + C) e^{-\frac{18.9}{\tau_s}} = C. \quad (5.6)$$

Initial experiments varying the laser power showed the relative magnitude of the two responses changed as a function of incident laser power. Figure 5.4 shows the integrated signal change for a 30% transmitting Pb film at 3 different laser powers. The inset shows the signal change normalized by the laser power. The lines are fits to the data based on Equation 5.5. Fit parameters for all the Pb ZPD measurements can be found in Table 5.1.⁴ The fast response grows in proportion to the slow response as the incident power is reduced. Figure 5.5 shows the temperature dependent integrated response for a 10% transmitting Pb film.

⁴For consistency with the fits, all pulse widths quoted in the text will refer to gaussian half widths. The full- width-half-max (FWHM) is larger by a factor of ~ 1.6 .

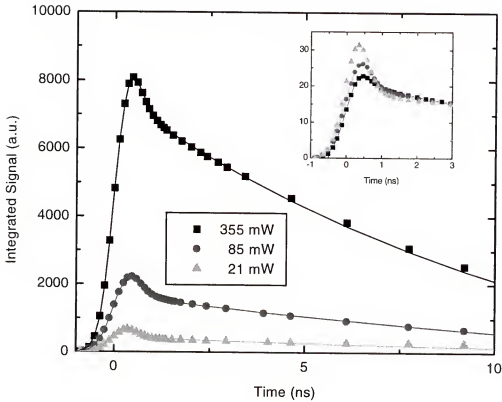


Figure 5.4: Integrated signal for a 30% transmission film as a function of laser power. The inset shows the curves normalized for by the laser power. Small variations in the slopes of the slow response are attributed to cumulative errors in the derivative measurements.

The fast response grows as the temperature is decreased, while the slow response remains fairly constant. The relative growth of the fast response with decreased laser power in Figure 5.4 can be explained as sample heating by the laser. As the power is decreased, the temperature of the sample is reduced. As the temperature of the sample decreases, the fast response grows relative to the slow one. The slow response is ascribed to sample heating. With the exception of incident power dependencies, for most measurements the laser power was kept to a minimum in order to reduce heating effects. The fits for the decays in Figure 5.5 showed a strong

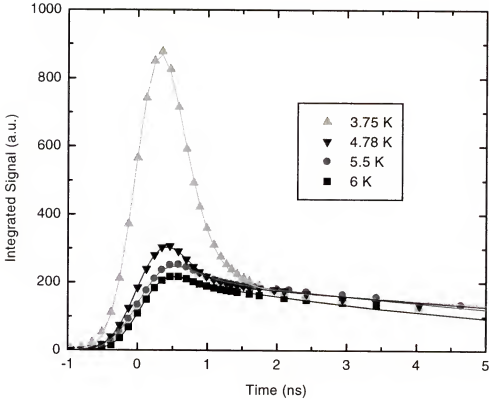


Figure 5.5: Integrated signal for a 10% transmission film as a function of temperature. The laser power at the sample was ~ 25 mW. The symbols are data points, the lines are fits of the form in Equation 5.5.

correlation between the fast response magnitude and lifetime. Except at the lowest temperatures, the measured data do not resolve the decay and are determined by the profile of the probe pulse. This result implies that the lifetimes are too short to be measured directly. To give some consistency to the fits, the magnitude of the fast response for high temperatures is set equal to that of the lowest temperature and the lifetime is allowed to vary. This fitting procedure assumes that the number of pairs broken is constant and the response of the system is temperature independent. These assumptions fail at higher temperatures, and this regime will

\mathcal{T}_{ns} (%)	P (mW)	T (K)	A_f (a.u.)	τ_f (ns)	A_s (a.u.)	τ_s (ns)	w (ns)
30	355	5	13100	0.146	7470	29	0.44
30	85	5	4870	0.187	1660	47	0.49
30	21	4.85	1380	0.185	432	40	0.40
10	20	3.85	2790	0.227	242	16	0.43
10	20	4.85	2790	0.049	210	38	0.45
10	20	5.55	2790	0.030	227	23	0.46
10	20	6.03	2790	0.025	217	14	0.41
35	20	3.95	2240	0.200	298	2.8	0.27

Table 5.1: Fit parameters for the FIR ZPD signal decay measurements for Pb films. Fits are based on Equation 5.5. Films are listed by normal state transmission and laser power. Parameters are: magnitude of the fast response, lifetime of the fast response, magnitude of the slow response, lifetime of the slow response and pulse width.

be discussed later. Because the incident pump laser causes sample heating and the temperature sensor is not mounted directly on the sample, differences between the measured and actual temperatures must be accounted for. In the superconducting state, the absolute transmission of the film is dependent on the temperature. Thus, it can be used as a kind of thermometer to measure the increase in temperature due to the laser. Most measurements were performed with about 20 mW of laser power at the sample. For a 30% transmission film, this caused a 0.1 K increase at 4.5 K. The increase will vary with temperature depending on the heat capacity of the film and the thermal conductance of the film and film/substrate interface. For the temperature range used in these experiments, the specific heat of the film is dominated by the lattice and varies as T^3 [28]. The thermal conductivity of the film is proportional to the heat capacity and also varies as T^3 [28]. At low temperatures, acoustic mismatch theory indicates the conductance at the film/substrate interface will also vary as T^3 . If the laser power is held constant, the temperature

change in the film will be proportional to $1/T^3$. Film thickness will have some effect because of the greater heat capacity of the thicker film. This is partially offset by the increased absorption of the thicker film.

One may presume that the slow response should vary with temperature due to the variations in the specific heat and thermal conductance. The temperature change is proportional to $1/T^3$ as mentioned above. However, as the temperature decreases, the transmission increases with the opening of the gap. The increase in transmission is dependent on the source spectrum, detector efficiency and other instrument parameters and is not easily calculated. However, it can be measured and the result shows that the increase in the change in temperature is almost completely compensated by the decrease in the rate change of transmission with temperature. Figure 5.6 is a plot of the measured frequency averaged transmission as a function of temperature for a 20% transmission $\text{Pb}_{0.75}\text{Bi}_{0.25}$ film, taken with the grating at ZPD. Lead bismuth data are shown because similar data for lead was taken only above 4.8 K. The limited lead data is comparable to the lead bismuth if adjusted for differences in T_c . The inset shows the derivative with respect to temperature and T^3 curve for comparison. The close adherence of the derivative to T^3 explains the nearly constant magnitude of the thermal portion of the response with changing temperature.

5.3.3 Temperature Dependence of the Quasiparticle Lifetime

In all measurements conducted during detuned operations the quasiparticle lifetime was too short to be measured by the ~ 450 ps probe pulses. A 30% transmission film was measured with a compressed bunch synchrotron lattice yielding

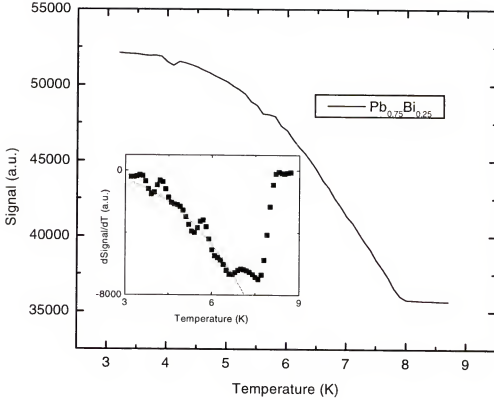


Figure 5.6: Frequency averaged transmission as a function of temperature for a $\text{Pb}_{0.75}\text{Bi}_{0.25}$ film. The symbols in the inset show the derivative with respect to temperature. The solid line in the inset is a T^3 curve. The close adherence of the derivative to T^3 explains the nearly constant magnitude of the thermal response in the ZPD measurements.

probe pulses on the order of 270 ps (see Figure 5.7). Based on a fit to the integrated signal of the form in Equation 5.5, this measurement indicated a quasiparticle lifetime of ~ 200 ps at 3.95 K.

Even with the shortest bunches currently available, for temperatures above 4 K the quasiparticle lifetime is too short to be measured directly. However, it is still possible to measure the temperature dependence of lifetime. Recall that the height of the peak due to the fast portion of the signal in the ZPD measurements was

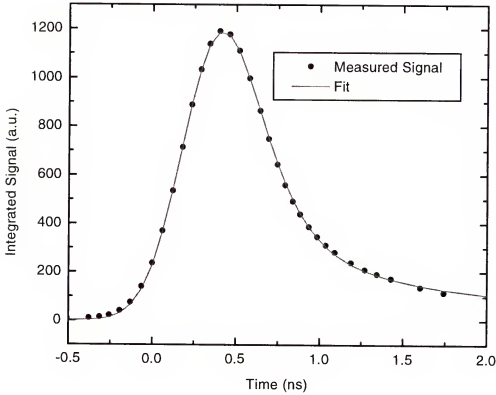


Figure 5.7: Integrated signal for a 35% transmission film at 3.95 K. The laser power at the sample was ~ 20 mW. The symbols are data points, the line is a fit of the form in Equation 5.5. The fit indicates a quasiparticle lifetime of ~ 200 ps.

reduced at higher temperatures. This was attributed to a reduction in lifetime. A measurement with a large dither amplitude that makes the full step up⁵ measures this the peak height with an offset due to the thermal portion of the decay. If the thermal portion is subtracted, the remaining part should be due to recombination of nonequilibrium quasiparticles.

⁵The “step up” means a dither sampling between before the arrival of the probe pulse and at the peak of the response. The “step down” means a dither sampling between the peak response and after the fast response has decayed leaving only the thermal portion. See the inset of Figure 5.11 for an example.

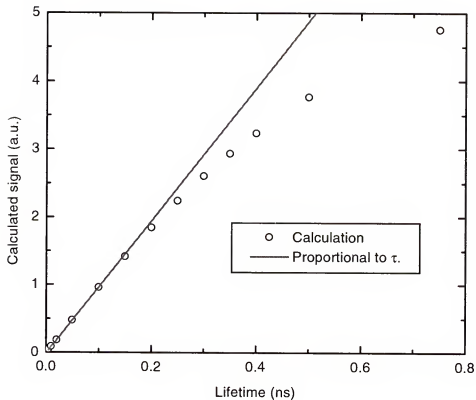


Figure 5.8: Calculated signal as a function of lifetime for a 1 ns probe pulse and exponential decay with constant initial number of quasiparticles. The calculation is based on Equation 5.5. The points are from the calculations and the solid line is what the signal would follow if it were proportional to the lifetime. The two differ by $\sim 10\%$ for a 0.3 ns lifetime.

The measured signal will be a convolution of the probe pulse and the time dependent change in transmission. For quasiparticle lifetimes much shorter than the pulse width, the signal is proportional to the lifetime. Figure 5.8 shows a plot of the calculated signal for a 1 ns probe pulse as a function of quasiparticle lifetime, based on Equation 5.5. If we take 10% to be our maximum acceptable error, then the measured signal should be acceptable up to a lifetime of 0.3 times the pulse width. The measured lifetime for Pb was 220 ps at a temperature of 3.8 K. The

measured decay curve was taken at high beam current just after a fill and should have a corresponding pulse width of 700 ps. Thus, the measured curve should be proportional to the lifetime within acceptable limits for temperatures of 3.8 K and higher, assuming a temperature dependent lifetime of the form of Equation 5.2.

The measured maximum change in transmission signal is related to the lifetime through shifts in the gap, Δ_g . This relationship is temperature dependent and may be written as:

$$\Delta \text{Signal}(T) = \frac{d\text{Signal}}{d\Delta_g}(T) \Delta \Delta_g. \quad (5.7)$$

The relationship between the signal and gap is a complicated function dependent on material properties, detector sensitivity, source spectrum and the transmission spectrum of the instrument. In general, this function is difficult to calculate near the gap. However, the signal and gap can be related through the change in signal as a function of temperature using BCS to calculate the gap as a function of temperature. The transmission signal as a function of temperature is directly measurable. Thus, the change in signal due to a change in gap may be written as:

$$\frac{d\text{Signal}}{d\Delta_g}(T) = \frac{d\text{Signal}(T)}{dT} \cdot \frac{1}{\frac{d\Delta_g(T)}{dT}}. \quad (5.8)$$

The change in gap, $\Delta \Delta_g$ in Equation 5.8 is dependent on the number of excess quasiparticles generated by the pump pulse, and this dependence is itself temperature dependent. The entire relation between the change in transmission and the number of excess quasiparticles can be written as:

$$\Delta \text{Signal} = \frac{d\text{Signal}}{dT} \cdot \frac{1}{\frac{d\Delta_g}{dT}} \cdot \frac{d\Delta_g}{dn} \cdot \Delta n. \quad (5.9)$$

In order to fit the data, several assumptions were made to simplify the analysis. $d\text{Signal}/dT$ was calculated from a measured curve of the transmitted signal as a function of temperature over most of the range. At low temperatures the measured curve flattens out and small errors in the measurement lead to large errors in the derivative. To compensate for this, an estimated derivative is calculated from BCS theory with the same code used for fitting the $\mathcal{I}_s/\mathcal{I}_n$ ratios and an assumed instrument spectrum is used for the derivative below 4.5 K. The $d\Delta_g/dT$ term is calculated from BCS theory.

From Owen and Scalapino [65], the third term is constant and proportional to n at low temperatures and in the limit of small n . For this analysis it is taken to be independent of temperature. The last term on the right hand side of Equation 5.9 is also temperature dependent. The incident photons break pairs generating energetic quasiparticles. These quasiparticles release their energy through collisions and interactions with phonons. The energetic particles from the collision and phonons with energy above the gap go on to create more pairs until an equilibrium is reached and most of the excess quasiparticles have energies just above the gap. The total number of pairs created should be inversely proportional to the gap so $\Delta n \propto 1/\Delta_g$. The individual corrections and the total combined effect are shown in Figure 5.9. Each has been scaled to 1 at 3.5 K.

Figure 5.10 shows the quasiparticle lifetime as a function of temperature. The open circles represent data points after making the corrections of Equation 5.9 and scaling to the lifetime determined by the lowest temperature ZPD measurements. The solid circles are data points from the ZPD measurements. The line is a fit based on Equation 5.2. The only adjustable parameter of the fit is the magni-

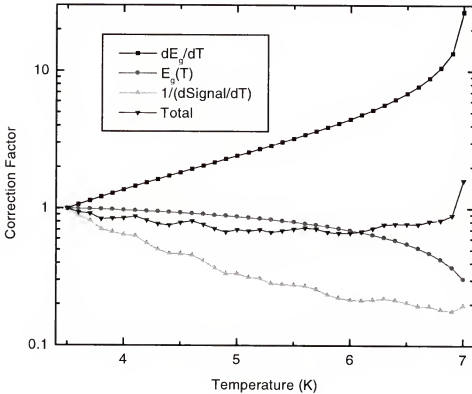


Figure 5.9: Corrections to the maximum dither signal to yield the quasiparticle lifetime as a function of temperature.

tude. All other parameters used are the the same as those for the $\mathcal{I}_s/\mathcal{I}_n$ fits for the same film. The inset shows the dither signal as measured. The data are in reasonably good agreement with theory over the entire temperature range, somewhat surprising considering the assumption of low reduced temperature for some of the corrections. The agreement with Equation 5.2 is consistent with previously published data [71, 64].

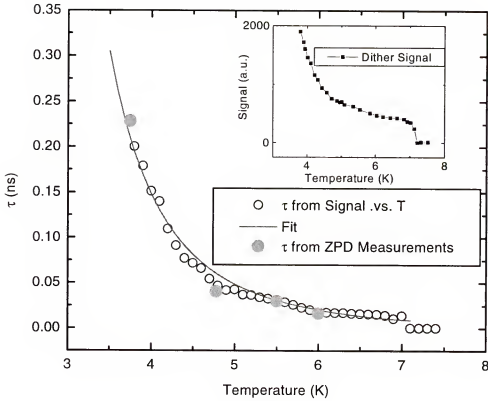


Figure 5.10: Quasiparticle lifetimes. The solid circles are based on ZPD measurements. The open circles are based on temperature dependent measurements of the maximum dither signal (shown in inset) with corrections (Figure 5.9) and scaled to the ZPD measurements at the lowest temperature. The line is a fit based on Equation 5.5.

5.3.4 Time-resolved Spectroscopy

Time-resolved photoinduced spectra were taken for many of the films grown. For high laser powers, the response is dominated by sample heating (see Figure 5.4) and thus the spectra are not interesting in discussions of non-equilibrium phenomena. For low laser powers, the slope of the slow response was too small to yield meaningful spectra in a reasonable amount of time. However, the changes in the spectra at the rapid step up and down of the fast response at low temperatures

are measurable and interesting. The step up spectra is a combination of both sample heating and the gap shift caused by excess quasiparticles. The step down is largely due to recombination of excess quasiparticles as the changes due to the slow thermal response are small over such a short period. Summing the two spectra gives a result after most of the excess quasiparticles have recombined into pairs and is largely due to sample heating. Figure 5.11 shows the time-resolved spectra taken from a 10% transmission film with a laser power of 20 mW at the sample. The spectra were measured with a dither amplitude of approximately 730 ps, large enough to make the entire step up and step down of the fast response. The top panel shows the two measured spectra their sum. The inset shows the points between which the spectra were taken on a ZPD measurement. The middle and lower panels show fits to the sum and step down, corresponding to the thermal and fast response respectively. Dashed lines between the data points are guides to the eye, solid lines are fits based on the same algorithm used in calculating the $\mathcal{T}_s/\mathcal{T}_n$ ratios and use the same film parameters. The thermal response is fit with a temperature shift of 0.025 K and the fit is in good agreement with the data over the frequencies measured. The fast response is fit with a gap shift of 0.06 cm^{-1} . The fit is reasonable in magnitude but does not have good agreement over any significant frequency range. Deviations at low frequencies are attributed to decreasing signal-to-noise below 20 cm^{-1} . Deviations at higher frequencies may be due to strong coupling effects not considered in the first order correction used, or improper consideration of the change in gap due to excess quasiparticles [65].

The differential spectra may be used to perform consistency checks on our other data. Although the data are somewhat noisy, they can provide order of

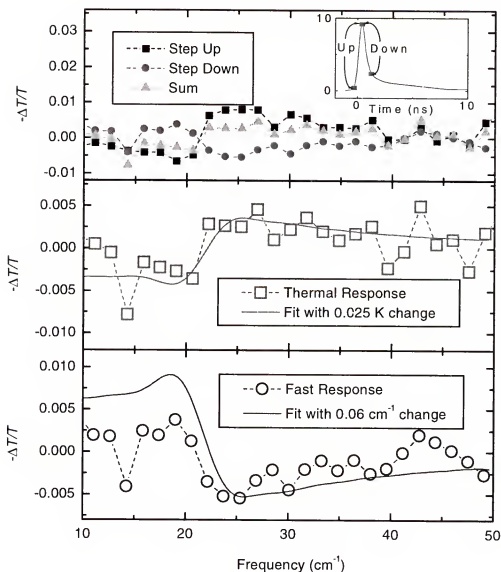


Figure 5.11: Differential spectra for a 10% transmission Pb film. The top frame shows the two measured differential spectra and their sum. The inset shows points on the response between which the spectra were taken. The step down is almost fully comprised of the fast response. The sum of the two reflects a good estimate of the thermal component of the decay. The center and lower frames contain these two spectra with fits based on a gap shift for the fast decay and a temperature shift for the slow decay. Fits based on the same algorithm used for calculating the T_s/T_n ratios.

magnitude estimates for the thermal lifetime and excess quasiparticle density. The fast response fit gave a gap shift of 0.06 cm^{-1} . The measured response is the real response convolved with the probe pulse. This leads to the true gap shift shortly after the pump pulse being approximately 3 times larger than the measured value, assuming the measured 220 ps lifetime. Thus, the maximum gap shift should be $\sim 0.18 \text{ cm}^{-1}$. From Equation 5.4, this is consistent with an excess quasiparticle density $n = 0.004$. This is somewhat smaller, but of the same order as the predicted value of 0.01. The temperature change from the thermal fit may be used with the temperature rise from the frequency averaged change in transmission to determine a lifetime for the thermal part of the decay. If the assumptions that the thermal decay is a single exponential and the differential signal is proportional to the temperature change for small changes, then the ratio of the change from the differential spectra and the average temperature increase give a slow decay time of 70 ns. This is larger than the measured values by a factor of 2 to 5, but also of the same order. The differences are not surprising considering the poor sensitivity to lifetimes of the same order or larger than the 18.9 ns period between pulses.

5.3.5 $\text{Pb}_{0.75}\text{Bi}_{0.25}$

Only 3 $\text{Pb}_{0.75}\text{Bi}_{0.25}$ films have been grown and measured at this time. The lead-bismuth alloy data is much less complete than that of the lead and will not be discussed in detail here. However, one experiment is worthy of note at this time. The maximum time resolution achieved to date by this beamline came with a lead- bismuth measurement. Figure 5.12 shows the ZPD decay of a 20% transmission $\text{Pb}_{0.75}\text{Bi}_{0.25}$ film. The solid line is a fit based on Equation 5.5 and

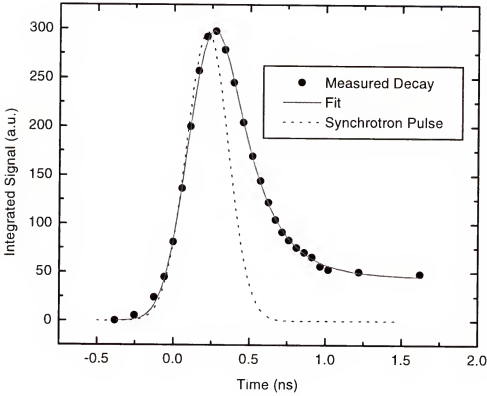


Figure 5.12: Integrated signal for a 20% transmission $\text{Pb}_{0.75}\text{Bi}_{0.25}$ film at 3.5 K. The laser power at the sample was ~ 20 mW. The symbols are data points, the solid line is a fit of the form in Equation 5.5. The dotted line shows the synchrotron pulse. This measurement reflects the maximum time resolution so far achieved at the U12IR beamline.

the dotted line shows the width of the synchrotron pulse for comparison. The fit parameters are given in Table 5.2. The probe pulses had a width of ~ 190 ps. The quasiparticle lifetime for the lead bismuth film was measured to be 200 ps at 3.5 K. The bunch compressed lattice used in this experiment produced pulses with widths approximately half those achieved in detuned operations. However, this comes at the cost of beam current. The bunch compressed lattice is limited to below 100 mA, about 25% of the average current in detuned operations. The

\mathcal{T}_{ns} (%)	P (mW)	T (K)	A_f (a.u.)	τ_f (ns)	A_s (a.u.)	τ_s (ns)	pw (ns)
20	20	3.5	647	0.20	49	1.4	0.19

Table 5.2: Fit parameters for the FIR ZPD signal decay measurements for the $\text{Pb}_{0.75}\text{Bi}_{0.25}$ film. Fits are based on Equation 5.5. Parameters are: normal state transmission, incident laser power, magnitude of the fast response, lifetime of the fast response, magnitude of the slow response, lifetime of the slow response and pulse width.

short thermal lifetime of the fit is attributed to having data over only 2 ns of the decay.

5.4 Summary

In this chapter we have reported time-resolved infrared studies of superconducting Pb and $\text{Pb}_{0.75}\text{Bi}_{0.25}$ films with time resolutions up to 200 ps. Several techniques were applied to measure the far infrared change in transmission. The frequency averaged change in transmission showed a two component decay, similar to that reported in transient the electrical response of Nb [75]. The fast component of the decay was ascribed to recombination of excess quasiparticles, the slow response was ascribed to sample heating.

Fits to the frequency averaged data allowed direct measurement of the quasiparticle lifetime at low temperatures. The temperature dependence of the lifetime has been inferred from measurements of the maximum signal as a function of temperature. The lifetimes and temperature dependence are in agreement with previously reported values and theoretical predictions. The thermal response was constant over the temperature range measured. This was due to the increase in

sample heating being offset by a decrease in sensitivity of the change in transmission to temperature. Fits to the spectroscopic data allowed an estimate of the energy gap shift and hence the number of pairs broken. This estimate was in reasonable agreement with the expected number of pairs broken based on the amount of energy absorbed by the film.

CHAPTER 6 CONCLUSION

This dissertation has presented a description of a new facility for time-resolved measurements in the infrared region. The U12IR beamline of the National Synchrotron Light Source at Brookhaven National Lab is a dedicated infrared beamline optimized for use in far infrared and time-resolved studies. Using the synchrotron as an IR source and a mode-locked Ti:sapphire laser as an excitation source, time-resolved pump-probe spectroscopy may be performed.

The broadband nature of the synchrotron spectrum allows the use of well developed interferometric techniques. Differences between interferometers and monochromators were discussed, including the multiplex advantage enjoyed by interferometers. A comparison was made between amplitude and wavefront dividing interferometers. The wavefront dividing lamellar grating type was shown to be more efficient at the lowest frequencies (below 50 cm^{-1}), while an amplitude division type is the better instrument for higher frequencies (above 50 cm^{-1}). The implications of a pulsed IR source on the maximum frequency resolution attainable were investigated. It was shown that the current instruments may be limited by the short probe pulse, but the experiments described in this dissertation are not at a sufficient resolution to be affected by this limitation.

Characteristics of the infrared spectrum from the synchrotron were developed and discussed. The current interferometer end stations allow a frequency range of $2\text{--}10,000\text{ cm}^{-1}$. The synchrotron source has been shown to have several advan-

tages over a blackbody source, despite its lower output power over most of the IR region. The synchrotron's higher brightness allows greater throughput and higher signal to noise for small samples and surface studies. For frequencies below 20 cm^{-1} the synchrotron has a greater output power than a typical thermal source. The pulsed nature of the synchrotron radiation allows time-resolved pump-probe measurements. The VUV ring provides IR pulses on the order of 1 ns during normal operations, with a period between pulses of 18.9 ns. Special operations allow pulse widths as low as 200 ps to be achieved. The maximum period between pulses is 180 ns. This allows transient phenomena with time scales from 100s of ps to 100s of ns to be investigated.

A detailed description of the experimental apparatus was presented, including extraction and steering optics for bringing the synchrotron light to the spectrometers, as well as optics for bringing the laser pump pulses to the samples. Methods for adjusting and maintaining the the arrival time of the laser pump pulse with respect to the synchrotron probe pulse were discussed. Several techniques were developed for time-resolved measurements. These included both frequency averaged and frequency dependent measurements using rapid scan and step scan interferometers.

The data presented in the experiments described in this work have demonstrated some of the capabilities of the new facility. The time-resolved spectra showed evidence for only one carrier being responsible for the changes in absorption. The measured lifetime was much shorter than that observed in clean samples. This difference was attributed increased scattering from surface defects. Measurements over a broad spectral range showed oscillator strength gained in the FIR

region was removed from near the semiconductor energy gap. The changes in absorption deviated from the sum-rule for oscillator strengths. This deviation may be explained by a lack of sensitivity to frequencies much above the gap.

The investigations of quasiparticle recombination in Pb and $\text{Pb}_{0.75}\text{Bi}_{0.25}$ films resulted in the direct measurement of the quasiparticle lifetime and its temperature dependence. The time-resolved frequency averaged response showed a two component decay similar to that reported in transient electrical measurements of Nb films [75]. The fast response varied strongly with temperature and was ascribed to the recombination of excess quasiparticles. The slow response was nearly constant over the range of temperatures measured and was ascribed to sample heating. The lifetimes and temperature dependence extracted were in agreement with previously published studies and theoretical calculations. The maximum time resolution to date was achieved with probe pulse widths ~ 200 ps. Time-resolved spectra indicated the number of quasiparticles generated was of the same order as that expected based on estimates of the amount of pump energy absorbed. The spectra were also used to estimate the lifetime of the slower thermal decay. The result was consistent with the values derived from the frequency averaged measurements within experimental uncertainty.

In sum, the U12IR beamline has proved to be a useful tool for sample characterization and the investigation of some of the fundamental phenomena of solid-state physics. The broad frequency and time scale ranges allow the study of a host of systems. Current experiments are limited to temperatures above 3 K and sample heating by the laser has proved to be a concern in some instances. The addition of an immersion cryostat currently undergoing commissioning will allow lower tem-

peratures and higher fluence and at the same time reduce effects due to sample heating.

APPENDIX A COHERENT EMISSION

A.1 Introduction

The expressions for the intensity of synchrotron radiation derived in Chapter 2 assume the individual particles in the beam emit incoherently. For wavelengths on the order of the bunch length, there is an increase in the emitted power caused by the coherent superposition of radiation from the electrons in the bunch [77, 78, 25, 79]. Equation 2.37 (see Section 2.4.6) gives the theoretical frequency at which the energy from coherent emission equals that of normal incoherent emission for a given current and bunch geometry. Using this expression, coherent emission should not be measurable, even at the lowest frequency measurable with the lamellar grating spectrometer and the maximum current in single bunch mode of 300 mA. However, bursts of coherent emission have been observed at the U12IR beamline of the National Synchrotron Light Source (NSLS), beginning at currents much below the maximum. Similar phenomena have been reported at SURF II (NIST) [80]. This appendix will give a brief discussion of the coherent emission observed at the NSLS, including some characteristics and possible explanations.

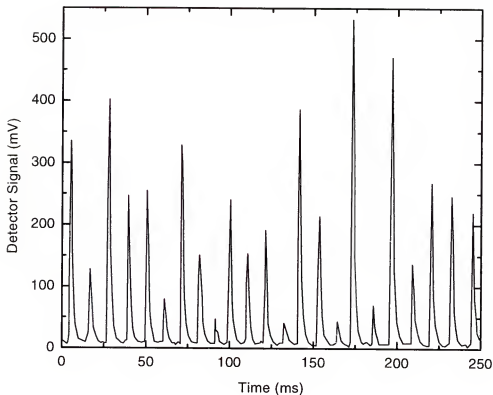


Figure A.1: Bursts of coherent emission. The fall time is limited by the detector response of $200\ \mu\text{s}$. Time between bursts averaged between 1 and 10 ms, depending on the operational parameters.

A.2 Observations

The bursts of coherent emission were first observed during single bunch detuned operations intended for timing studies. Figure A.1 shows a plot of the bursts as measured with a bolometer detector. The bursts decay faster than the $200\ \mu\text{s}$ fall time of the bolometer used. The bursts begin to appear once the ring current, I , reaches a threshold value, I_{th} , which is dependent on the ring operating parameters. Below the threshold, the average intensity of the emission is linear with the beam current, as expected for incoherent emission by the electrons in the bunch. Above

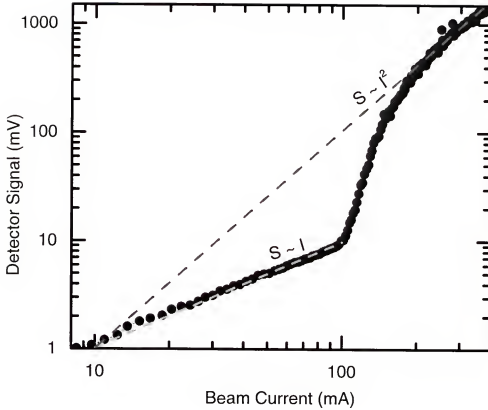


Figure A.2: Average detector signal as a function of current in single bunch mode. Below 100 mA, the signal is proportional to the beam current, above the 100 mA threshold, the signal becomes dominated by the coherent emission and varies with the square of the beam current above threshold ($[I - I_{th}]^2$).

the threshold, the excess intensity (that above the linear part) increases with the square of the current over threshold, $(I - I_{th})^2$. Figure A.2 shows a plot of the average signal as a function of beam current. The threshold was found to be fairly constant dependent on the current per bunch for standard detuned operations. For detuned single bunch mode, the threshold current was about 100 mA. In detuned, 3 bunch symmetric operations, the threshold current was found to be near 300 mA. Small deviations consistent with the onset of coherent emission were observed

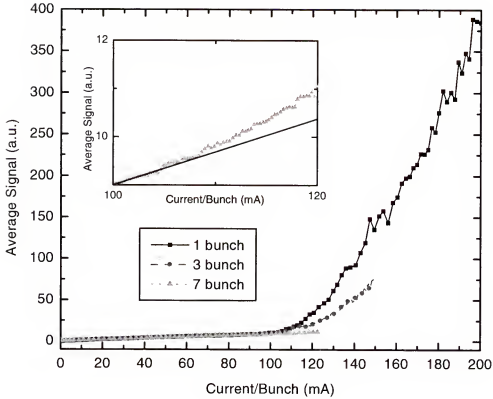


Figure A.3: Average detector signal as a function of current per bunch for 3 different modes of operation, single bunch, 3 bunch and seven bunch. The inset is an expanded view of the 7 bunch signal near the maximum and shows some initial deviation from a linear variation of the signal with current, indicating the onset of coherent emission.

in 7 bunch detuned operations as well, although at slightly more than 100 mA per bunch. See Figure A.3.

Spectra of the emission were taken. As mentioned in Chapter 3, the lamellar grating spectrometer has a strong oscillations in spectra taken at low frequencies caused by the cone upstream of the diamond window separating the spectrometer vacuum space from that of the ring. To remove this structure due to the instrument response, spectra were taken with both incoherent and coherent emission and

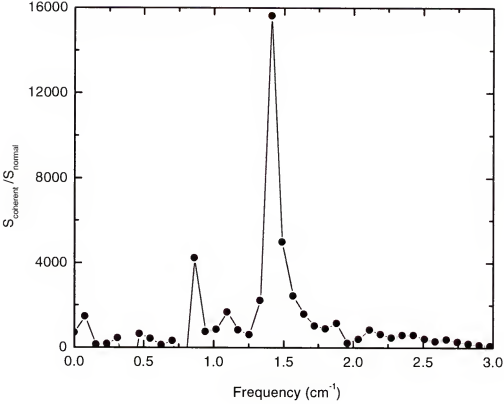


Figure A.4: Coherent emission spectrum. The plotted spectrum is normalized by the incoherent spectrum to remove oscillations from the instrument response.

ratioed. Figure A.4 shows the coherent emission spectrum normalized by that of the incoherent emission. There is a strong peak near 1.4 cm^{-1} ($\sim 7 \text{ mm}$ wavelength). In single bunch detuned operations, the bunches are known to have a length of $\sim 30 \text{ cm}$. The peak in the spectrum is consistent with structure on the scale of 7 mm , more than an order of magnitude shorter than the bunch length. This structure is thought to be micro-bunching (density modulations within the bunch), which is a characteristic of the microwave instability [81, 79, 82].

The microwave instability is caused electrons interacting through their wake fields. The wake field is characterized by a complex impedance determined by the beam pipe, RF cavities and other structures in the ring [81, 82]. Some of the bellows used in the ring have a corrugation spacing of 7 mm and may be responsible for the instability that causes the emission.

The range of time between bursts varies between 1 and 10 ms. The bursts of coherent emission decay faster than the $\sim 200 \mu\text{s}$ fall time of the detector used. The rise time of the bursts was typically faster than that of the detector rise time of 1–2 μs . At present, what determines the rise and fall times and time between bursts is not known. Further studies are needed to understand better the relationship between the various ring parameters and the coherent emission. A more detailed discussion of the observed coherent emission as well as the microwave instability and how operational parameters may affect the instability may be found in the literature [81, 82].

A.3 Summary

Bursts of coherent emission were observed on the NSLS VUV ring. The bursts had a frequency of 1.4 cm^{-1} with rise and fall times lower than the limiting values of the detector used in the measurements. The time between bursts varied from 1 to 10 ms. The emission begins only after the beam current has exceeded a threshold value. The coherent part of the emission is proportional to the square of the current above that threshold. The bursts are attributed to density modulations caused by the microwave instability. It is noted that several bellows around the

ring have a 7 mm corrugation spacing and may be the source of the impedance modulations that lead to the instability.

APPENDIX B USING A BOLOMETER AS A MID IR DETECTOR

B.1 Introduction

This appendix describes experiments for using a bolometer detector at mid infrared frequencies. High brightness is one of the large advantages of using synchrotron radiation as a light source [3, 2]. Usually, this feature is put to use in microscopy, or surface science where the samples measured are small or have small etendue [7, 8]. The high brightness allows an improved signal-to-noise ratio over thermal sources by allowing more light to be focused into the small area of the sample being measured. The high brightness may also be used at the detector to improve signal-to-noise. Bolometric detectors measure changes in voltage across an element with a large change in resistivity with respect to temperature. The absorbed light warms the element slightly causing the resistance across it to drop. The background noise of this type of detector is limited by the amount of thermal background radiation it sees [83, 84]. Detectors are shielded against stray light from most directions allowing in the light to be measured also allows the thermal background of the optics transporting the light from the source. To reduce the background, cold filters are placed in front of the detector, or in front of a light cone which focuses the incident light onto the detector. These filters are kept at liquid helium temperatures to reduce their emission and are fabricated to only allow the spectral region of interest to pass through, greatly reducing the thermal

background by rejecting all light outside the frequency range of the filter. This experiment involves replacing the optical frequency filter with a spatial filter in order to reduce the background and still pass higher frequencies of source radiation.

B.2 Experiment

The detector used in these experiments was an Infrared Laboratories bolometer with a boron-doped silicon element. This detector has a filter wheel kept at liquid helium temperatures with 4 positions for selectable filtering. Usually, these filters are made of either black polyethylene or polyethylene with a diamond or garnet scatter powder. One of these cold filters was replaced by a brass disk with a 1 mm diameter pinhole. The detector comes with a polyethylene window which is not transparent in the frequency range of interest. In preliminary tests, this window was replaced with a KRS5 window. Although not transparent in the far infrared region, the KRS5 was convenient for use in an initial test. These tests proved successful and that window was replaced with chemical vapor deposition (CVD) diamond. The diamond window was made from a fragment of a 0.5 inch diameter window intended to separate the rough and ultra high vacuum spaces of the beamline which was broken during installation. The fragment was much smaller than the original polyethylene window and a recessed mount was fabricated so the f/3.5 light from the Bruker optics could pass through it. Figure B.1 contains a drawing of the new window housing as well as the element and filter.

When first attempted, there was too much light from the synchrotron and the detector was saturated for all beam currents. To reduce the amount of light on the detector, an aperture was placed in the beam path. With the aperture in place, the

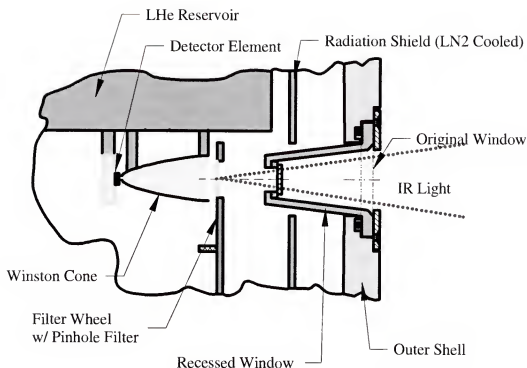


Figure B.1: Drawing of the changes to the bolometer detector. The original polyethylene window was replaced by a recessed CVD diamond. One of the cold filters was replaced by a brass disk with a pinhole.

detector was functional for moderate beam currents. A plot of the measured single beam spectrum through the instrument using a $\text{CaF}_2\text{:Si}$ beam splitter is shown in Figure B.2. The beam splitter absorbs below 1450 cm^{-1} . The structure between 1600 and 4000 cm^{-1} is due to absorption by the diamond windows in the beamline and on the detector. The decrease in the spectrum with increased frequency is due to the limited response time of the detector. This bolometer has a response time of a few tenths of a millisecond. The spectrum shown was taken with a mirror velocity of 10 cm/s . At this velocity, a 0.2 ms response time corresponds to a frequency of 500 cm^{-1} . For higher frequencies, the detector is too slow to make a

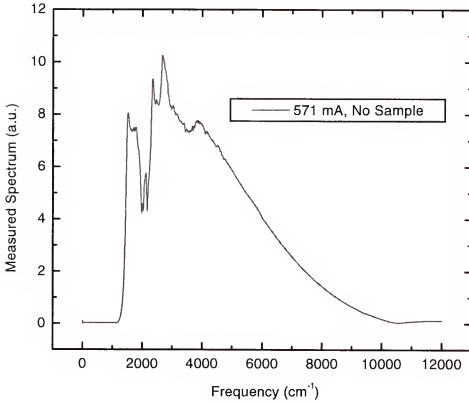


Figure B.2: Single beam spectra taken with the pinhole filter and a $\text{CaF}_2\text{:Si}$ beam splitter. Structure between 1800 and 2000 cm^{-1} is due to absorption by the diamond windows in the beamline and detector. The decline of the power at high frequencies is a consequence of the slow detector response.

complete response to the changes in the interference signal measured, causing the consistent drop in the single beam spectra shown.

The pinhole filter also performed well below 2000 cm^{-1} . Figure B.3 shows a 100% line using the pinhole filter with a Si wafer beam splitter taken during the initial tests with a KRS5 window (which absorbs below 400 cm^{-1}). The signal-to-noise is reasonably good down to about 500 cm^{-1} (noise is less than 0.5% of the signal on average). The increased noise at the lower frequencies is attributed

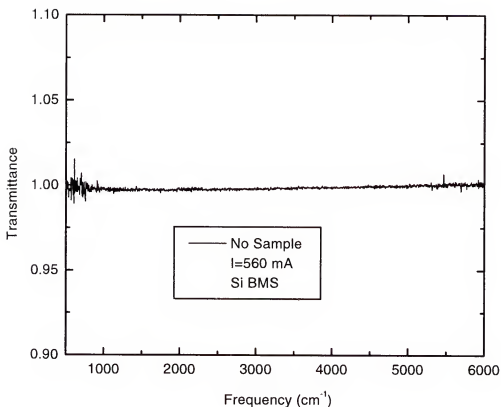


Figure B.3: 100% line using the pinhole filter with a silicon wafer as a beam splitter. The Si wafer is efficient over a broad spectral range, though slight variations in the wafer thickness limited its useful range to below 6000 cm^{-1} .

to increased sensitivity to beam motion as the diffraction limited spot size for those frequencies becomes comparable in size to that of the hole in the filter. For measurements below 700 cm^{-1} the standard filters can be used providing reasonable overlap. The Si wafer beam splitter is efficient over a broad spectral range. However, variations in thickness limited its useful upper frequency to $\sim 6000\text{ cm}^{-1}$. Also, interference due to multiple internal reflections within the wafer limited its resolution to 4 cm^{-1} . See Section 2.3.1 for more details.

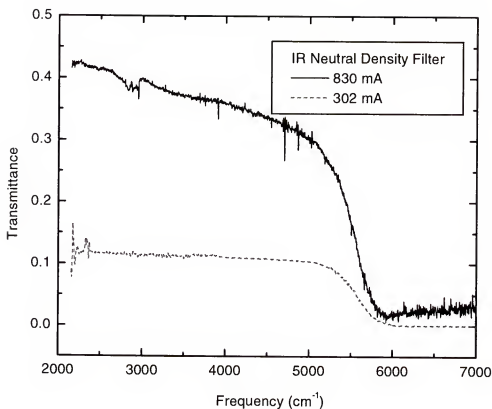


Figure B.4: Transmittance through a IR neutral density filter. The two curves are for 2 beam currents and show a large nonlinearity at high currents due to the increased fluence overheating the detector. The roll off at 6000 cm^{-1} is due to the Ge substrate. The slight slope is intrinsic to the filter and has been observed with other instruments and detectors.

There was evidence of nonlinearity at high beam currents. Figure B.4 shows the transmittance of an IR filter for two different beam currents. The filter is a 10% transmission neutral density filter. The spectrum measured at low current is the correct spectrum for this filter. The slope and transmittance slightly above 10% are consistent with measurements with other instruments and detectors. The high beam current spectrum is much higher than that of the low current. This is caused by nonlinearity in the detector. At high beam currents, the IR synchrotron

radiation warms the detector element to the point that it loses responsivity. The result an erroneously low background spectrum and when the sample spectrum is divided by the lower background, the transmittance calculated is too high.

The bolometer resistance provides a good gauge of how much total radiation is absorbed by the element. The detector has a 10 M Ω load resistor in series with the detector element. With the synchrotron source blocked, the total resistance is over 25 M Ω . At a current of 600 mA, the resistance was about 13 M Ω . At a beam current of 900 mA, the resistance was below 10.5 M Ω . The detector measures changes in total resistance. Once the element resistance drops below about 11 M Ω , the changes in resistivity are no longer proportional to the changes in temperature. Hence, the detector loses its linearity and erroneous spectra result.

The neutral density filter was absorptive above 6000 cm⁻¹. To test the detector at higher frequencies, a series of measurements were made with no sample in place, instead, following the beam current decay. Figure B.5 shows a series of 14 spectra taken at 10 minute intervals. All spectra are normalized by the same background. The data show the decay of the beam current as the average value falls over time. There is some structure near 2000 cm⁻¹ caused by absorption features of the diamond window not dividing out completely. The spectra do not remain flat over the course of the beam current decay. The deviations are attributed to drifts in the interferometer and are not thought to be due to the detector. Such drifts are common in high frequency spectra taken with this instrument and are usually avoided by taking several background and sample spectra back to back, or interleaved in order to average out such errors.

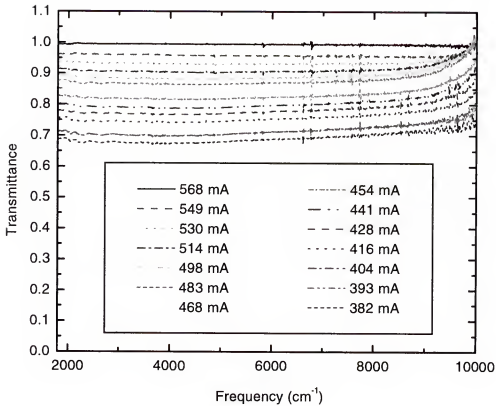


Figure B.5: Transmission as a function of beam current.

B.3 Summary

The motivation behind this experiment was to explore the possibility of using the high brightness of synchrotron radiation to extend to useful frequency range of bolometric detectors. The experiments showed that with the synchrotron source in conjunction with a pinhole cold filter, the effective range of the bolometer used in the test was extended to $10,000 \text{ cm}^{-1}$. The bolometer proved to be sensitive to the amount of light falling on it and showed substantial nonlinearity at high beam currents, despite aperturing of the beam to reduce the flux on the detector. This nonlinearity makes the usefulness of this detector at high frequencies questionable

for absolute spectroscopy. However, for qualitative analysis, such as surface science and many biological applications, the nonlinearity is acceptable. In these cases, this detector may prove useful. The detector could be used for absolute spectroscopy of small samples, assuming the reference spectra (empty hole or mirror) was taken through an aperture of similar size to the sample. The major advantage would be in allowing coverage from 10–10,000 cm^{-1} with a single detector. With a silicon beam splitter the possibility exists for measuring this range with a single alignment. Thus, alleviating the discontinuities that sometimes occur when merging data from different beam splitters and detectors.

In conclusion, these experiments have shown the bolometer to be a viable detector at frequencies an order of magnitude or more higher than those for which it is typically used. The potential use as a single detector to avoid alignment shifts and the potential cost savings of not requiring a separate mid infrared detector suggest that this type of system be studied further to ascertain its efficiency when compared to other common mid IR detectors.

APPENDIX C LASER OPERATION

This appendix will give a brief description of the laser and optics used for the pump pulse in the experiments described in this dissertation. It also includes a short manual on operating the laser and pulse-pickers. For a more detailed description of the laser and a thorough description of its use, including day-to-day operation and trouble shooting, please refer to the Mira and Verdi users manuals. For instructions on synchronizing the laser to the ring, refer to the Synchro-lock manual.

C.1 Description

Figure C.1 shows the layout of the laser and optics. The pump laser (1) is a Coherent Verdi diode-pumped, Nd:vanadate laser capable of output powers up to 5.5 W. The Verdi uses power tracking software to maintain stable operation. For normal operations the Verdi is run with 5 W output power. The Mira (2) is a mode-locked Ti:sapphire laser custom built by Coherent to operate at twice the RF frequency of the NSLS VUV ring (105.8 MHz). It uses the optical Kerr effect to self-focus the beam which leads to higher gain in mode-locked operation than in continuous wave mode (CW). The CW mode is further reduced by placing a slit in a location where the mode-locked beam's cross-section is smaller than that of the CW beam.

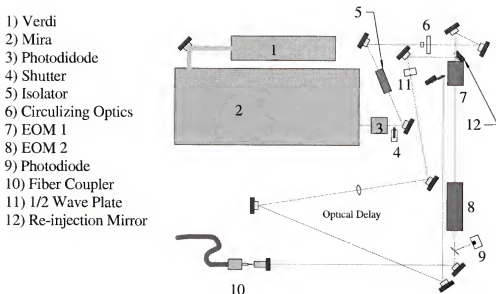


Figure C.1: Diagram of the optical layout of the laser system.

Immediately after the Mira, the beam passes through a beam splitter where a portion is reflected onto a photodiode (3) for diagnostic purposes. Following the diagnostic photodiode, the beam passes through a safety shutter (4) and is then reflected through a Faraday isolator (5). The isolator is based on the Faraday effect and prevents reflections from downstream optics from re-entering the cavity and destabilizing the Mira. After the isolator, the beam passes through a pair of cylindrical lenses (6) used to correct a slight ellipticity in its cross-section. The beam then passes through the first pulse-picker (7). The pulse-picker is an electro-optical modulator (EOM) used to reject every other pulse and thus reduce the pulse repetition frequency (PRF) of the laser to 52.88 MHz, that of the synchrotron. The EOM consists of a Pockels cell used to rotate the polarization of every other pulse 90 degrees and a polarizing beam splitter which then deflects those pulses whose polarization has been rotated. The rejected pulse is optically delayed and

passed through a half-wave plate (11) which rotates the polarization back to its original state. The pulse is then re-inserted parallel to the original beam path and coincident with the following pulse with a mirror on the edge of the primary beam (12). The second pulse is recycled with an efficiency of about 80%.

Following the first pulse-picker is a second (8) used to further reduce the laser PRF to match that of the synchrotron when operated in single-bunch or 3-bunch symmetric mode. The principle of the second pulse-picker is the same as the first. Following the second pulse-picker, the beam passes through another beam splitter which reflects a portion of the beam onto another photodiode (9) for diagnostic purposes. The remainder of the beam passes into a fiber coupler where it is focused into a optical fiber used to transport the pump pulses to the beamline area.

C.2 Manual

WARNING: The Verdi and Mira are class IV lasers capable of causing severe damage to the eyes and skin. The lasers should only be operated by authorized persons whom have completed the requisite laser training.

Instructions for the day-to-day operation of the Verdi and Mira lasers can be found in their respective users manuals. Consult them for instructions on the alignment and maintenance of the lasers. This manual will primarily concern itself with the additional information needed to operate the laser synchronized to the ring with acceptable power and minimal fluctuations. It is not meant as a replacement for the user manuals and those manuals should be consulted before any attempt is made to operate either the Verdi or the Mira.

What follows is a set of instructions for using the Mira synchronized to the ring RF.

- 1) Turn on the cooling water for the Mira and Verdi. Wait until the Verdi base plate temperature drops below 25.5 K. This usually takes ten to twenty minutes and will reduce the time it takes the laser to stabilize once it is turned on.

- 2) Insure the safety shutter (4) is closed and that the beam is contained so no stray radiation pass to the beamline area.

- 3) Make sure the Verdi shutter is open and then turn on the Verdi. Also, power the phase shifter and frequency divider as well as the first pulse-picker (and the second if 3-bunch or 1-bunch operations are planned).

- 4) Wait approximately 1 hour for the Verdi and Mira to stabilize.

- 5) Once stable, follow the directions in the Mira users manual for day-to-day operations and place the Mira in mode-lock (ML) or beta-lock (β L) mode and synchronize the beam to the ring RF using the Synchro-Lock software.

- 6) Confirm the alignment through the downstream optics is good and that there is efficient coupling into the optical fiber. If the alignment is poor, refer to the Section C.3 for instructions on how to improve the downstream optical alignment.

- 7) Confirm the phase shifter is set at either 0 or 12 volts. Turn on the downstream diagnostic photodiode () and feed its output to an oscilloscope. Minimize the intensity of the rejected peak by adjusting the bias voltage on the first pulse-picker.

- 8) Turn on the function generator used for dithered measurements and set it for a 1-2 V 100 Hz square dither.

9) Feed the output of the downstream diagnostic photodiode to a lock-in amplifier using the output of the function generator as a reference. Minimize the signal on the lock-in by adjusting the slit width and position on the Mira.

10) Proceed with experiments.

C.3 Optimization of the Downstream Optics

This section describes the procedure to follow for optimizing the throughput of the downstream optics.

1) Maximize the power passing through the optical isolator by adjusting its position and the mirror reflecting the beam into the isolator.

2) With the rejected beam blocked, maximize the power passing through the first pulse-picker by adjusting the input mirror and the pulse-picker position and alignment. The pulse-picker alignment is sensitive and the beam should pass through the center with no distortions. This must be done with the laser mode-locked and the pulse-picker operating.

3) Maximize the power through the second pulse picker by adjusting its alignment and the alignment of the input mirrors (also used for the first pulse-picker). A few iterations of steps 2 and 3 may be necessary to achieve a good alignment.

4) Once a good alignment of the primary pulse has been achieved, unblock the rejected pulse beam and align it visually until it is on the edge of the mirror used to re-insert it into the beam path next to the following pulse and at the same height as the primary beam. Then adjust that mirror until the second beam is coincident with the primary beam at a point after the second pulse picker.

5) Place a power meter at the position where the two beams overlap. Adjust the half-wave plate to maximize the power.

6) Block the second beam and optimize the coupling of the first into the optical fiber using the adjustments of the fiber coupler. Then unblock the second beam and optimize its coupling by adjusting the re-insertion mirror.

Under ideal conditions a maximum of 450–500 mW can be achieved at the beamline. Typical values are near 400 mW for normal operations with the slits closed slightly from the maximum mode-locked power width, giving more stable operation.

REFERENCES

- [1] J. Schwinger. *Phys. Rev.*, 75:1912, 1949.
- [2] W. D. Duncan and G. P. Williams. *Applied Optics*, 22:2914, 1983.
- [3] G. P. Williams. *Sync. Rad. News*, 8:8, 1995.
- [4] G.L. Carr, M. Hanfland, and G.P. Williams. *Rev. Sci. Inst.*, 66:1643, 1995.
- [5] G. L. Carr, P. Dumas, C.J. Hirschmugl, and G.P. Williams. *Il Nuovo Cimento*, 20:375, 1998.
- [6] J.A. Reffner, P.A. Martoglio, and G.P. Williams. *Rev. Sci. Inst.*, 66:1298, 1995.
- [7] C. Hirschmugl. *Nucl. Instr. and Meth.*, A319:245, 1992.
- [8] C. J. Hirschmugl and G. P. Williams. *Sync. Rad. News*, 8:10, 1995.
- [9] G. L. Carr, J. Reichman, D. DiMarzio, M.B. Lee, D.L. Ederer, K.E. Miyano, D.R. Mueller, A. Vasilaka, and W.L. O'Brien. *Semicond. Sci. Technol.*, 8:922, 1993.
- [10] D.L. Ederer, J.E. Rubensson, D.R. Mueller, R. Shuker, W.L. O'Brien, J. Jai, Q.Y. Dong, T.A. Callcott, G.L. Carr, G.P. Williams, C.J. Hirschmugl, S. Etemad, A. Inam, and D.B. Tanner. *Nucl. Instr. and Meth.*, A319:250, 1992.
- [11] N. Katzenellenbogen and D. Grischkowsky. *Appl. Phys. Lett.*, 58:222, 1991.
- [12] Eugene Hecht. *Optics*. Addison-Wesley, Reading, MA, 1989.
- [13] P. Fellgett. *J. Phys. Radium*, 19:1187, 1958.
- [14] R.J. Bell. *Introductory Fourier Transform Spectroscopy*. Academic Press, New York, NY, 1972.
- [15] Peter R. Griffiths and James A. de Haseth. *Fourier Transform Infrared Spectroscopy*. John Wiley & Sons, New York, NY, 1986.

- [16] W. Herres and J. Gronholtz. *Comp. App. Lab.*, 2:216, 1984.
- [17] J. Gronholtz and W. Herres. *Instruments & Computers*, 3:10, 1985.
- [18] J. Gronholtz and W. Herres. *Instruments & Computers*, 3:45, 1985.
- [19] J. Strong and G.A. Vanasse. *J. Opt. Soc. Am.*, 54:1474, 1964.
- [20] C.D. Porter and D.B. Tanner. *Int. J. Infrared and Milimeter Waves*, 4:273, 1983.
- [21] D.B. Tanner and R.P. McCall. *Appl. Opt.*, 23:2363, 1984.
- [22] Giorgio Margaritondo. *Introduction to Synchrotron Radiation*. Oxford University Press, New York, NY, 1988.
- [23] John David Jackson. *Classical Electrodynamics*. John Wiley & Sons, New York, NY, 1975.
- [24] S. Gasiorowicz. *Quantum Physics*. John Wiley & Sons, New York, NY, 1974.
- [25] G.P. Williams, C.J. Hirschmugl, E.M. Kneedler, P.Z. Takacs, M. Shleifer, Y.J. Chabal, and F.M. Hoffmann. *Phys. Rev. Lett.*, 62:261, 1989.
- [26] F. Wooten. *Optical Properties of Solids*. Academic Press, New York, NY, 1972.
- [27] J.A. Stratton. *Electromagnetic Theory*. McGraw-Hill, New York, NY, 1941.
- [28] Neil W. Ashcroft and N. David Mermin. *Solid State Physics*. Saunders College, Philadelphia, PA, 1976.
- [29] C. Kittel. *Introduction to Solid State Physics*. John Wiley & Sons, New York, NY, 1986.
- [30] R.P.S.M. Lobo. *Rev. Sci. Inst.*, 70:2899, 1999.
- [31] R.L. Henry and D.B. Tanner. *Infrared Physics*, 19:173, 1979.
- [32] E.Z. Rothman and J.B. Hastings, editors. *National Synchrotron Light Source Activity Report 1997*. Brookhaven National Laboratory, Upton, NY, 1998.
- [33] D.E. Spence, P.N. Kean, and W. Sibbett. *Opt. Lett.*, 16:42, 1991.
- [34] D.E. Spence, J.M. Evans, W.E. Sleat, and W. Sibbett. *Opt. Lett.*, 16:1762, 1991.

- [35] R. Winston. *J. Opt. Soc. Amer.*, 60:245, 1970.
- [36] R.H. Hildebrand and R. Winston. *Appl. Opt.*, 21:1844, 1982.
- [37] C. Benoit a-la Guillaume. *Selected Constants Relative to Semiconductors*. Pergamon, 1961. and references therein.
- [38] RK. Willardson and A.C. Beer, editors. *Semiconductors and Semimetals*, volume 16. Academic Press, New York, NY, 1981. and references therein.
- [39] D Long. *Energy Bands in Semiconductors*. Wiley, New York, NY, 1968.
- [40] M. Abramowitz and I.A. Stegun. *Handbook for Mathematical Functions*. Dover Publications, Inc., New York, NY, 1972.
- [41] W.S. Pelouch and L.A. Schlie. *App. Phys. Lett.*, 68:1389, 1996.
- [42] J. Bardeen, L.N. Cooper, and J.R. Schrieffer. *Phys. Rev.*, 108:1175, 1957.
- [43] L.R. Testardi. *Phys. Rev. B*, 4:2189, 1971.
- [44] H.K. Onnes. *Comm. Phys. Lab. Univ. Leiden*, (119,120,122), 1911.
- [45] Michael Tinkham. *Introduction to Superconductivity*. Krieger Publishing Co., Malabar, FL, 1980.
- [46] Pierre-Gilles de Gennes. *Superconductivity of Metals and Alloys*. Addison-Wesley, Redwood City, CA, 1989.
- [47] E.A. Lynton. *Superconductivity*. Methuen & Co. LTD., London, Gr. Br., 1969.
- [48] S.B. Nam. *Phys. Rev.*, 156:470, 1967.
- [49] S.B. Nam. *Phys. Rev.*, 156:487, 1967.
- [50] D.M. Ginsberg and M. Tinkham. *Phys. Rev.*, 119:575, 1960.
- [51] F. Marsiglio, J.P. Carbotte, and M. J. Blezius. *Phys. Rev. B*, 41:6457, 1990.
- [52] R.E. Harris and D.M. Ginsberg. *Phys. Rev.*, 188:737, 1969.
- [53] F.Chilton, editor. *Superconductivity*. North-Holland, Amsterdam, 1971.
- [54] W.Shaw and J.C. Swihart. *Phys. Rev. Lett.*, 20:1000, 1968.
- [55] R.E. Glover and M. Tinkham. *Phys. Rev.*, 104:884, 1956.

- [56] R.E. Glover and M. Tinkham. *Phys. Rev.*, 108:243, 1957.
- [57] D.M. Ginsberg and M. Tinkham. *Phys. Rev.*, 118:990, 1960.
- [58] H.D. Drew and A.J. Sievers. *Phys. Rev. Lett.*, 19:697, 1967.
- [59] L.H. Palmer and M. Tinkham. *Phys. Rev.*, 165:588, 1968.
- [60] D.B. Tanner. *Phys. Rev. B*, 8:5045, 1973.
- [61] G.L. Carr, J.C. Garland, and D.B. Tanner. *Phys. Rev. Lett.*, 50:1607, 1983.
- [62] D.C. Mattis and J. Bardeen. *Phys. Rev.*, 111:412, 1958.
- [63] D.M. Ginsberg, R.E. Harris, and R.C. Dynes. *Phys. Rev. B*, 14:990, 1976.
- [64] W.H. Parker and W.D. Williams. *Phys. Rev. Lett.*, 29:924, 1972.
- [65] C.S. Owen and D.J. Scalapino. *Phys. Rev. Lett.*, 28:1559, 1972.
- [66] J.R. Schrieffer and D.M. Ginsberg. *Phys. Rev. Lett.*, 8:207, 1962.
- [67] A. Rothwarf and M. Cohen. *Phys. Rev.*, 130:1401, 1963.
- [68] M. Tinkham and J. Clarke. *Phys. Rev. Lett.*, 28:1366, 1972.
- [69] J. Chang and D.J. Scalapino. *Phys. Rev. B*, 9:4769, 1974.
- [70] W.H. Parker. *Phys. Rev. B*, 12:3667, 1975.
- [71] A. Rothwarf and B.N. Taylor. *Phys. Rev. Lett.*, 19:27, 1967.
- [72] G.L. Carr, R.P.S.M. Lobo, J. LaVeigne, D.H. Reitze, and D.B. Tanner. To be published.
- [73] G.A. Sai-Halasz, C.C. Chi, A. Denenstein, and D.N. Langenberg. *Phys. Rev. Lett.*, 33:215, 1974.
- [74] R. Peters and H. Meissner. *Phys. Rev. Lett.*, 30:965, 1973.
- [75] M. Johnson. *Phys. Rev. Lett.*, 67:347, 1991.
- [76] J.F. Federici, B.I. Greene, D.H. Rapkine, , and J. Orenstein. *Phys. Rev. B*, 43:8617, 1991.
- [77] S. Nodvick and D.S. Saxon. *Phys. Rev.*, 96:180, 1954.

- [78] F.C. Michel. *Phys. Rev. Lett.*, 48:580, 1982.
- [79] C.J. Hirschmugl, M. Sagurton, and G.P. Williams. *Phys. Rev. A*, 44:1316, 1991.
- [80] G.T. Fraser, A.R. Hight Walker, U. Arp, T. Lucatorto, and K.K. Lehmann. *SPIE*, 3153:42, 1997.
- [81] G.L. Carr, R.P.S.M. Lobo, C.J. Hirschmugl, J. LaVeigne, D.H. Reitze, and D.B. Tanner. *SPIE*, 3153:80, 1997.
- [82] J.M. Wang. *Phys. Rev. E*, 58:984, 1998.
- [83] F.J. Low. *Appl. Opt.*, 2:649, 1963.
- [84] F.J. Low. *J. Opt. Soc. Am.*, 51:1300, 1961.

BIOGRAPHICAL SKETCH

Joe LaVeigne was born in Ocala, Florida on June 23, 1968. He recieved his bachelor's degree in aerospace engineering from the University of Floria in May 1991. After one year he returned to academics at the University of Florida to study for an advanced degree in physics. In 1994, he joined David Tanner's research group in the Department of Physics. In 1996, he began work on the time-resolved infrared spectroscopy project at the U12IR beamline of the National Synchrotron Light Source in Brookhaven National Lab. In 1997, he moved to Long Island to work full-time at the experiment site.

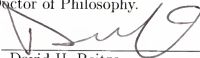
Joe is married to Yao-yi Tseng, who he met in class during his first year studying physics.

I certify that I have read this study and that in my opinion it conforms to acceptable standards of scholarly presentation and is fully adequate, in scope and quality, as a dissertation for the degree of Doctor of Philosophy.



David B. Tanner, Chairman
Professor of Physics

I certify that I have read this study and that in my opinion it conforms to acceptable standards of scholarly presentation and is fully adequate, in scope and quality, as a dissertation for the degree of Doctor of Philosophy.



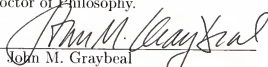
David H. Reitze
Associate Professor of Physics

I certify that I have read this study and that in my opinion it conforms to acceptable standards of scholarly presentation and is fully adequate, in scope and quality, as a dissertation for the degree of Doctor of Philosophy.



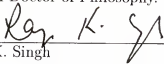
Selman Hershfield
Associate Professor of Physics

I certify that I have read this study and that in my opinion it conforms to acceptable standards of scholarly presentation and is fully adequate, in scope and quality, as a dissertation for the degree of Doctor of Philosophy.



John M. Graybeal
Associate Professor of Physics

I certify that I have read this study and that in my opinion it conforms to acceptable standards of scholarly presentation and is fully adequate, in scope and quality, as a dissertation for the degree of Doctor of Philosophy.



Rajiv K. Singh
Professor of Materials Science and Engineering

This dissertation was submitted to the Graduate Faculty of the Department of Physics in the College of Liberal Arts and Sciences and to the Graduate School and was accepted as partial fulfillment of the requirements for the degree of Doctor of Philosophy.

August 1999

Dean, Graduate School